University of Southampton Research Repository

UNIVERSITY OF SOUTHAMPTON

FACULTY OF ENGINEERING AND THE ENVIRONMENT

Engineering Sciences

Development of nanocrystalline graphite for MEMS and membranes

by

Sam J. Fishlock

Thesis for the degree of Doctor of Philosophy

April 2017

UNIVERSITY OF SOUTHAMPTON

ABSTRACT

FACULTY OF ENGINEERING AND THE ENVIRONMENT

<u>Engineering Sciences</u>

Thesis for the degree of Doctor of Philosophy

Development of nanocrystalline graphite MEMS and Membranes

Sam Jeffery Fishlock

Thin carbon films such as graphite and graphene are promising materials for micro- and nanoelectromechanical systems (MEMS and NEMS) applications, including resonators and switches, and also to be used as membranes for molecular sieving. The potential of these materials to be used in such applications is due to their electrical and mechanical properties, and also because they may be used as ultra-thin films. However, the most widely-used methods to synthesise these films have a tendency to cause poor performance in MEMS and NEMS. The most common technique, chemical vapour deposition (CVD) onto a catalyst, is followed by a physical transfer of the film to a separate substrate. This causes wrinkling and a variation in strain across the film, which leads to variable performance of MEMS and NEMS. Therefore, plasma-enhanced CVD (PECVD), which can be used to deposit nanocrystalline graphitic films directly onto large-area substrates, such as 6-inch silicon wafers, is a promising route to overcome this issue.

Doubly-clamped beams and square micromechanical membranes were fabricated using nanographite films of 300 to 400 nm thickness, on silicon substrates. The compressive built-in stress of the film, measured as 436 MPa, caused these microstructures to buckle out-of-plane when they were released. The buckling behaviour of both structures was used as a characterisation tool to measure the Young's modulus of nanographite, which is a key mechanical parameter of materials, and was measured as 23 GPa.

To demonstrate the use of nanographite in a MEMS application, cantilever and doubly-clamped beam resonators of thickness around 300 nm were fabricated. Despite the built-in compressive stress of the film, the doubly-clamped beams were fabricated without buckling, and were under an effective tensile stress. This was achieved through the fabrication procedure, by using a 25 to 30 µm isotropic etch undercut of the 200 µm-wide anchors. The stress gradient in the film caused deflection of the anchors which 'pulled' the beams tight through the application of tensile stress. The devices were actuated electrostatically and the vibration response was measured using laser Doppler vibrometry. Cantilevers were measured with fundamental natural frequencies between 5 and 25 kHz, and for

doubly-clamped beams natural frequencies were measured between 245 and 640 kHz. Quality factors under ambient pressure were around 5 to 10 for cantilevers and 20 to 30 for doubly-clamped beams, and around 1800 under 30 mTorr vacuum for a doubly-clamped beam.

An ultrahigh vacuum system with mass spectrometer was constructed to measure the permeance of gases through nanographite thin films. The permeance of He, H_2, Ne, CO_2 and O_2 through 350 nm thick nanographite membranes was measured. The permeance of He, H_2 and Ne at 150 °C was 5.1, 4.0 and 0.08×10^{-10} mol / (m$^2 \cdot$s $\cdot$ Pa), respectively, but the permeance of CO_2 and O_2 was below the limit of detection of the mass spectrometer. An estimation of the maximum permeance of CO_2 and O_2 respectively were 1.12×10^{-12} and 4.76×10^{-15} mol / (m$^2 \cdot$s $\cdot$ Pa). The low permeance of Ne, CO_2 and O_2 relative to H_2 and He showed that nanographite is a promising membrane material for molecular sieving.

Table of Contents

Contents

DECLARATION OF AUTHORSHIP

I, Sam Jeffery Fishlock declare that this thesis and the work presented in it are my own and has been generated by me as the result of my own original research.

I confirm that:

1. This work was done wholly or mainly while in candidature for a research degree at this University;
2. Where any part of this thesis has previously been submitted for a degree or any other qualification at this University or any other institution, this has been clearly stated;
3. Where I have consulted the published work of others, this is always clearly attributed;
4. Where I have quoted from the work of others, the source is always given. With the exception of such quotations, this thesis is entirely my own work;
5. I have acknowledged all main sources of help;
6. Where the thesis is based on work done by myself jointly with others, I have made clear exactly what was done by others and what I have contributed myself;
7. Parts of this work have been published, see publications list.

Signed: ....

Date: ....

Declaration

The photograph in Figure 3.1 (A) was taken by Dr Ahmed Abuelgasim. The UHV apparatus described in Section 3.3 was designed by Dr Sean O'Shea, IMRE, A*STAR Singapore, and myself, and was constructed by me. The X-ray reflectivity result in Section 4.2 was taken and fitted by Mr Lim Poh Chong, IMRE, A*STAR Singapore. The SEM image in Section 4.2 was taken by Mr Andrew Breeson, IMRE, A*STAR Singapore.

Acknowledgements

Publications

Journal article

S.J. Fishlock, D. Grech, J.W. McBride, H.M.H. Chong, S.H. Pu, Mechanical characterisation of nanocrystalline graphite using micromechanical structures, Microelectronic Engineering. 159 (2016) 184–189. doi:10.1016/j.mee.2016.03.040.

S.J. Fishlock, J.W. McBride, H.M.H., Chong, S.J. O'Shea, S.H. Pu, Fabrication and characterisaiton of nanocrystalline MEMS resonators, *Journal of Micromechanics and Microengineering* (Manuscript in preparation).

S.J. Fishlock, J.W McBride, H.M.H., Chong, S.J. O'Shea, S.H. Pu, Nanocrystalline graphite membranes for molecular separation, *Journal of Membrane Science* (Manuscript in preparation).

Conference presentation

S.J. Fishlock, J.W. McBride, H.M.H., Chong, S.J. O'Shea, S.H. Pu, (2015) Characterisation of nanographite for MEMS resonators. In, *2015 MRS Fall Meeting, Boston, USA, 29 Nov - 04 Dec 2015*.

S.J. Fishlock, J.W. McBride, H.M.H., Chong, S.J. O'Shea, S.H. Pu, (2014) Fabrication and characterisation of nanocrystalline graphite micromechanical structures. At *40th International Conference on Micro and Nano Engineering, Lausanne, CH, 22 - 26 Sep 2014*.

S.J. Fishlock, S.H. Pu, Z.H.A.Hamid, M.E. Schmidt, C. Xu, M. Cooke, J.W. Mcbride, H.M.H. Chong, (2013) Mechanical characterisation of Nanocrystalline graphite. At *39th International Conference on Micro and Nano Engineering, London, UK, 16 – 19 Sep. 2013*.

Definitions and Abbreviations

a	Area
A_{GT}	Geometric constant for gas translational diffusion
B	Gas permeance
b	Beam width
C	Capacitance
c	Damping coefficient
c_c	Critical damping level
C_0	Capacitance at zero displacement
CTE	Coefficient of thermal expansion
D	Diffusion constant
D_{GT}	Diffusion coefficient for gas translational diffusion
D_s	Diffusion coefficient for surface diffusion
d_p	Pore size
E	Young's modulus
$\hat{E}$	Effective Young's modulus for beams of high width to thickness ratio
E_a	Activation energy
E_{GT}	Activation energy for gas translational diffusion
E_S	Activation energy for surface diffusion
EPS	Effective pumping speed
F	Load
f	Frequency
f_0	Natural frequency
F_{crit}	Critical buckling load
G	Concentration
G_1	Upstream concentration
G_2	Downstream concentrations
h	Thickness
I	Second moment of area
J	Molar gas flux
k	Sping constant
k_B	Boltzmann constant
k_d	Kinetic diameter
k_e	Electrostatic spring constant

l	Length
Δl	Added length
m	Mass
Δm	Added mass
M	Atomic mass
N_t	Number of moles
o	Side length of a square membrane
p	Pressure
Δp_{AVG}	Measured change in partial pressure
Δp_0	Measured change in background pressure
p_{leak}	Partial pressure of the analyte through the leak valve
p_{UPS}	Upstream pressure of the gas in the HV chamber
Q	Quality factor
Q_{leak}	The leak rate through the leak valve
Q_m	Leak rate through the membrane
r	Separation distance between beam (top electrode) and substrate
R	Molar gas constant
t	Time period of one oscillation
Δt	Time period over which pressure change is measured
T	Absolute temperature
ΔT	Temperature increase
u	Curvature
v	Volume of the UHV chamber
V_{AC}	Amplitude of the AC voltage
V_{DC}	DC bias voltage
w	Amplitude of buckling
$\bar{w}$	Dimensionless deflection
x	Displacement
z	Constriction of probability factor
α	The ratio of fluxes of two gases (separation factor)
β	Geometric constant
ε	Strain
ζ	Damping ratio
v	Poisson's ratio
ρ	Density
σ	Stress

σ_0	Biaxial stress
σ_{grad}	Through-thickness stress gradient
σ_{ii}	Collision diameter
τ	Diffusional length
ψ	Jump frequency
ω	Radial frequency
$\Delta\omega$	Bandwidth at full-width at half maximum power
λ	Eigenvalue corresponding to a mode shape

a-C:H	Hydrogenated tetrahedral carbon
AFM	Atomic force microscope
AMU	Atomic mass units
CNT	Carbon nanotube
CVD	Chemical vapour deposition
DLC	Diamond-like carbons
FE	Finite element
FIB	Focused ion-beam milling
FWHM	Full width at half maximum
GT	Gas translational
GV	Gate valve
HF	Hydrofluoric acid
HOPG	Highly-ordered pyrolytic graphite
HSQ	Hydrogen silsesquioxane resist
IC	Integrated circuit
ICP	Inductively coupled plasma
LDV	Laser Doppler vibrometry
LPCVD	Low-pressure chemical vapour deposition
MEMS	Microelectromechanical systems
MOFs	Metal-organic frameworks

MPCVD	Microwave plasma-CVD
NCD	Nanocrystalline diamond
NEMS	Nanoelectromechanical systems
NMP	N‑Methyl‑pyrrolidone
PECVD	Plasma-enhanced chemical vapour deposition
Polysilicon	Polycrystalline silicon
RF	Radio frequency
RGA	Residual gas analyser
RIE	Reactive ion etching
SDOF	Single degree-of-freedom
SiNx	Silicon nitride
SOI	Silicon-on-insulator
ta-C	Tetrahedral carbon
TEM	Transmission electron microscope
UHV	Ultrahigh vacuum

1. Introduction

1.1 Use of carbon in MEMS, NEMS and nano-membranes

Micro and nanoelectromechanical systems (MEMS and NEMS) are systems and devices which are fabricated using technology which is adapted from silicon-based electronic integrated circuit (IC) technology. The main difference between MEMS and purely electrical devices is that they have a mechanical element, as well as an electrical element to them. The mechanical element is a part of the system which is released (not adhered) from the substrate. For example, in Figure 1.1 (A), the beam section is released from the substrate, and is free to deflect under an external force. This structure is a building block for a MEMS application termed a resonator. The beam of the resonator has a large vibration amplitude, much like a guitar string, when excited at certain frequencies. One application of a resonator device is as a sensor of strain, for example. Here, as it is subjected to an external strain, its frequency will change, like a guitar string being tightened. The change in the frequency can be used to measure the strain; hence the resonator may be used as a sensor.
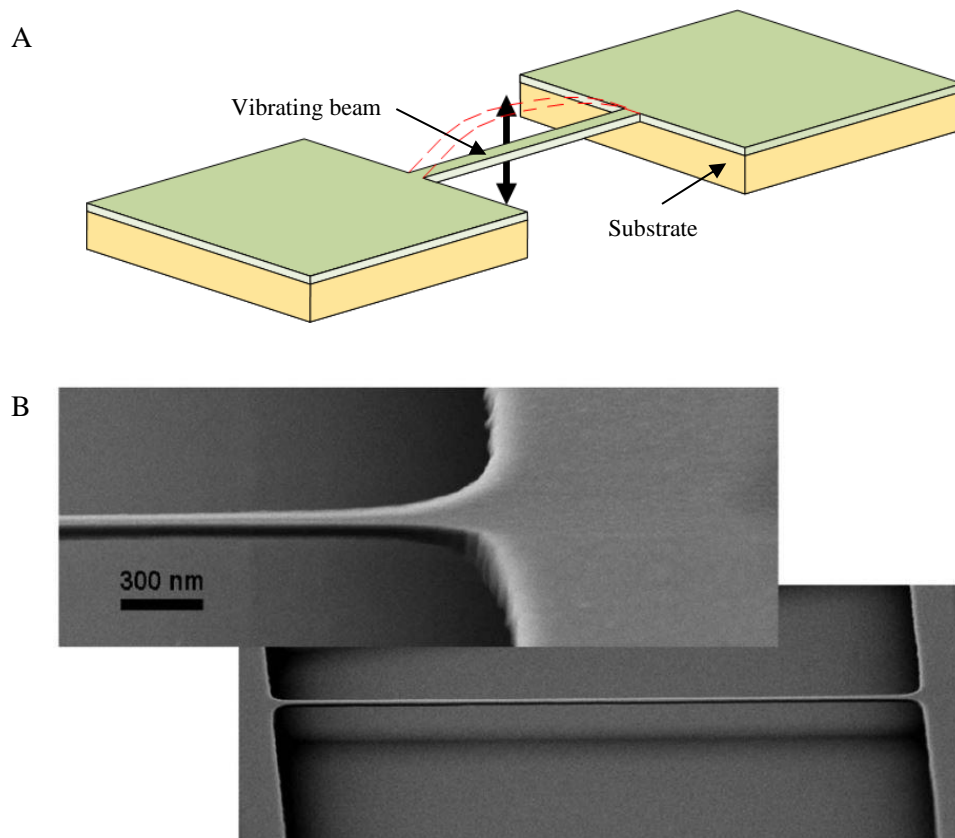
Figure 1.1. (A) Schematic of a resonating doubly-clamped beam. The black arrow shows how the beam deflects when it is excited under resonant vibration. Image adapted from [1] (B) Scanning electron microscope image of a doubly-clamped beam resonator made from silicon nitride [2].

1

The development of MEMS and NEMS has in some ways been similar to the development of ICs. For example, the fabrication of MEMS has been dominated by the use of silicon as the main material. Another similarity between MEMS and ICs is the fact that silicon has some material limitations, which has led to the search for different materials to be used. A third similarity is that this search has often led to carbon-based materials. For example, one of the limitations for silicon in MEMS is that it cannot be readily used in some harsh environments, for example at temperature above 400 °C. This is because the mechanical properties, including the Young's modulus rapidly drop above this temperature [3].

This has led to the search for materials which may be used at high temperature, for example, as sensors in harsh environments. Another development in resonators is in creating devices from ultra-thin films, since the sensitivity of a resonator-based sensor depends on the overall mass of the device. This is a limitation of silicon, since it cannot currently be made into ultra-thin freestanding films of less than a few atomic layers [4]. This is because silicon films become unstable at very low thickness, and tend to misshape and buckle.

Carbon-based materials, such as graphite and graphene, offer some advantageous properties compared with silicon. For example, crystalline graphite has a higher value of Young's modulus (1060 GPa in-plane vs. 169 GPa for silicon in the <110> direction [5,6]) and the Young's modulus of graphite does not decrease at high temperatures above 2000 °C [7]. Graphite can also be made in ultra-thin sheets, even to a single atomic layer, called graphene [8]. There has been significant research interest in graphene and graphite MEMS and NEMS, for example as resonators [9], switches [10] and membrane-based pressure sensors [11].

Another related application for carbon thin films is in nano-scaled membranes [12]. Permeable membranes have long been used as thin layers to filter molecules, where, for example, a mixture of gases is purified, by way of larger molecules being blocked from travelling through the pores of the material [13]. Recently, the use of thin layers of graphite for MEMS and NEMS devices has led to research on the gas permeance through nano-scaled membranes [14]. These membranes are fabricated from thin graphite films using methods which are usually used in NEMS, for example, using patterned substrates [15] and ultraviolet etching [12]. Work by Koenig *et al.* showed that such nano-scaled membranes show promising characteristics as compared to traditional larger membranes, such as high permeance due to the lower thickness [16] and the ability to tailor the material pore-size through etching [12].

One current complication for the use of thin graphite films in both MEMS/NEMS and for membranes lies within the synthesis method used for their production. Graphite or graphene is generally

deposited using thermal chemical vapour deposition (CVD) onto a catalyst such as nickel, copper or germanium [17–19]. However, it is difficult to use the graphitic layer whilst it is still adhered to the catalyst, and it must then be transferred to a more useful substrate, such as silicon or quartz. For applications such as resonators and membranes, this transfer process has a detrimental effect on the device's characteristics. This is because the film is fragile and is susceptible to tears and wrinkles, as may be seen in Figure 1.2 [20]. Therefore there is significant interest in developing methods to produce graphitic films which can be deposited directly onto silicon substrates for use in MEMS/NEMS and membranes.
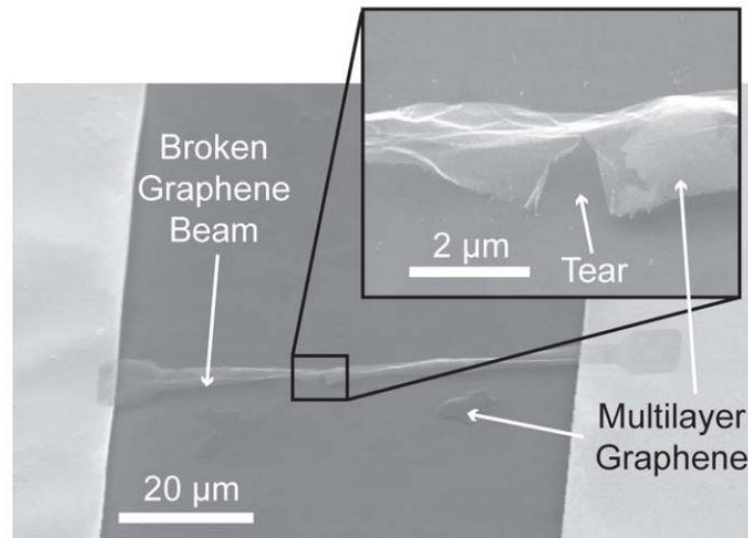
Figure 1.2. Scanning electron microscope image of a multilayer graphene NEMS switch which has failed during operation [20].

One such method to deposit graphitic films is through plasma-enhanced chemical vapour deposition (PECVD) directly onto insulating substrates such as silicon and quartz [21–23]. In PECVD, a carbon-containing gas such as CH_4 is dissociated by an applied radio frequency (RF) electric field, and carbon nucleates into graphene crystallites on the substrate. These crystallites grow to the order of 50 nm in diameter. The crystallite size is smaller than polycrystalline films grown on a metal catalyst (50 nm compared with 10 to 50 µm [24]). The crystal structure of PECVD-grown graphite, called nanocrystalline graphite (nanographite for short), has a large effect on its material properties. For example nanographite is more electrically resistive than single crystal or polycrystalline graphite [22].

In comparing nanocrystalline graphite with polycrystalline graphite, it is clear that there is a trade-off between some of the material properties and the ease and scalability of synthesis of the film. For some MEMS and NEMS applications, whilst it seems promising that the simplicity and scalability of PECVD means that the method may become widely used for future research and industrial applications, there is currently little work on the use of nanographite thin films in MEMS/NEMS

(such as the measurement of its mechanical properties.) The work presented in this Thesis will seek to add knowledge for the future use of MEMS/NEMS and membranes using nanographite thin films.

1.2 Research objectives

1. Present methods of fabricating MEMS and NEMS structures using nanographite deposited directly on substrates such as silicon and quartz.

2. Characterise the mechanical properties of nanographite including the Young's modulus using microstructures.

3. Use nanographite in a MEMS application such as a resonator, and measure the key parameters of natural frequency and quality factor for comparison with the performance of related materials.

4. Fabricate nanographite membranes and characterise its properties for use in gas separation.

1.3 Thesis Structure

The following Chapter is split into two main sections. The first section reviews the literature concerning the use of carbon thin films for MEMS and NEMS resonators, and the second section focuses on the application of carbon membranes for gas separation applications. Chapter 3 presents the experimental methods used in the main experiments of this Thesis, including the fabrication of MEMS and membrane structures, and also includes a description of how they have been characterised. The first types of structures I fabricated were micromechanical beams and membranes. In Chapter 4, I measure the Young's modulus of nanographite from the buckling characteristics of these beam and membrane structures. In Chapter 5, I built on the fabrication process for released beams and characterised electrostatically actuated beams as prototype resonators. In Chapter 6, I present the results of an investigation into the permeance of gases through freestanding nanographite membranes. Finally, in Chapter 7, I conclude the work of my Thesis along with suggestions for furthering this investigation.

2. Literature review

In this Thesis I am researching the development of carbon thin films for applications in MEMS and NEMS resonators and in membranes for gas separation. In the following Section, I provide a short review of the use of carbon thin films in resonator applications, and demonstrate how nanographite thin films deposited using plasma-enhanced chemical vapour deposition may prove a more scalable and robust material than the currently used graphitic thin films. In Section 2.3 I will present an overview of materials used for making membranes to separate gases, and show how nanographite may be a promising material for this application.

2.1 Microelectromechanical systems

MEMS and NEMS are micro- to nano-scaled devices which have both electrical and mechanical behaviour. The major difference between the fabrication of MEMS and NEMS and of purely electronic devices is that the thin film is 'released' or suspended from the substrate, (i.e. there is a section which is not stuck down) and is free to deflect under an applied external force. Typically MEMS devices fall in two categories: (1) MEMS actuators, and (2) MEMS sensors.

The deflection behaviour of a material is governed by its stiffness which can be expressed as its Young's modulus. The Young's modulus E of a material is a measure of its stiffness and governs how much strain ε a material will undergo under an applied stress σ according to Equation 2.1.

$$E = \frac{\sigma}{\varepsilon} \tag{2.1}$$

Where σ and ε may be calculated according to Equations 2.2 and 2.3:

$$\sigma = \frac{F}{a} \tag{2.2}$$

where F is the applied force and a is the cross sectional area.

$$\varepsilon = \frac{\Delta l}{l} \tag{2.3}$$

where Δl is the elongation and l is the original length.

One widespread example of a MEMS device is a resonator. A good analogy for a resonator is a guitar string: if a well-tuned 'A' string is plucked on a guitar, it will vibrate with a frequency of 110.0 Hz [25], the natural frequency (f_0) of the string. An example of a MEMS resonator structure is given in Figure 2.1. In this example, an electrically conducting beam which is clamped at both ends has been released and is suspended in air above the substrate. This is called a doubly-clamped beam. An electrical potential difference V applied between the substrate and the beam creates an electrostatic force F_e on the beam [26]. If the frequency of the applied F_e is equal to the natural frequency f_0 of the beam, then the amplitude of its vibration will become relatively large, compared with the

amplitude at other frequencies. This is an example of a MEMS actuator i.e. a device which converts the electrical input *V* into a mechanical motion of the beam. The resonator may also be used as a sensor: if a mass or strain is applied to the resonator, as shown in Figure 2.2, the resonant frequency f_0 will change. This is the basis for using resonators as sensors.
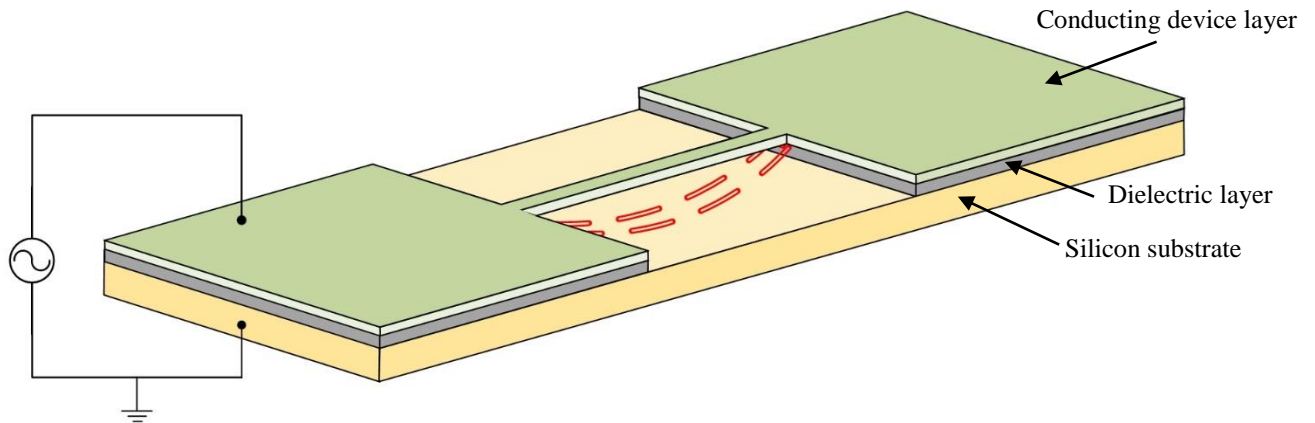
Figure 2.1. Schematic of a MEMS resonator based on a doubly-clamped beam. The potential difference applied between the conducting device layer and the substrate creates an electrostatic force which causes deflection of the beam.
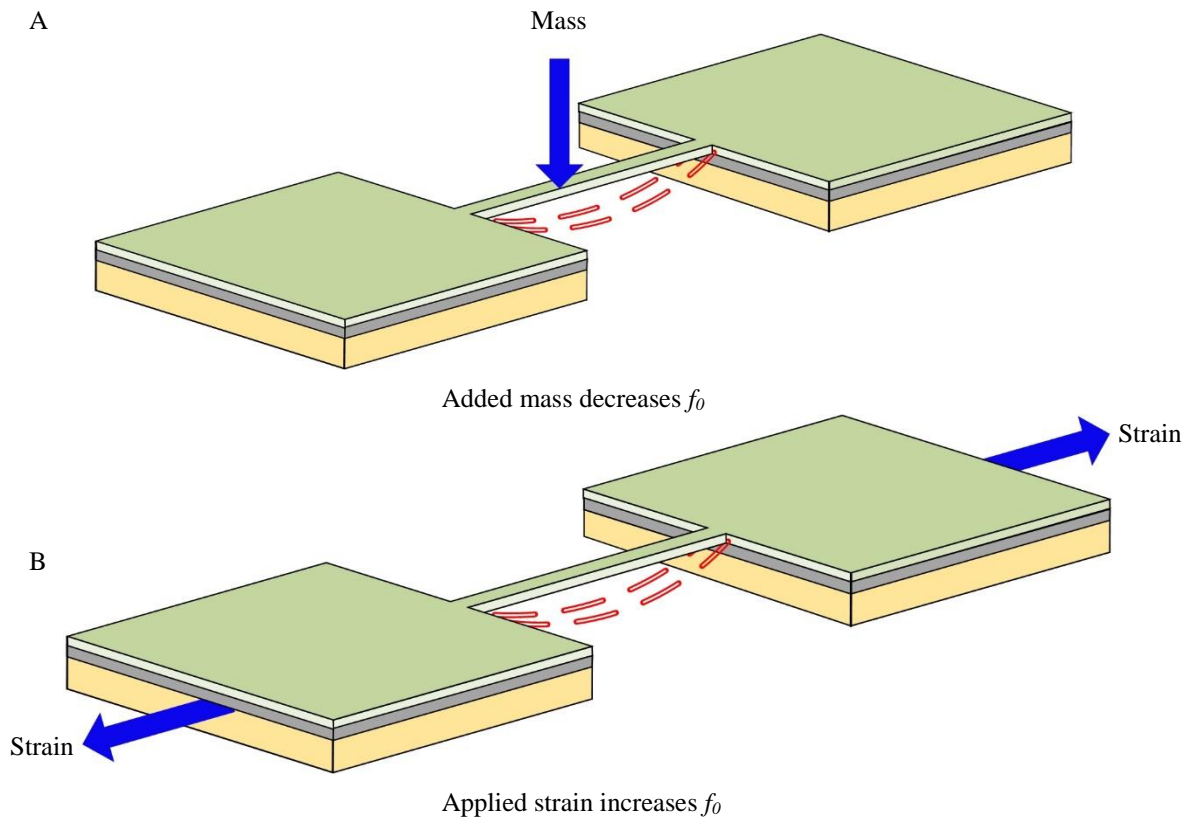
Figure 2.2. Schematic of how a MEMS resonator may be used as a sensor of (A) mass and (B) strain.

A key parameter of resonators is called the quality factor, Q. Q is the ratio of energy stored over energy loss, and is measured as the full width at half maximum (FWHM) of the power amplitude of the frequency response, which is, for example, shown in Figure 2.3. The frequency response of resonator with a high value of Q is typified by a high and narrow peak. The natural frequency of vibration is shown as f_o and the full width half maximum is FWHM and the peak amplitude is A_0. The FWHM is defined for a power spectrum as $A_0^2 / 2$. Thus in the amplitude spectrum the FHWM corresponds to $A_0 / \sqrt{2}$. Q is calculated as in Equation 2.4 [27]. The quality factor is an important parameter in resonators, as, for example, a higher value of Q may enable higher detection of forces, as a more distinct peak may enable more sensitive detection in changes of f_o.

$$Q = f_o / \text{FWHM} \tag{2.4}$$
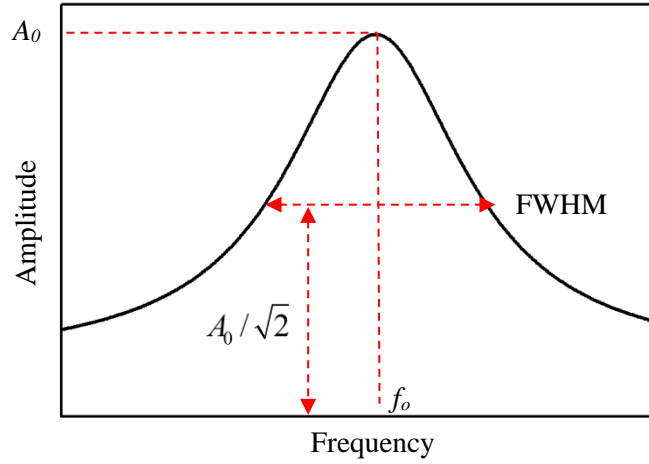
Figure 2.3. Schematic plot of the amplitude against frequency for a resonator excited in a natural mode of vibration, with key points denoted.

MEMS are fabricated using methods adapted from the more mature IC industry. A typical process involves the use of silicon substrates, on which thin films are deposited, patterned and etched. Figure 2.4 shows a simple example of fabricating a silicon nitride (SiN$_x$) cantilever beam [28]. The released beam in Figure 2.4 (C) may also be used as the basic structure of a resonator. This is a clamped-free beam, which is called a cantilever. Other structures which are commonly used as resonators are doubly-clamped beams [29], and membranes (sheets which are fully clamped on all sides) [30], double-end tuning forks [31] and disk-shaped resonators [32]. Micro and nano-scaled membranes are also used in a range of different applications including filtration of biomolecules [33] and gases [34] or as impermeable barriers [15].
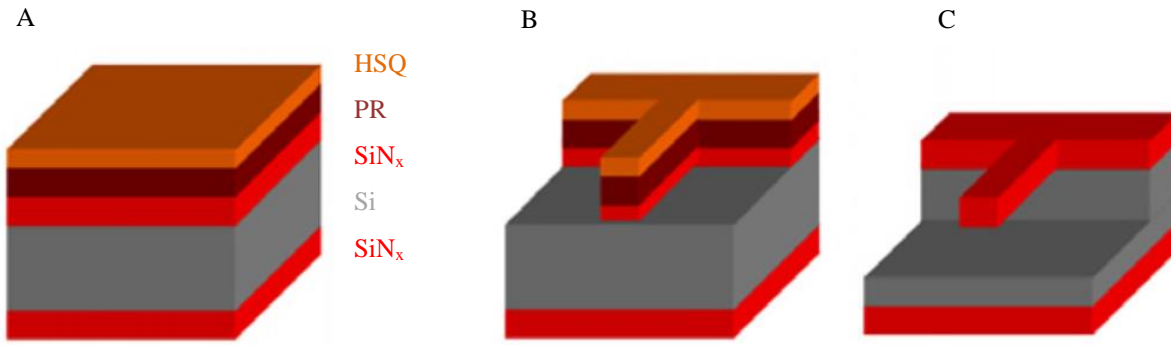
Figure 2.4. A typical cantilever fabrication process. (A) Overall layer stack where HSQ is Hydrogen silsesquioxane resist and PR is a positive photoresist. (B) After patterning and etching of the SiN_x layer. (C) Release of the cantilever structure by an isotropic dry etch process. Image adapted from [28].

This literature survey is split into two main parts and both parts focus on the use of carbon thin films. Part 2.2 centres on the use of carbon in MEMS and NEMS resonator applications, and Part 2.3 focuses on membranes. These two applications are linked as they are fabricated using similar techniques and are of similar materials. However, because of the difference in application, it is helpful to split this discourse into two sections.

2.2 Introduction to MEMS resonators

For many communication applications (for example communication by mobile phone), a frequency reference is required [35]. The most widely used frequency reference is a quartz crystal oscillator [36]. In the case of a quartz crystal oscillator, the mechanical vibration of the crystal is excited electrically, and the amplitude of vibration becomes large at its natural frequency f_0, which may be used as a timing reference since $f_0 = 1 / t$ (where t is time period of one oscillation). A quartz crystal is usually within the size range of mm^2 - cm^2 [37] and is generally located externally to the IC of an electronic device. The large size of the quartz crystal and inherently difficult material etch processes means this type of oscillator is very inefficient in terms of space and integration with IC fabrication.

The first pioneering work to overcome the issue of integration dates to the 1960's by Nathanson *et al*.[38]. This work recognised the significant advantage of fabricating MEMS structures using silicon IC technology. Their device, shown in Figure 2.5 (A-B), comprised of a 500 µm long gold cantilever beam with a resonant frequency of 60 kHz and quality factor (*Q)* of 500, tested at ambient pressure.

For some context on the values of *Q* for resonators, Figure 2.6 shows a plot of *Q* for a number of MEMS and NEMS resonators, and how this varies with the volume of the device. The value of *Q* decreases as the volume decreases, because in a crystalline material the mechanical energy dissipation is dominated by losses at or near the surface [39]. As a benchmark, a MEMS beam of

length 100 µm, width 10 µm and thickness 0.5 µm has a volume of 5×10^{-7} mm³. This is roughly the volume of the devices which are fabricated in the work of this Thesis.
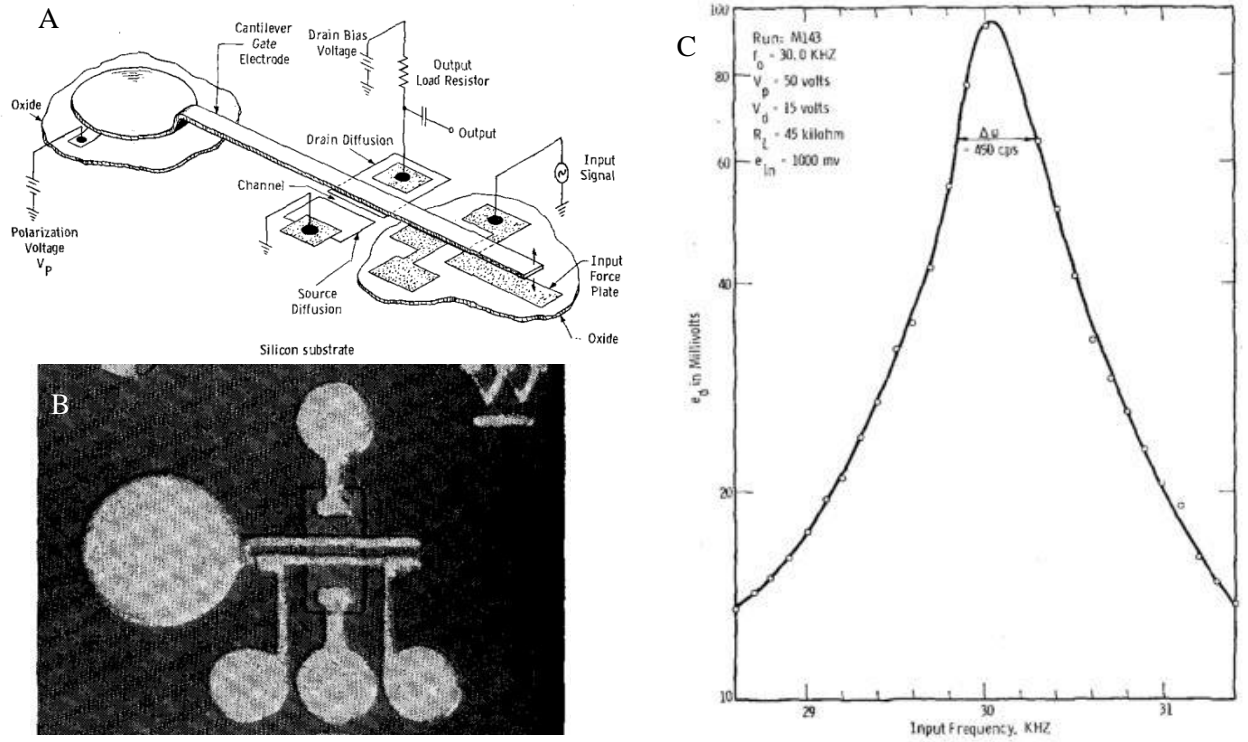
Figure 2.5. (A) Schematic of the first micro machined resonator, a gold cantilever beam [38]. (B) Photograph of the resonator. (C) Frequency response showing the detected output voltage of the device with varying input frequency. Images adapted from [38].
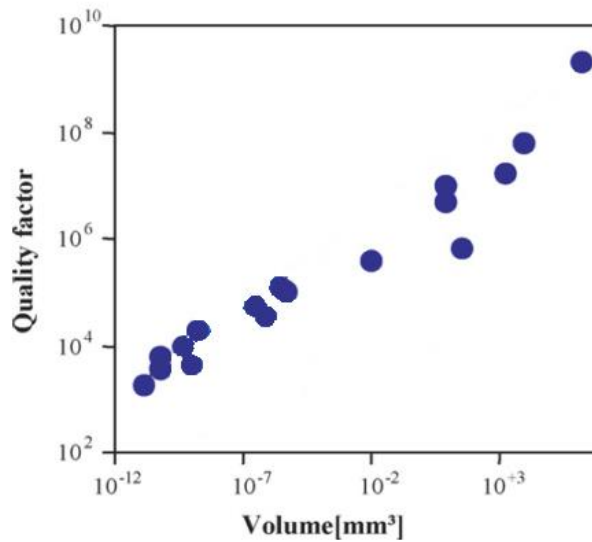
Figure 2.6. Maximum Q of various monocrystalline silicon MEMS and NEMS resonators plotted against the volume of the structural element (for example, the volume of a beam). Image adapted from [1].

The natural frequency f_0 of a structure at resonance is a function of its stiffness and mass; therefore a change in these quantities will cause a change in f_0 as described in Equation 2.5.

$$f_0 = \frac{1}{2\pi} \sqrt{\frac{k}{m_{eff} + \beta \Delta m}} \qquad (2.5)$$

where an added mass is Δm, k is the spring constant of the structure, m_{eff} is the effective mass, and β is a geometric constant.

This mechanism has been used for sensing the presence and mass of gas molecules [34], metals [40], and biomolecules [41]. As an example, Figure 2.7 shows a plot of the frequency response of a silicon resonator sensing the thickness of an added chrome layer of increasing thickness, up to 15 nm [40].
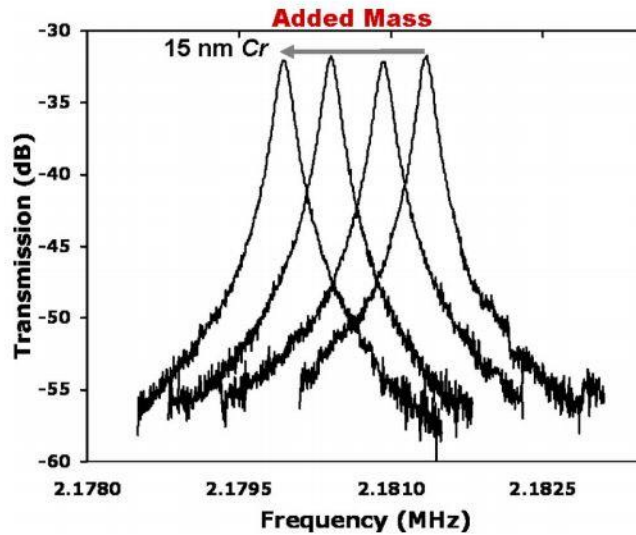
Figure 2.7. Frequency response of a silicon resonator with added mass. Image taken from [40].

Similarly to an addition of a mass Δm, a change in the stiffness k will cause a change in f, and this fact has been used in MEMS-based strain sensors to measure the strain caused by an applied pressure [31], and for condition monitoring [42] where an applied strain is measured.

2.2.2 Materials issues in resonator sensors

Silicon is by far the most widely used material in MEMS and NEMS resonator devices [43]. Its mechanical properties are well known, with a Young's modulus (*E*) of 169 GPa for the <110> direction [6] and a wide body of knowledge for its processing is available, such as etching and deposition. Silicon MEMS may be fabricated using silicon-on-insulator (SOI), which has a thin layer of single crystal silicon bonded to a layer of silicon dioxide [31]. The use of polycrystalline silicon (polysilicon) is also common in MEMS [44]. Polysilicon may be deposited using a gaseous precursor

through low-pressure chemical vapour deposition (LPCVD) using SiH$_4$ [45]. Polysilicon has an isotropic value of *E* of 160 GPa [6].

Figure 2.8 shows the variation of the *E* of silicon with temperature [3]. This graph shows a rapid decrease after 400 to 600 °C. This degradation in properties means that silicon may not be used in many harsh environments. Some applications where the use of MEMS sensors is sought after include combustion engines [46], in high radiation environments [47], and in the oil industry [48].
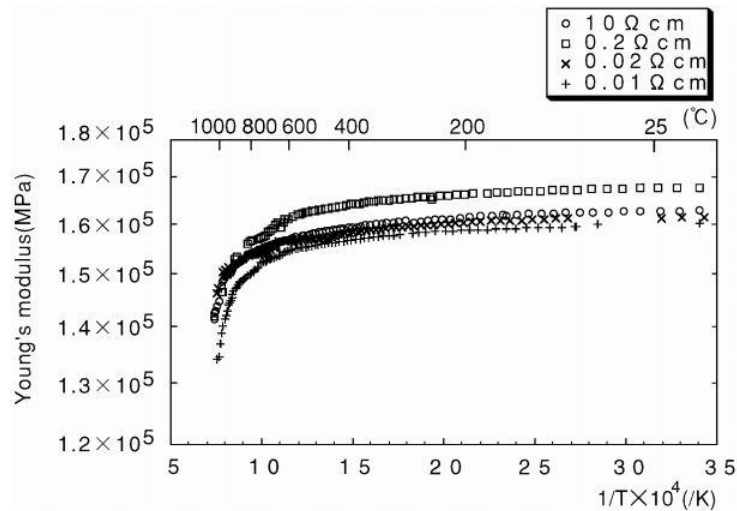
Figure 2.8. Variation of the Young's modulus of single crystal silicon of different resistivity. Image taken from [3].

Polysilicon may be deposited using a gaseous precursor through low-pressure chemical vapour deposition (LPCVD) using SiH$_4$ [45]. Polysilicon has an isotropic value of *E* of 160 GPa [6]. Amorphous silicon may be deposited using plasma-enhanced chemical vapour deposition (PECVD) at relatively lower temperatures than polysilicon (200 vs 500 °C) and has a Young's modulus of 110 to 159 GPa with recent application in MEMS resonators [49,50].

A recent development for MEMS and NEMS applications is towards the use of increasingly small and thin devices [51]. For example, graphite has been made into thin sheets of one single graphene layer, which is thermodynamically stable [52] even when released from its substrate. The silicon analogy for graphene, single and bi-layers of silicon (both known as 'silicene'), has recently been produced experimentally [53]. However, silicene is unstable in a flat state, which leads to buckling [4]. Therefore, with current technology it is very difficult to produce layers of silicon for ultra-thin NEMS structures.

Silicon carbide (SiC) is a stiff, strong, and chemically resistant material [46] with a Young's modulus of between 232 (amorphous SiC) [54] and 694 GPa (Single crystal SiC) [48]. SiC has had wide

interest in MEMS applications for use in harsh environments [46] and has been used in membrane-based pressure sensors [55] and in resonator-based sensors [56]. There is recent interest in creating ultra- thin layers of SiC [57,58] to a thickness of 0.5 to 3 nm. However, such ultra-thin samples have only been produced on a very small scale, with flakes measuring up to 2 µm. Thus, SiC may be a promising material for ultra-thin NEMS, but the synthesis of large-area samples currently requires further research.

2.2.3 Carbon materials for resonators

Silicon's poor performance at high temperature, and instability at very low thickness, has led research efforts for new MEMS and NEMS materials. A main group of materials under research for such applications are carbon-based materials.

Graphite and graphene, in particular, have been the subject of wide research for NEMS resonators, since graphene was the first ultra-thin 2D material [8]. This low thickness (and therefore low mass) may be used to increase the sensitivity of resonator-based sensors, as the change in frequency caused by an external force or mass depends, in part, on the total mass of a resonator. Graphite may also be used in harsh environments since it retains its mechanical properties well above 2000 °C [7].

Carbon-based materials have a broad range of properties which depends heavily on the bonding type and structure of the material. Diamond-based carbons with sp^3 bonds and graphitic carbons with sp^2 bonds have very different electrical and mechanical properties, and may be useful in different types of applications. In the following Section, the properties and applications of different carbon thin films used in MEMS and NEMS resonators is reviewed.

2.2.4 Planar graphitic materials

Graphitic materials are strongly anisotropic, with very high value of E within the plane (1060 GPa), and very low E out-of-plane (36.5 GPa) [5]. This is due to the mismatch in bond-types in the different planes, with in-plane covalent C-C bonds, and out-of-plane van der Waals forces [59]. Graphite also has high electrical conductivity, and when isolated to a single layer, graphene, it is the thinnest and strongest known material [60]. Due to these properties, graphene and thin film graphite show promise for MEMS and NEMS applications.

The methods for depositing graphene and thin graphite layers are diverse. These will be briefly reviewed here, along with how they have been used in NEMS devices. A summary is made in Table 2.1.

Method	Description with pros and cons
Mechanical exfoliation	This method yields single-layer graphene samples and has been used to produce NEMS resonators, but the small scale, random size distribution and poor control of strain mean that it is not feasible to widely produce devices based on this method.
Annealing of silicon carbide	Annealing SiC provides high quality graphene on an insulating substrate and may be undertaken on a large scale. The decomposition tends to create a 'terraced arrangement' with discontinuous films. The high stresses and fragility of the film mean that it is difficult to fabricate suspended NEMS structures using this type of film.
Chemical vapour deposition with transfer process	Large-area deposition and allows for production of a high quality film, but requires a catalyst layer. However, defects and strain from the transfer process have produced NEMS devices with poor performance.
PECVD deposition onto insulating substrates	The small grain size of nanographite leads to poorer electrical properties, but may be used for wafer-scaled deposition and is reproducible. There is limited amount of research on these films for NEMS in general and resonators in particular.

Table 2.1. Summary of methods used to synthesise thin film graphitic materials.

2.2.4.1 Mechanical exfoliation

Mechanical exfoliation (using friction to separate layers) has been used to create thin layers of graphite [61] with the aim of producing single layered sheets. This was achieved in 2004 [8], by using adhesive tape to repeatedly cleave highly-ordered pyrolytic graphite (HOPG) samples until a single layer was obtained. The flakes were then released from the tape in acetone and captured on a silicon dioxide (SiO_2) surface. This method can produce samples of a single crystal, without grain boundaries or defects.

Using exfoliation, Bunch *et al.* [62] fabricated 5 µm long NEMS resonators, which were actuated electrostatically, from graphite and graphene, with Q between 20 and 850 at pressure below 1 µTorr. They calculated the graphite/graphene to have a value of E of 1000 GPa, and fabricated resonators of thickness ranging from 75 nm to 0.3 nm (the thickness of a single sheet). This represents the thinnest material for resonators, for which the authors noted the good potential for mass sensing.

Mechanical exfoliation is a synthesis method which creates graphene and thin film graphite samples of good crystalline quality. However, the use of adhesive tape gives no control over the size or orientation of the sample, and the crystal size is typically of the order of 10µm. This method severely limits the ease, repeatability and scalability of fabrication using exfoliated graphite.

Due to the small size of graphene samples obtained using mechanical exfoliation, interest in more scalable methods which enable synthesis of large-area films has grown. To date, the most widely-used method to achieve large-scaled thin graphite and graphene growth is by using thermal chemical vapour deposition (CVD) onto nickel [63], copper [18] and germanium catalysts [19]. In CVD, hydrogen mixed with methane (CH_4) is used to deposit graphene at temperatures of 900 to 1000 °C, where carbon is dissociated from the CH_4. The carbon then forms a graphene or graphite film on the catalyst substrate.
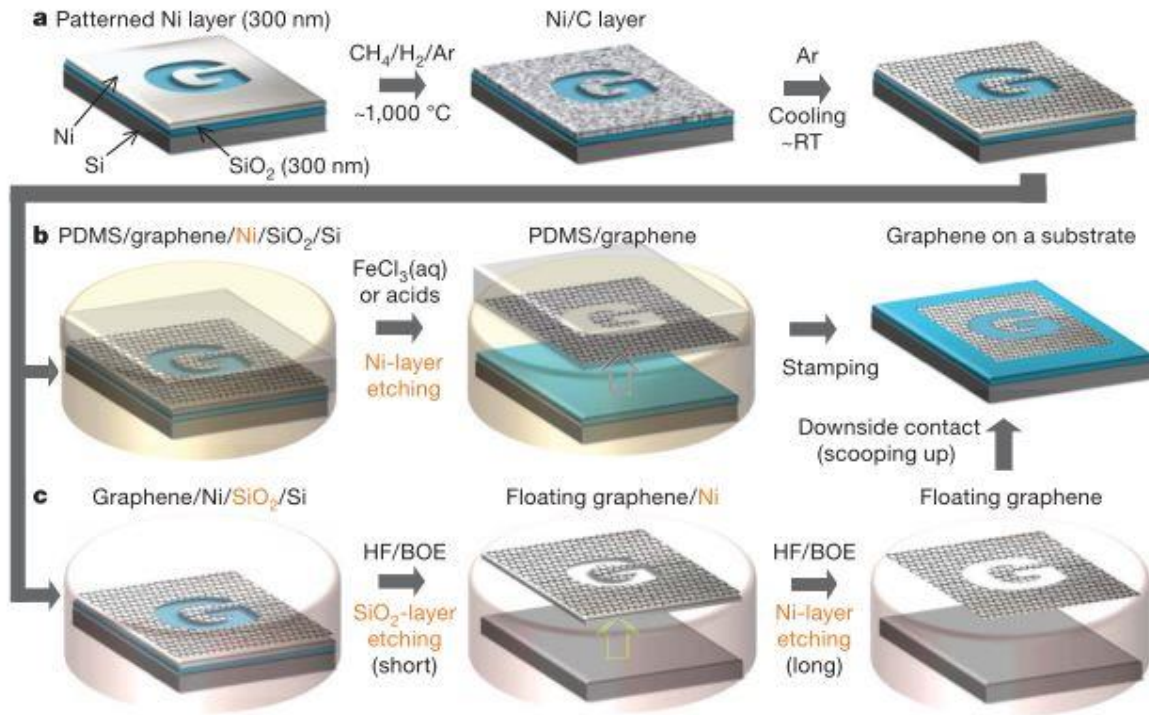
Figure 2.9. Schematic of methods to synthesis and transfer graphene using a nickel catalyst. Image adapted from [17].

Before it can be used in any device, the graphitic film must be removed from the catalyst and transferred to a different substrate, such as silicon coated with SiO_2. For metal catalysts, this can be done on a large scale [8] with a polymer support adhered to the graphene/catalyst. The catalyst is then etched leaving graphene-on-polymer, which can then be transferred to a desired substrate, as shown in Figure 2.9. For the germanium catalyst [19], a simpler dry transfer may be used to move the layer to the intended substrate.

Graphene grown using thermal CVD onto a copper substrate has been used to fabricate large arrays of graphene resonators, as shown in Figure 2.10 [64]. These had dimensions of 2×3 µm and Q of 25 to 250 at pressure below 50 µTorr. Whilst the transfer process from copper to silicon substrate has been performed on a relatively large scale, the quality of the graphene resonators was reduced in

this process. The devices suffered poor repeatability between nominally identical devices, and many suffered tears and failed. This was due to wrinkles and defects introduced during the synthesis and transfer process. The variation of strain across the material also caused large variation in the resonant frequency of devices fabricated using this method [64].

The use of the germanium catalyst and subsequent dry-transfer may help to eliminate some of the wrinkles, defects and poor reproducibility in graphene NEMS. However this has not currently been investigated, and it is unclear whether the strain over a wide area is homogenous.
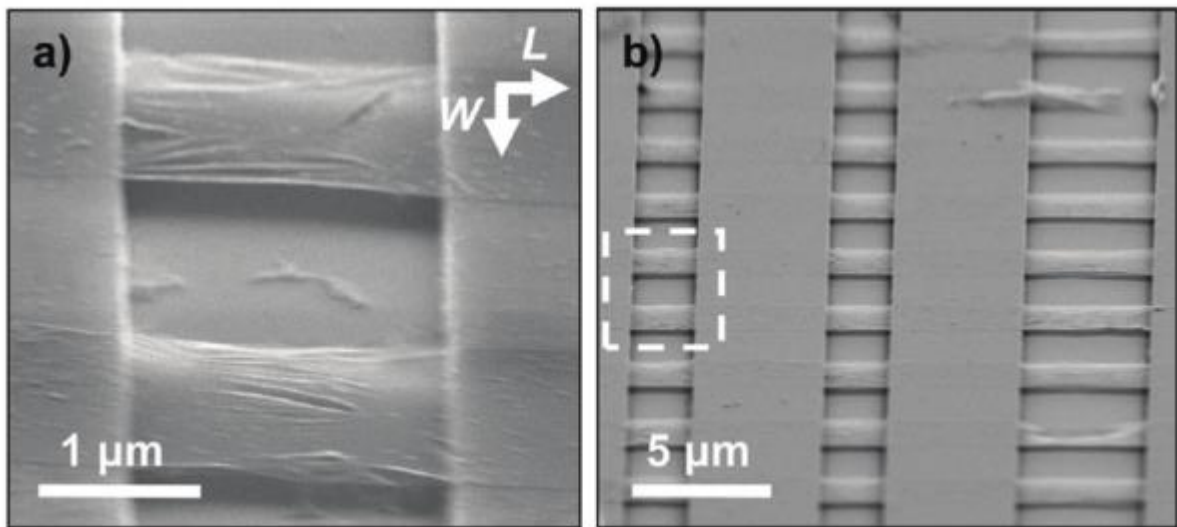
Figure 2.10. SEM images of arrays of graphene resonators, suffering from tears and wrinkles. Image taken from [64].

2.2.4.3 Plasma-enhanced chemical vapour deposition of graphitic materials onto insulating substrates

Plasma-enhanced chemical vapour deposition (PECVD) has been used as a more scalable method to deposit graphitic thin films onto a range of substrates, including silicon and SiO_2 [21,22,65,66]. PECVD has been used to deposit continuous and ultra-thin nanographene films of thickness as low as 2.5 nm [21] to 3 nm [22]. Since the deposition is directly onto the intended substrate, this removes the need for transfer of the film between substrates as with thermal/catalytic CVD.

In PECVD, a gaseous carbon precursor such as CH_4 is introduced into a plasma reactor, and many of the molecules in the gas are ionised through an applied RF electric field. This dissociates the CH_4 into different carbon-containing radicals, which then nucleate on the substrate as graphite islands. The islands grow into crystallites in the order of 10 to 50 nm in diameter [66]. A H_2 diluent is often used in the plasma reaction as the H_2 acts to etch weaker bonds in the film and promote sp^2 carbon growth [66]. Temperatures in PECVD have been employed from 400 to 900 °C. These films are

termed nanocrystalline graphite/graphene or nanographite/nanographene/NCG for brevity. Nanographite films are electrically conducting, with a resistivity of around 30 mΩ·cm and display piezoresistive behaviour [67]. A summary of different results for the electrical and structural properties of different nanographite/nanographene films is detailed in Table 2.2.

The use of PECVD nanographite films in resonators and NEMS in general has been limited. Recent research by Sun *et al.* developed 5 nm thick nanographite films for NEMS-based switches, based on buckled doubly-clamped beams [68], with a low pull-in voltage and uniform film thickness. Sun *et al.* extracted a value of 860 GPa from the pull-in behaviour of the beams; however, this is an *effective* value, which does not take into account the stress or buckled shape of the beams.

Group	Deposition method and temperature (°C)	Electrical resistivity measurement	Grain size (method of determination)	Notes
University of Southampton [22][68].	PECVD, 750 to 900	29 mΩ-cm 13k Ω per square at 6nm on quartz	2.2 to 2.7 nm (Raman analysis)	Uniform thickness across 6-inch wafer. Application for NEMS switches.
Chinese Academy of Sciences, Beijing group [67][66]	Remote-PECVD, 550	40 kΩ per square	Few to ~50 nm (AFM)	Piezoresistive measurements show a gauge factor of up to 300.
National Tsing Hua University group [69]	Electron cyclotron resonance CVD, 400	20 kΩ per square	2 to 3 nm (Raman/TEM)	Low deposition temperature.

Table 2.2. Summary of the deposition and properties of some graphitic thin films deposited by PECVD.

2.2.4.4 Graphitic films from the annealing of silicon carbide

SiC is widely manufactured in the form of single crystal, wafer-scale substrates, and it may be used as a template for graphitic film growth. Annealing SiC in an argon atmosphere [70] is a route for graphene and graphite growth. Using this method, the silicon evaporates from the substrate, thereby leaving a graphene/graphite layer on the top of the SiC substrate. The formation of graphene occurs on long thin 'steps' or terraces of width ~3 μm and length 50 μm which follow the crystallographic orientation of the substrate, and does not form one continuous film over the wafer. This greatly limits the fabrication of devices, as they need to be contained within the terrace.

Shivaraman *et al.* [71] fabricated doubly-clamped nanomechanical resonators from thin films of graphite (of a few layers) grown on SiC substrates, as shown in Figure 2.11. The resonators had

lengths of 3 to 20 µm and Q up to a maximum of 1000 (but typically between 50 and 400) at pressure of around 10 µTorr. The repeatability of fabrication was poor. For example, many devices were observed to have 'crinkled' doubly-buckled geometries as a result of high stress and difficulty in etching SiC.
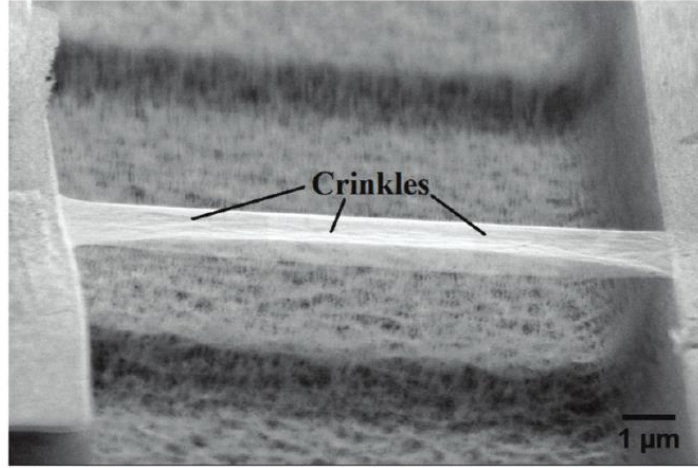
Figure 2.11. SEM image of a doubly-clamped few layered graphene beam, made from SiC. Crinkle defects are highlighted. Image taken from [71].

2.2.5 Diamond

Diamond has a value of E of 1035 GPa [72], high strength, and chemical inertness, and is therefore a robust material for harsh-environment sensing [73]. There are various methods to deposit diamond films including microwave plasma-CVD (MPCVD) [74], hot-filament CVD [74], and PECVD [75]. Diamond is a wide band-gap semiconductor and may be doped with, for example, boron [76], to give it electrically conducting properties.

Tao *et al.* [77] fabricated nanomechanical resonators using cantilevers made of high quality single crystal diamond for measuring force or mass, as shown in Figure 2.12. These cantilevers were of length 20 to 240 µm and had maximum Q of 1.2 million, at room temperature and pressure below 1 µTorr. These cantilevers were fabricated by bonding a single crystal diamond onto a silicon substrate, before patterning and release. Single crystal diamond cannot currently be readily deposited onto another substrate, and in this research, a relatively thick layer was bonded and subsequently thinned by etching. This may be a plausible route of fabrication for certain niche applications, though it is difficult to foresee this being used for large-scaled production, due to the complexity of producing large-sized diamond-on-insulator substrates.
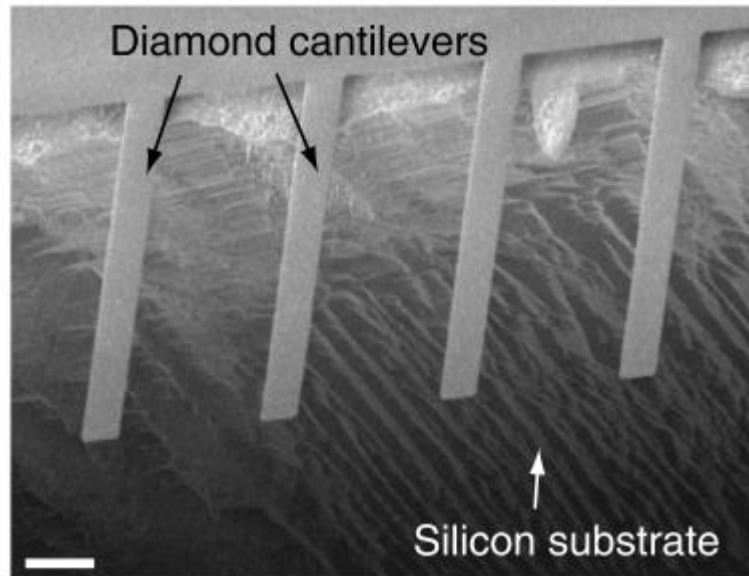
Figure 2.12. Image showing nanomechanical diamond resonators fabricated from single crystal diamond. Image adapted from [77]. Scale bar is 20 µm.

Nanocrystalline diamond films (NCD) represent a more scalable diamond thin film as it may be deposited onto a substrate from a CH_4 precursor. NCD was deposited using MPCVD at 750 °C onto a Si/SiO_2 wafer and machined into NEMS resonators by Sekaric *et al.* [78]. These devices had lengths of 1 to 8 µm and Q of 2400 to 3500 at a pressure of about 1 µTorr. Larger-grained polycrystalline diamond (PCD) films have been grown by Sepulveda *et al.* using MPECVD [79]. PCD films require a nanoparticle seeding layer for the diamond growth. The resonators grown using this method had lengths of 90 µm and a Q of around 10,000 at 1 µTorr pressure.

Currently, obtaining ultra-thin layers of NCD and PCD films is problematic. In research by Yoshikawa *et al*. synthesis of NCD films of 14 nm thickness [80] contained pinholes, and a thicker layer (>30 nm) was required for films without a significant number of pinholes. Therefore, it is currently difficult to deposit NCD films of ultra-low thickness which are of sufficient quality for NEMS applications.

PECVD and MPECVD represent large-area deposition methods for fabrication of diamond-based MEMS and NEMS. The relative Q of each also highlights a common trend for thin film MEMS and NEMS: the more reproducible and scalable fabrication is at the cost of a smaller grain structure. A small grain structure considerably reduces Q compared with a single crystal film. Conversely, more complex synthesis routes generally enable films of better crystallinity.

Diamond-like carbons (DLC) include a range of materials and include a mix of diamond and graphitic-type bonding. Figure 2.13 shows a ternary phase diagram which denotes most of the main groups of DLC films [81], such as tetrahedral carbon (ta-C) and hydrogenated tetrahedral carbon (a-C:H). The mechanical properties may range from being similar to graphite or similar to diamond, and with a similar variation in electrical properties. DLC may have a value of E varying from 160 GPa [82] to 757 GPa [83].
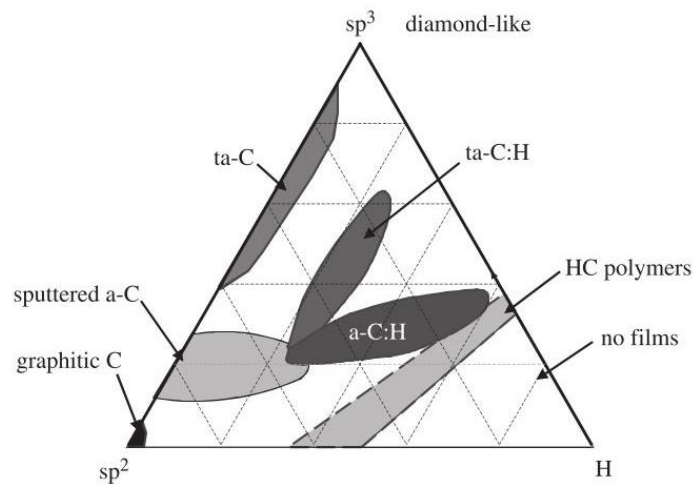
Figure 2.13. Ternary phase diagram of carbons. The corners correspond to graphite, diamond and hydrocarbons, respectively. Image taken from [81].

DLC is commonly deposited using PECVD [84], sputtering [85] and filtered cathodic vacuum arc [86]. These are all easily scalable methods of deposition over large-area substrates, and have been used to fabricate high frequency, electrically-actuated and integrated NEMS resonators, of length 1 µm and with a Q of 1400 at a pressure below 10 µTorr [82]. An image of a DLC resonator is shown in Figure 2.14 (A), and it can be seen that the high built-in stress of the film caused it to buckle. DLC thin films often have extremely large stress states (2 to 11 GPa) [82,86]. The stress state of DLC has greatly limited the use of this material within MEMS, since this leads to buckling [82], and delamination, as shown in Figure 2.14 (B) [86].
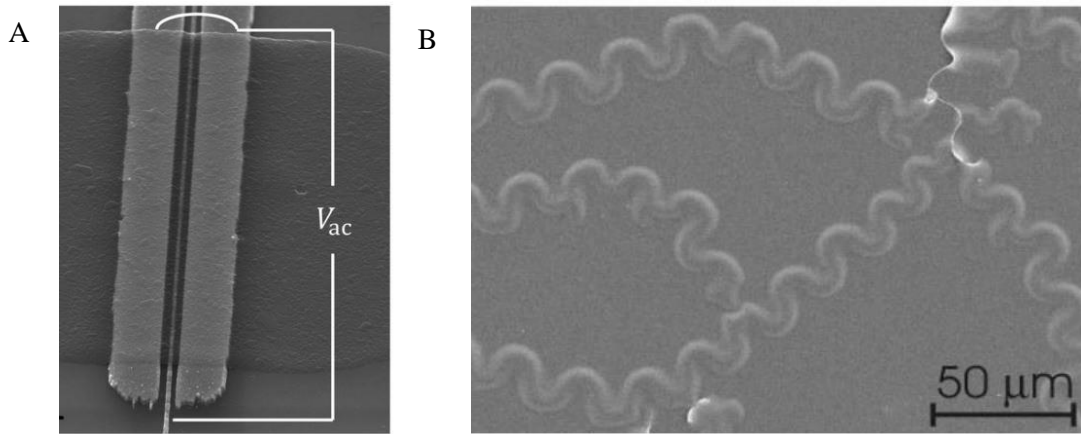
Figure 2.14. (A) Image of a buckled DLC resonator. Image taken from [82]. (B) Example of delamination from the substrate caused by very high compressive stress in a DLC film prepared using cathodic vacuum arc. Image taken from [86].

2.2.6. Further applications for carbon-based probes.

Whilst the bulk of this literature survey has focused on the use of carbon thin films for resonator applications (which primarily require values of high f_0 and Q), the wide spectrum of carbon properties such as low mass [87], low friction [88] and negative thermal expansion [89] have shown promise for a range of applications beyond resonators, such as atomic force microscope (AFM) probes [90], actuators [91] and nanoelectromechanical switches. For example, DLC coatings have been used as a coating for silicon AFM cantilevers [90]. In this application, the high value of Young's modulus of DLC (616 GPa) raised the resonant frequency of the cantilever, and also increased the wear life of the tip because of DLC's higher hardness compared with standard AFM materials such as silicon or silicon nitride. Graphene films, grown using thermal CVD were used in bimorph cantilever actuators with epoxy [91], here the difference in thermal expansion between and graphene and epoxy, and the low Young's modulus of the epoxy enabled large deflections of cantilever. Loh *et. al.* [92] fabricated nanoelectromechanical switches using two forms of carbon: a carbon nanotube (CNT) cantilever and a DLC contact electrode. Here, the low cross-sectional area of the CNT cantilever enabled a switch with a pull-in voltage of 23 V and the low friction characteristics of the DLC helped to reduce stiction of the device, thereby increasing its lifetime.

<u>2.2.7 Conclusions for the literature based on the application of resonators</u>

Resonators are promising devices for use as sensors of force and mass. The search for more sensitive and more durable devices has led to wide-ranging research into materials beyond the traditionally-used silicon. Some carbon thin films: graphite, diamond and DLC, all have promising properties and have been reviewed here.

Diamond shows high promise as a material for resonators, particularly with single-crystal devices showing very high values of Q. However, it is difficult to obtain thin films of single crystal diamond. Other routes of deposition such as PECVD and MPECVD are relatively easily employed to deposit NCD films directly onto substrates, and have been widely researched. Currently, continuous ultra-thin NCD films cannot be deposited using PECVD or MPECVD. DLC typically has poor electrical performance and exhibits extremely large states of stress which makes fabrication of released devices very troublesome.

Graphitic thin film materials are a promising route for future carbon-based MEMS and NEMS devices for two main reasons:

- These materials may potentially be used in harsh environments, enabling sensing of a number of applications which have been 'off-limits'.
- Ultra-thin graphite and graphene films may be deposited at lower thickness than the other carbon materials. Such thin films can be used to fabricate stable suspended structures, without buckling. The very low mass of ultra-thin devices may facilitate sensors of greater sensitivity.

Graphitic thin films of high quality may be obtained using metal or germanium catalysts; however, the transfer to an appropriate substrate leads to poor performance, particularly with variation in strain. PECVD is a method used to produce electrically-conducting nanographitic thin films directly onto insulating substrates, and at temperatures as low as 400°C. This type of film has been recently used for NEMS switches [68], which in terms of fabrication, has many similarities to how one may fabricate a resonator. The devices in this study were buckled, which creates difficulty in modelling and designing devices, since the behaviour becomes nonlinear. Buckled devices are also likely to be more fragile due to the large strain of the material. However, this work shows the promise of fabrication of MEMS and NEMS using nanographite thin films, though clearly more research is required. In particular the following are areas of interest:

1. To measure the mechanical properties of nanographite and to characterise its performance within MEMS and NEMS applications.
2. To demonstrate routes of fabrication of nanographite in particular, and carbon thin films in general, which are reproducible and do not suffer from buckling.

2.3 Membranes for gas separation

Hydrogen is an alternative fuel to commonly-used hydrocarbons such as methane and natural gases, and is seen as advantageous because its byproducts after combustion do not include CO_2 which is predicted to increase the effect of the greenhouse effect in global warming [93]. The limited usage of H_2 as a commercial fuel is largely due to the energy-intensive methods used to produce it. The most commonly-used method currently to produce H_2 involves obtaining it from hydrocarbons [94]. This process leaves a gaseous mix of H_2 and CO_2. Cryogenic distillation is then used to separate these two components; an energy-intensive process which limits its economic viability [95]. Another gas, helium, is widely used in medical and industrial fields. The vast majority of He is extracted from natural fields, where it is found as a mixture with other gases such as nitrogen [96]. Helium is then typically purified using cryogenic distillation, as with H_2. Less energy-intensive methods of production are sought after for both these gases, with membrane separation being a widely researched and promising technology method [97–100].

Permeable membranes are thin sheets of a porous material which may be used as filters to separate different molecules. The molecules are commonly sorted by size, mass and charge [101]. Membranes with an average pore size, for example, between that of the molecular size of H_2 and CO_2, provide greater resistance to the flow of CO_2 than H_2. These are known as molecular sieve membranes. Some materials, such as carbon, adsorb certain materials much more strongly than others, and this can be used to provide different flow rates [102]. Figure 2.15 shows a schematic of some types of materials which have been used for gas separation.
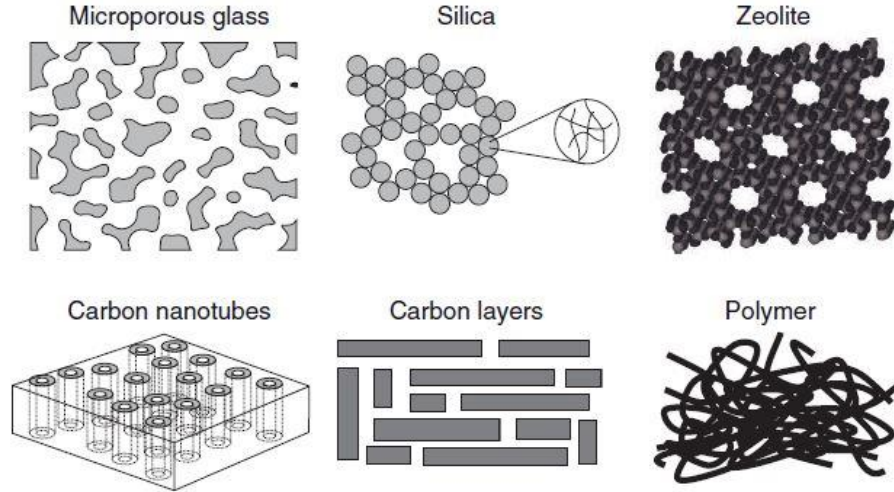
Figure 2.15. Schematic of various types of crystal structure which is used to filter gases. Image taken from [13].

For the ideal separation of H_2 and CO_2, for example, the flux (which is the flow of molecules, per unit time, through the membrane) of H_2 should be large, and the flux of CO_2 should be small. The ratio between these two is called the selectivity or separation factor ($\alpha_{H2/CO2}$). Typically there is a trade-off in the permeability and selectivity of membranes [103], whereby materials with higher permeance of H_2 tend to have a lower value of $\alpha_{H2/CO2}$. Another requirement for membranes for H_2 separation is the ability to withstand conditions of elevated temperature [104].

Polymeric membranes, in particular, have been very widely researched for these gas separation applications [103], as they are cheap to produce on a large scale. However, polymeric membranes may degrade at high temperature, and offer a limited trade-off between permeance and α. For example, Figure 2.16 shows a trade-off graph for $\alpha_{H2/CO2}$ which includes the 'Robeson's upper bound' indicating the empirical best achievable trade-off for polymeric membranes [103].

The permeation unit here is the Barrer, which is a thickness-normalised unit of permeability $\left(\dfrac{flux \cdot thickness}{area \cdot \Delta pressure} \right)$. One Barrer is equal to $10^{-10} \dfrac{cm^3(STP) \cdot cm}{\sec \cdot cm^2 \cdot cmHg}$ [105] (1 mol $\cdot$ m $\cdot$ m^{-2} $\cdot$ s^{-1} $\cdot$ Pa^{-1} is equal to 2.99×10^{-15} Barrer [106]). This unit enables comparison of the intrinsic material characteristics, since the thickness of the membrane is accounted for. However, more commonly the unit (mol $\cdot$ m^{-2} $\cdot$ s^{-1} $\cdot$ Pa^{-1}) is used in the literature. This unit gives $\left(\dfrac{flux}{area \cdot \Delta pressure} \right)$ and is not normalised to thickness.
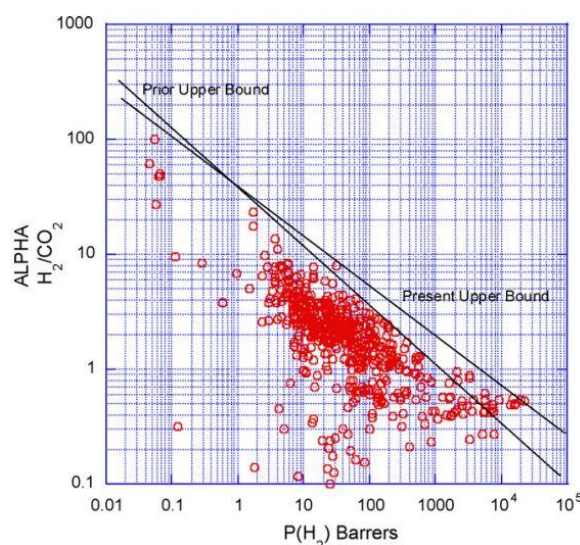
Figure 2.16. Graph showing the H_2 permeation and H_2/CO_2 separation behaviour of many polymeric membranes, with the empirical trade-off between permeability and separation. Image taken from [103]. The 'prior upper bound' represents the best performance in 1991, and the 'present upper bound' in 2008.

The performance limitations of polymeric membranes has led to a wide search for materials which offer higher levels of flux and selectivity, and which may be used at higher temperature. Figure 2.17 shows the behaviour for H_2/CO_2 separation of some inorganic membranes. Note the higher values of selectivity α achievable from some of the inorganic membranes compared with the polymeric membranes (Figure 2.16). The data points in this graph act as a reference for the following reviewed membranes. Membranes with results raising towards the top-right corner of the graph (marked by the star) in Figure 2.17 are sought.

A - [16] – Graphene oxide
B - [104] – Silicon carbide
C - [174] - Zeolite
D - [108] - Silica
E - [111] - MOF
F - [107] – Silica titania
G - [110] - MOF
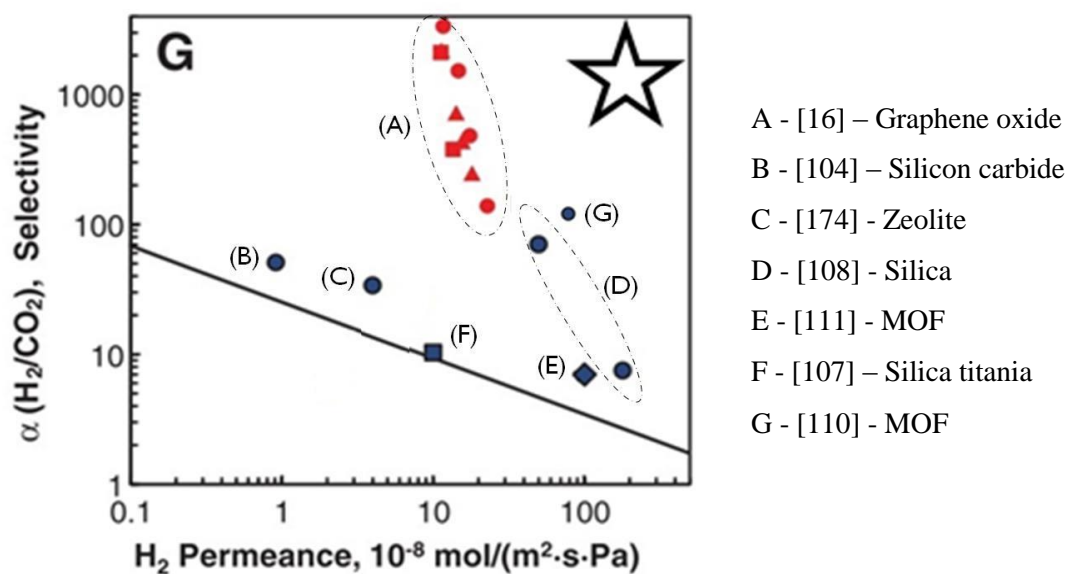
Figure 2.17. Graph showing the H_2 permeation and H_2/CO_2 separation behaviour of some inorganic membranes. The black line represents Robeson's upper bound for the behaviour of polymeric membranes [103]. The star represents the ideal separation performance. Image adapted from [16].

24

2.3.1 Materials for membranes

The following Section sets out a short overview of some promising membrane materials for gas separation based on the abovementioned trade-off in the behaviour of such membranes. Readers should note that the overall literature extensively covers the performance of membranes separating H_2/CO_2, whereas He separation is far less studied. As a result, most of the behaviour described in this Section relates to H_2/CO_2, thereby enabling comparison of the performance of different membranes.

2.3.1.1 Silicon composite membranes

SiC is a material which is mechanically stable at high temperature ($> 350°C$) [46] and as a result it is a potentially useful material for membrane gas separation, where high temperatures are often used. Elyassi *et al.* [104] characterised SiC membranes prepared by pyrolysis onto an aluminium oxide support. The membranes had reasonable $\alpha_{H2/CO2}$ of ~50, but a relatively small permeance of 1.2×10^{-8} mol m^{-2} s^{-1} Pa^{-1} at 200 °C. This performance is similar to the polymeric upper bound, and the low permeance of H_2 has currently limited the use of SiC membranes.

Silica-titania membranes (20 nm thick) were investigated by Gu *et al.* [107]. These membranes were produced using thermal CVD and possessed H_2 permeance of 24×10^{-8} mol m^{-2} s^{-1} Pa^{-1} but a poor $\alpha_{H2/CO2}$ of 14. De Vos *et al.* [108] produced silica membranes through isostatic pressing of powders. These membranes showed very high H_2 permeance of 200×10^{-8} mol m^{-2} s^{-1} Pa^{-1} at 200 °C, but a low $\alpha_{H2/CO2}$ of 7.5.

In all cases, silicon-based composite membranes were simple to fabricate on a large scale and possessed stability at elevated temperature. However, the trade-off in performance is similar to that achieved by the upper-bound of polymeric membranes.

2.3.1.2. Membranes based on metal-organic frameworks

Metal-organic frameworks (MOFs) are porous materials which comprise metal ions or clusters connected with organic linkers. They are currently the subject of wide research for membrane-based gas separation technology [109].

Peng *et al.* [110] fabricated nanometer-thin MOFs sheets based on zinc, and an example of a membrane is shown in Figure 2.18. These membranes had H_2 permeance of 91×10^{-8} mol m^{-2} s^{-1} Pa^{-1} and $\alpha_{H2/CO2}$ of 291 at 120 °C. These results show strong promise for gas separation. However, the membranes did not appear to possess robust mechanical behaviour (to ensure stability, the authors applied no absolute pressure differential across the membrane). Regarding temperature stability, the performance rapidly dropped at elevated temperature, with permeance decreasing by a factor of 3.6 *and* $\alpha_{H2/CO2}$ dropping by a factor of 5.5 when the temperature increased from 120 °C to 200 °C. The narrow band of conditions which facilitated high performance show that this type of MOF may currently be too specialised for usage under real-life conditions.
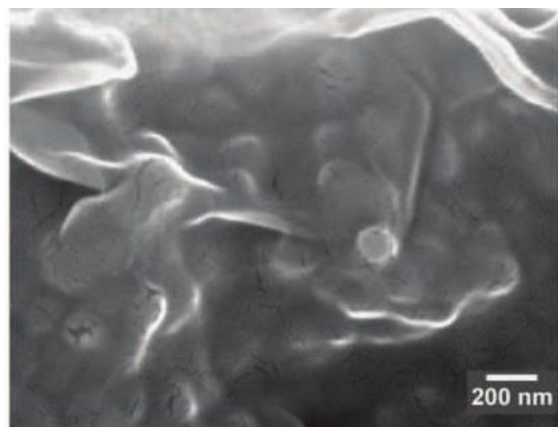
Figure 2.18. SEM image showing a zinc-based MOF membrane on a porous support. Image adapted from [110].

Guo *et al.* [111] constructed copper-based MOFs with high quality crystals of 5 to 10 µm diameter, which were formed over a copper mesh; a relatively simple technique for producing MOF membranes. The membrane gave very high H_2 permeation values of ~1×10^{-1} mol m^{-2} s^{-1} Pa^{-1}, but poor $\alpha_{H2/CO2}$ of ~7. The membranes were tested between room temperature and 70 °C, with no reliable demonstration of permeation behaviour at elevated temperatures.

MOFs represent a specialised system for gas separation, with very high fluxes and high separation values shown to be obtainable. Currently, MOF membranes appear to show high performance only within a narrow band of temperature operation. The degradation in properties shows they currently lack the robust material characteristics to withstand high temperatures and pressures to filter gases industrially, though they clearly represent a very promising technology for membrane gas separation.

2.3.1.3 Carbon materials for membranes

Carbon has, for decades, been widely researched and used as a material for gas and ion separation [112]. For many types of carbon membranes, polymeric precursors are graphitised to produce a

carbon graphitic framework. Carbon's chemical [113] and temperature stability [7] ensures it has a wide window of operation compared to, for example, MOFs.

Carbon membranes may have different adsorption characteristics for different materials [102]; for example, hydrocarbons are more strongly adsorbed than H_2 [102]. Selective adsorption can be used as a separation mechanism, whereas silicon and MOF membranes primarily rely on molecular sieving (filtering molecules by their size). The differential absorption behaviour has been utilised in carbon membranes derived from PVC [102] which is shown in cross-section in Figure 2.19. In this work, the high adsorption of hydrocarbons relative to H_2 gave an 'inverse' selectivity for H_2/C_4H_{10} of 0.01, despite H_2 being a much smaller molecule (2.89 Å vs 5 Å [114]).
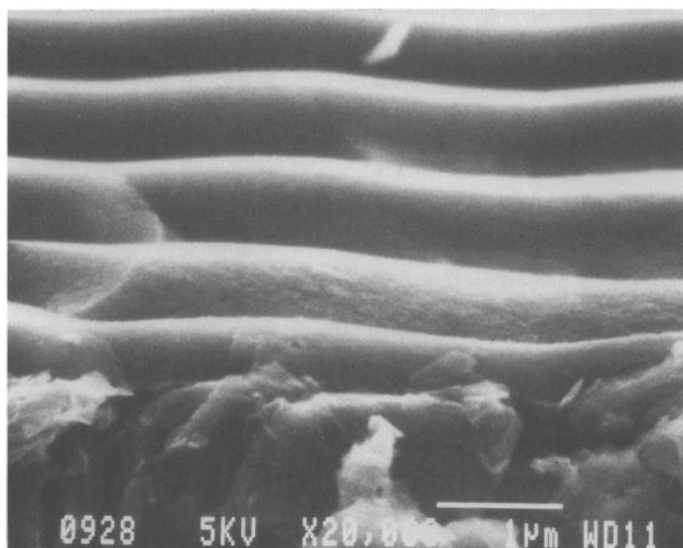
Figure 2.19. SEM image of a cross section of a carbon membrane derived from PVC. Image taken from [102]

The use of very thin carbon films such as graphene has opened up a range of materials which may offer high permeability for gas separation based on low thickness. Such films may also be designed and altered using micro- and nano-fabrication technologies such as focused ion-beam milling (FIB) [115], ultraviolet (UV) etching [12] and substrate patterning [15].

The massive amount of research in graphene and related materials has extended to the development for gas separation technologies. Li *et al.* [16] used graphene-oxide, derived from exfoliated graphene-oxide powder, on anodic aluminium supports. The membranes had a minimum thickness of 1.8 nm. However, despite the low thickness, the H_2 and He permeance were similar to SiC membranes of a much greater thickness (2 µm thick [104]). The 1.8 nm membranes had a H_2 permeance of about 20×10^{-8} mol m^{-2} s^{-1} Pa^{-1} at 100 °C and 10×10^{-8} mol m^{-2} s^{-1} Pa^{-1} at 20 °C.

However, $\alpha_{H2/CO2}$ was around 20 at 100 °C, reduced from a high value of ~2000 at 20 °C. Thus, the trade-off in performance is poor at higher temperatures, which is more likely to be the case for real-life applications. The sieving behaviour was attributed to intrinsic defects in the graphene-oxide lattice. The relatively modest value of H_2 flux may demonstrate that the crystal structure of ~ 500 nm sized flakes is not optimal for high flux of H_2.

The use of thin film graphitic materials also opens up different routes of fabrication and modification which are more often associated with NEMS. For example, Koenig et al. [12] made 5 µm diameter freestanding membranes of single crystal exfoliated graphene, and created pores in the graphene (which initially was free of defects) using UV etching. An AFM image of the porated graphene is shown in Figure 2.20. The use of UV etching enabled the pore-size to be designed and were made between 3.4 to 4.9 Å.

The drawbacks in synthesis methods which were discussed for graphene NEMS resonators equally apply to graphene membranes. Mechanically-exfoliated graphene may only be produced in very small crystals. Graphene grown using CVD has grain boundaries which strongly alter its gas permeance [116] and the defects which arise from the transfer process also inhibit selective gas permeance [14].
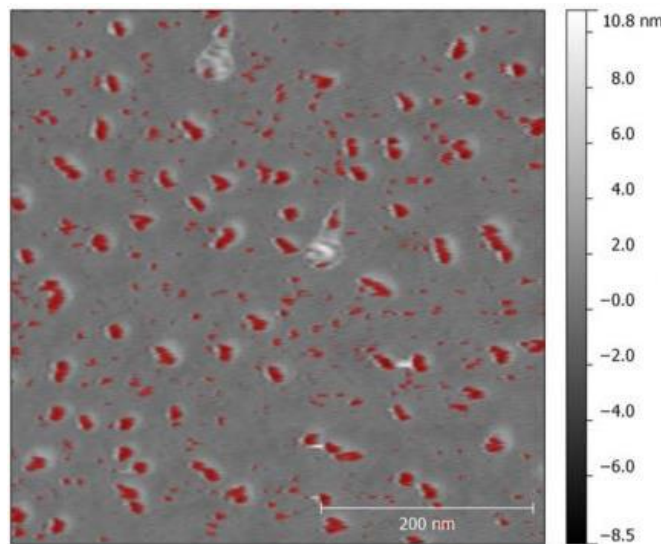
Figure 2.20. AFM image of a porated graphene surface, where the red areas are pores made by UV etching. Image taken from [14].

2.3.2 Conclusions of the literature based on the application of gas-separation membranes

Membranes for gas separation is a widely researched field, and it is clear that many different classes of materials, including silicon composites, MOFs and carbons show high levels of promise for gas separation technologies and specifically for H_2 and He separation. Conversely, each of the

researched material groups have some areas which require further research. Table 2.3 briefly summarises the properties of each of the reviewed inorganic materials for membrane gas separation.

Material	Description with summary
Silicon composites [104][107][108]	Materials such as silicon-carbide, silica-titania and silicon-oxide (silica) all possess good material stability at high temperature, and may be fabricated relatively simply. The trade-off in H_2 flux versus selectivity is fair, and similar to polymeric membranes.
MOFs [109][110][111]	MOFs are an emerging material for membrane gas separation, and there is wide interest in methods to fabricate them. Some membranes show very good combination of H_2 flux and selectivity. However the behaviour typically degrades at higher temperatures, and very thin MOF membranes do not currently appear very mechanically robust.
Carbon [112][102][115][14]	Carbon membranes based on polymeric precursors have been used for some time. They offer high temperature stability. The large amount of research on graphene and related materials has led to the use of graphene-oxide. However it has relatively low flux for such a thin material, and the separation behaviour degrades at higher temperatures. Use of nanotechnology-based fabrication of membranes, such as using pre-patterned silicon substrates for support and UV etching to create pores, offers promising new routes for membrane fabrication. However, the scalability issues which led to poor reliability of graphene NEMS also affect membranes.

Table 2.3 Summary of the behaviour trends of the reviewed membrane materials.

Carbon-based materials are promising materials for gas separation with attributes of high temperature resistance and chemical stability, and may separate gases using differential absorption [102] and/or through size-based molecular sieving [16]. Recent work on the use of fabrication technologies which are more closely associated with nanotechnology, such as FIB milling and UV etching, have shown promise for modification of thin graphitic films. However, many of the fabrication issues associated with graphene NEMS, such as its troublesome transfer process and inherent fragility, are also drawbacks for the use of graphene for gas separation technology.

Further work is required to utilise thin film graphitic membranes. The intrinsic defects in graphene-oxide have shown to be selective for H_2/ CO_2. However, the large flake size yields relatively few defects and the relative permeance of the material is low. Nanographite may have a much higher defect density than graphene-oxide, due to its low crystallite size, and PECVD offers wide-area deposition. Thus, nanographite films deposited on silicon substrates may be used as membranes

which: (A) filter gases through intrinsic defects and (B) can be used as a material to be altered using NEMS-type fabrication (such as UV etching). This literature survey has highlighted that it would be useful for further research to be conducted in the following two areas:

1. The demonstration of methods to fabricate nanographite-based membranes. This can be an 'enabling technology' for combining MEMS- and NEMS-type fabrication and modification of membranes, with a scalable deposition method.
2. The measurement of the permeability and separation behaviour of H_2 / CO_2 and He through nanographite membranes.

To summarise, this literature review has highlighted areas of research whereby the use of nanographite thin films show promise for: (A) use as a material for MEMS/NEMS resonator-based sensors, and (B) for membrane gas separation. The following Chapters in this Thesis describe the work undertaken towards these aims.

3. Experimental techniques

Here, the methods used to fabricate structures and devices which have been used for experiments in this research are presented. Subsequently the experimental methods used to analyse them are detailed.

3.1 Deposition of nanographite using plasma-enhanced chemical vapour deposition

This Thesis focuses on the characterisation of nanographite thin films for MEMS-type applications. The synthesis of this film is based on prior work in the University of Southampton [22]. The use of a commercial PECVD tool (Oxford Instruments Nanofab1000 Agile), as shown in Figure 3.1, enables a repeatable method for depositing films over a large, commercial type substrate, and in this work either 6-inch silicon wafers or 4-inch fused quartz wafers were used.
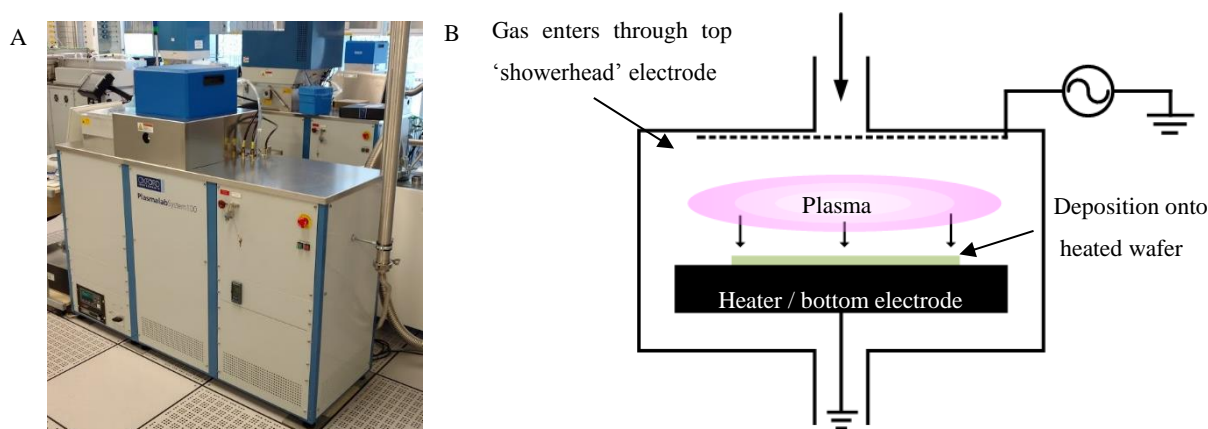
Figure 3.1 (A) Image of the Oxford instruments Nanofab1000 Agile PECVD tool used to deposit nanographite films (photo credit, Dr Ahmed Abuelgasim) (B) Schematic of the PECVD system for film deposition.

The deposition conditions are summarised in Table 3.1. The carbon precursor is CH_4, which is dissociated into various free radicals such as CH_x , C_2H_y , C_3H_z during the reaction [66]. The H_2 acts as a diluent, controlling deposition rate and promoting graphitic carbon growth by etching amorphous carbon [21]. The relatively high deposition temperature of 750 °C was used, since this was the minimum temperature to obtain graphitic carbon growth using this tool. Below 750 °C amorphous carbon was formed, or no deposition took place. A deposition rate of approximately 2 nm per minute was measured with the conditions described in Table 3.1.

Temperature (°C)	750
RF power (W)	100
Chamber pressure (mTorr)	1500
CH$_4$ flow (sccm)	75
H$_2$ flow (sccm)	60

Table 3.1. Summary of PECVD deposition conditions for nanographite.

3.2 Fabrication of nanographite structures

The following subsections detail the fabrication of three different types of nanographite structure:

- Fabrication of doubly-clamped buckled beams.
- Fabrication of a MEMS resonator structure.
- Fabrication of membranes.

All devices were fabricated using 6-inch standard P-type silicon wafers, excepting the membranes for gas permeation, which were deposited using 4-inch fused quartz wafers. UV photolithographic exposure was used throughout for patterning and aligning.

All masks were newly designed for this body of work, using L-edit software. The mask sets for all samples, excepting the fused quartz membranes, were printed transparency masks (Microlitho Ltd., U.K.) with minimum feature size of 10 µm. The fused quartz membranes were exposed using chrome on soda-lime glass photomasks, made in-house in the SnFPC, IMRE, A*STAR, Singapore.

For the avoidance of repetition, some common fabrication procedures are listed here:

- For devices fabricated using silicon substrates, each wafer was cleaned for 10 minutes using fuming nitric acid to remove organic contaminants.
- Prior to resist spinning, the wafer was dehydrated for 20 minutes in an oven at 210 °C.
- Complete etching of films is confirmed using ellipsometry and stylus profilometry.
- Recipes, for example PECVD and RIE, are detailed at the first mention, and are not changed throughout subsequent use.
- Residual resists, after etching steps, were cleaned using acetone or NMP solvent (N-Methyl-pyrrolidone), then rinsed with deionised (DI) water and IPA before drying with a N$_2$ gun.

3.2.1 Fabrication of simple doubly-clamped buckled beams

Released and freestanding beams are the most basic MEMS structures, and are the basis for a range of devices, including resonators, sensors and switches. Here, the fabrication of doubly-clamped beams is presented.
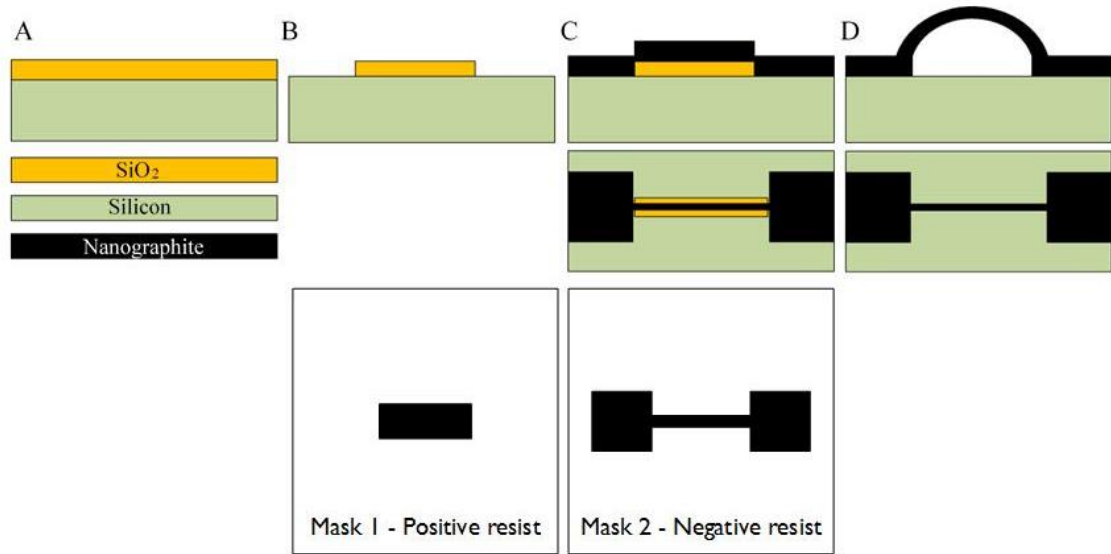
Figure 3.2. Process flow showing the main fabrication steps for doubly-clamped beams.

The first step for fabrication was to pattern a layer of SiO_2 (Figure 3.2 (A-B)), for use as a sacrificial spacer, which defines the released beam length. SiO_2 was deposited to a thickness of 200 nm using PECVD (Oxford instruments System 100LS) with the parameters set in Table 3.2. PECVD was considered the most suitable method for SiO_2 film deposition, since this is a relatively quick process for low numbers of wafers. The quality of film regarding density and etch resistance is lower than thermally grown SiO_2 [117]; however in this case this was a sought-after property. This was because it was preferential to reduce the exposure time of the device during etching, as, for example, the nickel electrode (in subsequent devices) is increasingly roughened by the HF over time.

Temperature (°C)	350
RF Power (W)	20
Pressure (mTorr)	1000
SiH_4 flow-rate (sccm)	4.2
N_2 flow-rate (sccm)	80
N_2O flow-rate (sccm)	350
Upper chamber heater (°C)	90

Table 3.2. Summary of the deposition conditions for PECVD SiO_2

After deposition the wafer was spin coated using S1813 positive resist at 5000 RPM and then baked at 115 °C. After cooling to room temperature the wafer was exposed using a UV EVG 620 T mask aligner using Mask 1 (Figure 3.2). The exposed resist was developed using MF319 developer for 40 seconds, then rinsed in DI water and dried using an N_2 gun. The resist thickness was 1.3 µm. After confirmation of the resist development, the SiO_2 was etched using reactive ion etching (RIE), with the recipe in Table 3.3.

Temperature (°C)	20
RF Power (W)	200
Pressure (mTorr)	30
CHF_3 flow-rate (sccm)	18
Ar flow rate (sccm)	32

Table 3.3. Summary of RIE conditions used to etch SiO_2.

The wafer was now an array of patterned SiO_2 sacrificial anchors, which are used to define the length of the released beams of 65 to 140 µm. Nanographite was deposited onto the patterned wafer to a thickness of 400 nm (Figure 3.2 (C)). The thickness of the film must be larger than the thickness of the anchor to ensure a continuous film, since the PECVD process was characterised to be largely directional and non-conformal; this is demonstrated in the Figure 3.3.
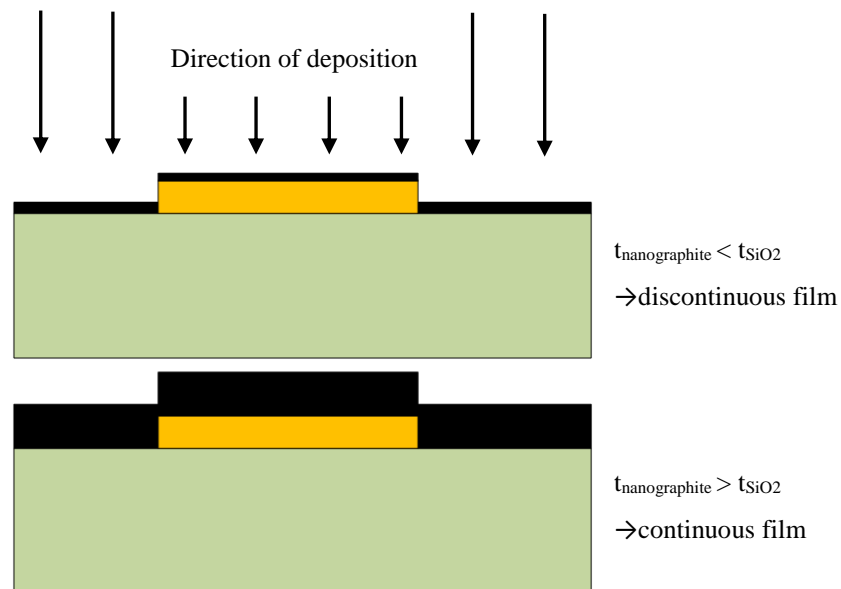
Figure 3.3. Diagram showing the thickness requirement for obtaining a continuous film when depositing nanographite over pre-patterned substrates using non-conformal PECVD.

The wafer was then spun with AZ2070 negative resist at 6000 RPM, yielding 5 µm thick layer and exposed after alignment to Mask 2 (Figure 3.2). This mask defines beams of 10 µm width, with large

anchors, as shown in Figure 3.4. The resist is baked at 110 °C and exposed in the mask aligner using an I-line filter in place. After exposure the wafer was then further baked at 110 °C, before development in AZ726 MIF. The nanographite was etched using RIE (recipe in Table 3.4). The wafer was then spin coated with S1813 resist before it was diced into individual chips. The resist is used to protect the surface from dust produced during the dicing process. Each chip was then cleaned in IPA and deionised water to remove the protective resist layer.
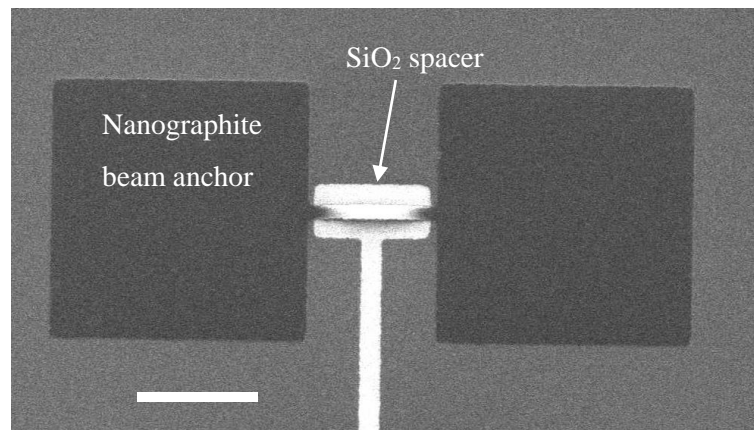
Figure 3.4. SEM image of a nanographite doubly-clamped beam, with both lithographic layers visible. Scale bar is 100 µm.

Temperature (°C)	20
Pressure (mTorr)	100
RF Power (W)	100
O_2 flow rate (sccm)	50

Table 3.4. Summary of the RIE etching conditions used to etch nanographite.

For the final step, the beam is released from the substrate (Figure 3.2 (D)). This is achieved using hydrofluoric acid vapour, using an Idonus HF etching system with the chip heated to 40 °C. This isotropically etches the SiO_2 without etching the nanographite. HF in the vapour phase avoids stiction between the beam and substrate which can be caused by surface tension when using liquid etchants. The built in stress of the film causes upward buckling of the released beam structure. Figure 3.5 shows a released device.
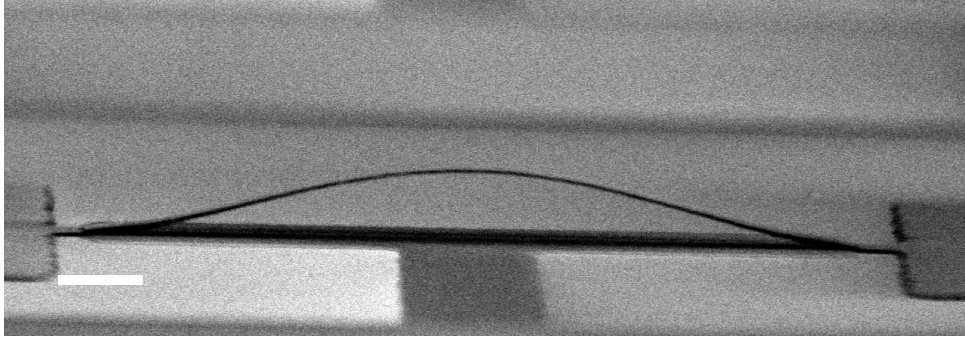
Figure 3.5. SEM image showing a high angle view of a released, buckled doubly-clamped nanographite beam. Scale bar is 10 µm.

3.2.2 Fabrication of MEMS nanographite resonator device

The fabrication of MEMS resonator devices builds upon the steps described for the doubly-clamped beams, with the same mask design used for the beam structures. For these resonators, both doubly-clamped and cantilever beams were fabricated.
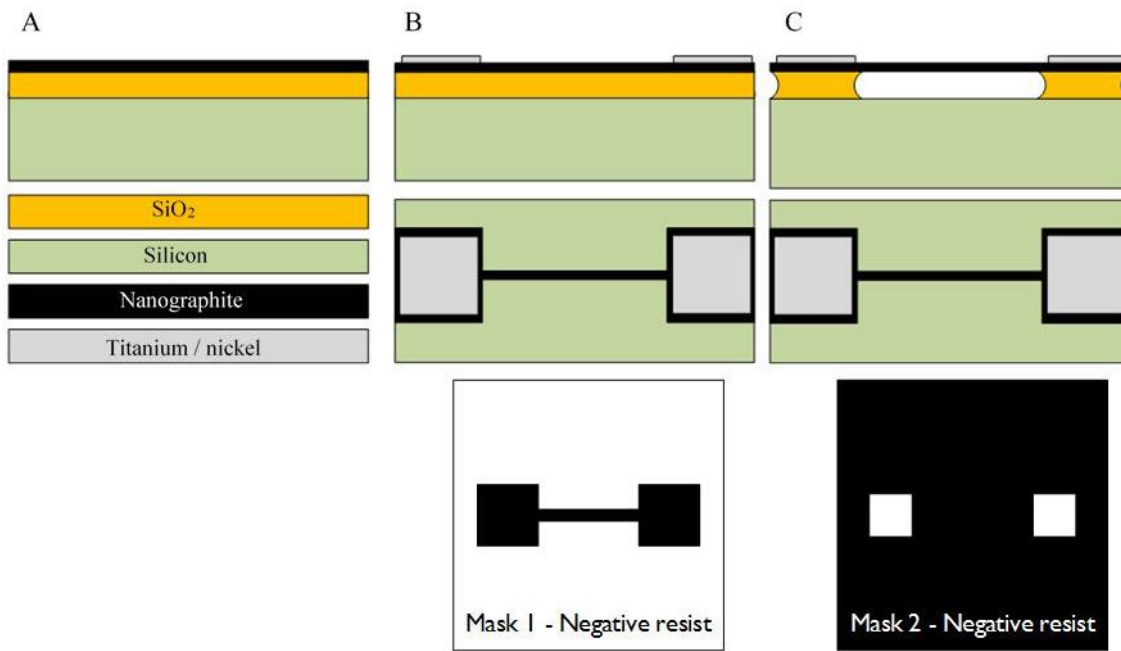
Figure 3.6. Process flow showing the main fabrication steps for resonators.

Firstly, 200 nm SiO_2 is deposited using PECVD, and then 350 nm nanographite is deposited directly onto the unprocessed SiO_2 layer (Figure 3.6 (A)). The wafer is then coated in AZ2070 resist and exposed using Mask 1 (Figure 3.6), which defines the beam outline with large square anchors. Both SiO_2 and nanographite layers are then fully etched using RIE.

The wafer is then coated in AZ2070 resist and Mask 2 (Figure 3.6) is exposed. This defines openings over the beam anchors for the electrodes. After development of the resist, titanium/nickel electrodes of 5/50 nm thickness are deposited over the wafer using e-beam evaporation (Leybold LAB700). The evaporation of both metals is performed in the same step, without venting the system to atmosphere; this avoids the formation of titanium oxide between the two metals. The entire wafer is coated in this step, and the metal which lies over the remaining resist is then 'lifted off' by dissolving the resist using NMP overnight. This leaves the beam with metalised anchors (Figure 3.6 (B)).

The final step is to release the beam structures from the substrate using HF vapour (Figure 3.6 (C)). A relatively large undercut of the beam anchors, caused by over-etching at this step, enables buckle-free structures to be released. This is enabled by deformation of the beam anchors, and the beam moves from a buckled state to a flat, tensile state. Part of the evolution in profile for the released beam is shown in Figure 3.7, with the beam initially being buckled before being effectively 'pulled' into a state of tensile stress as the undercut length increases. These devices were etched using a home-built HF vapour setup; the schematic is shown in Figure 3.8. In this setup, a lamp is placed above the chip to provide heating, and the chip is placed over an opening in a Teflon sheet and placed over a beaker filled with 25 % HF.
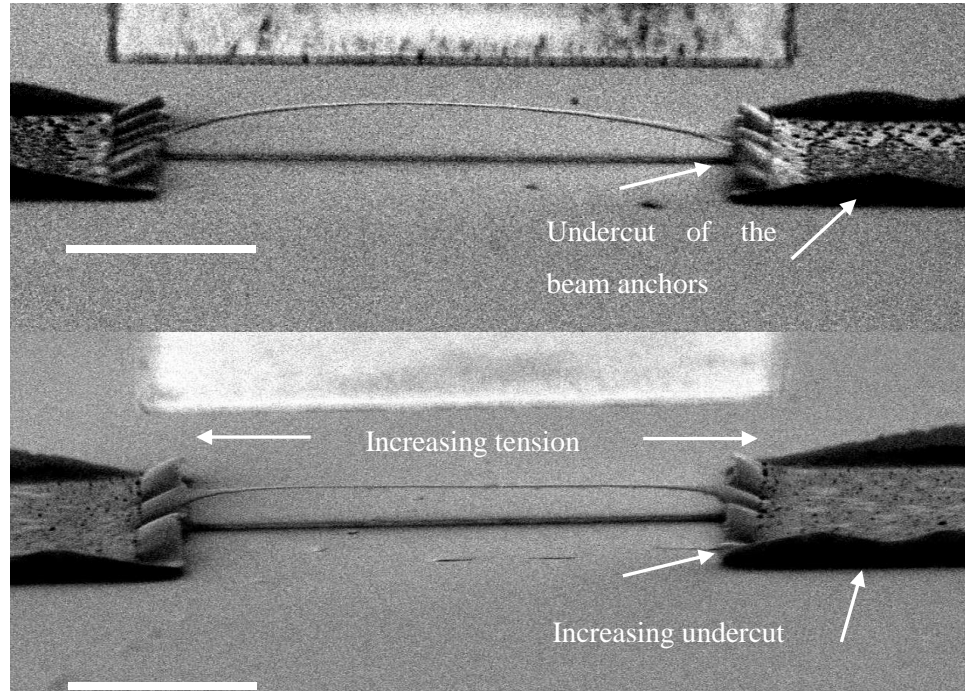
Figure 3.7. Two SEM images showing the evolution from buckled beam to straight beam with increasing period of etch and increase in undercut. Scale bars are 50 µm.
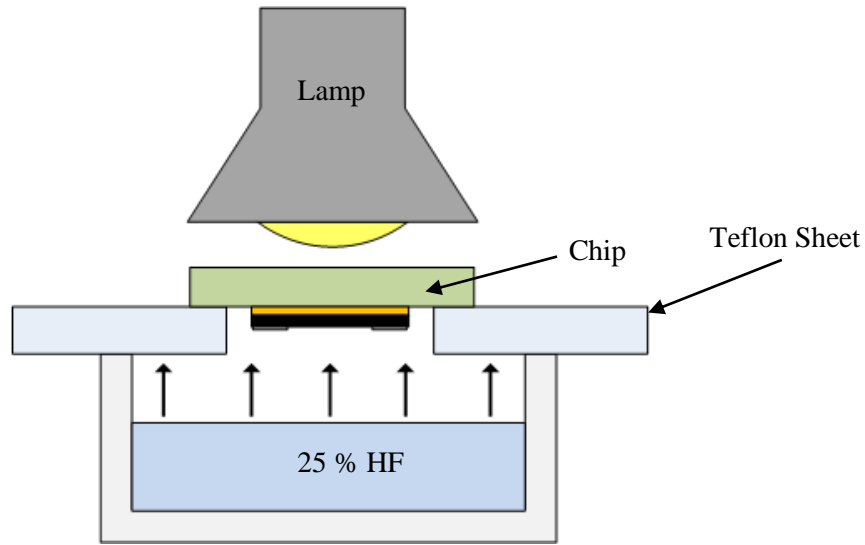
Figure 3.8. Schematic of the homebuilt HF vapour etching setup.

The etch rate of SiO_2 in HF vapour was measured at around 2µm per hour. Samples were periodically checked for the lateral etch depth under optical and scanning electron microscopy, since there was a degree of variability between chips when etching using the home-built setup. A typical etch release using this system was around 8 to 12 hours, compared with 10 to 15 minutes using the Idonus system. Completed released devices are shown in Figure 3.9 (A-B).
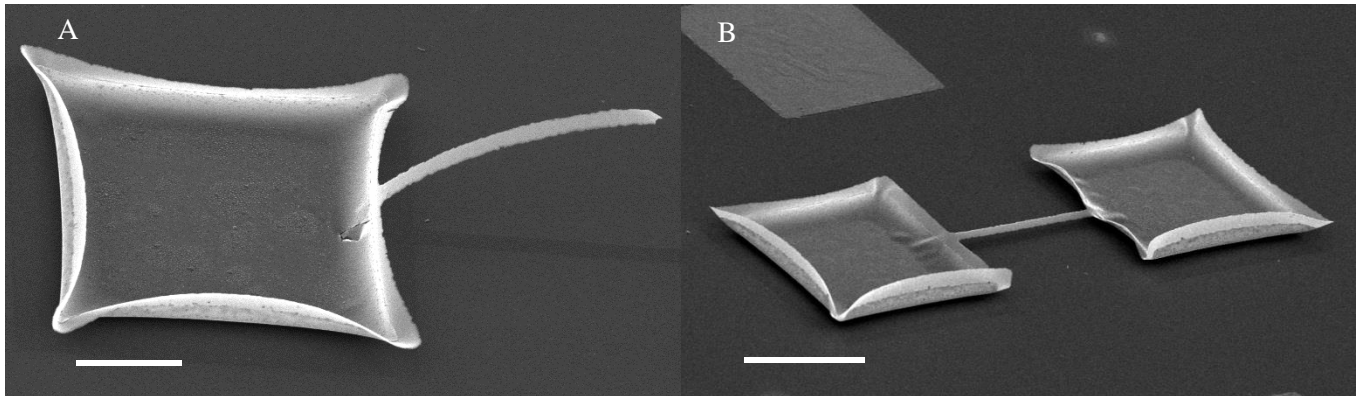
Figure 3.9. (A) SEM image of released nanographite cantilever device, 150 µm long. (B) SEM image Released nanographite doubly-clamped resonator, 100 µm long. Scale bars are (A) 50 and (B) 100 µm.

3.2.3 Fabrication of membranes

3.2.3.1 Membranes using silicon substrates

Firstly, a 400 nm SiO_2 layer was deposited by PECVD onto the wafer front-side. This is used as an etch-stop for a later step. A 350 nm layer of nanographite was then deposited onto the front-side followed by deposition of 1 µm thick layers of SiO_2 onto the front and backsides of the wafer using PECVD. This is to act as a masking material against the deep wet anisotropic silicon etchant, TMAH, and was found to have sufficient selectivity of etch rate.
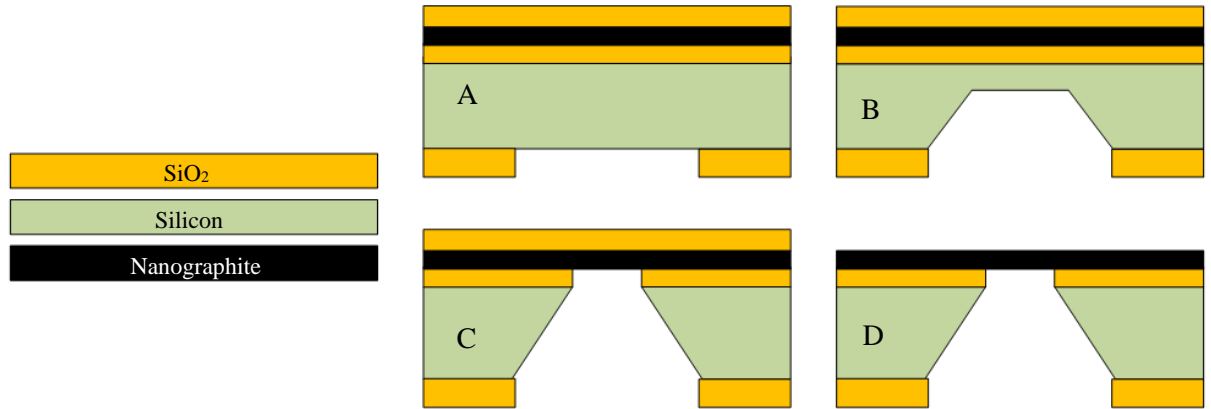
Figure 3.10. Process flow showing the main fabrication steps for membranes using a silicon substrate.

Square window openings were defined on the wafer backside through photolithography, using positive S1813 resist, with the SiO_2 layer etched using RIE (Figure 3.10 (A-B)). The size of the windows was designed to obtain membranes of front-side dimension 200 to 300 µm square. Earlier trial results using PECVD Si_3N_4 masking material and KOH as the silicon wet etchant provided variable results, with delamination of the mask occurring in areas over the wafer and with pinholes in wide regions over the wafer. This was never observed using the SiO_2 mask with TMAH etchant. The deep silicon etching step is required to release the membrane structures from the backside. TMAH gives an anisotropic etch profile creating pyramid-shaped pits bound by the slow-etching {111} planes of Silicon, as shown in Figure 3.11. 25% TMAH diluted in water was used at 70°C which etched the silicon at around 25 µm per hour. The wafer was removed from the etchant when there was around 100 µm remaining of the silicon wafer (Figure 3.10 (B)). This was to ensure sufficient thickness of silicon remained to retain stability of the wafer for dicing into individual chips, which was the next step.

Inductively coupled plasma (ICP) and RIE etching was then used to fully release the membranes from the wafer backside, with the ICP recipe summarised in Table 3.5. This method of wet-etching the wafer bulk and then fully releasing the devices using a dry ICP etch was developed by my colleague David Grech in the Southampton Nano Research group [118]. This technique removes the

risk of failure of devices from surface tension, which was found to be an issue on some devices fully released using TMAH.

Temperature (°C)	10
Pressure (mTorr)	20
SF_6 flow rate (sccm)	100
Ar flow rate (sccm)	25
RF power (W)	20
ICP power (W)	1500

Table 3.5. Summary of ICP conditions used to etch silicon.
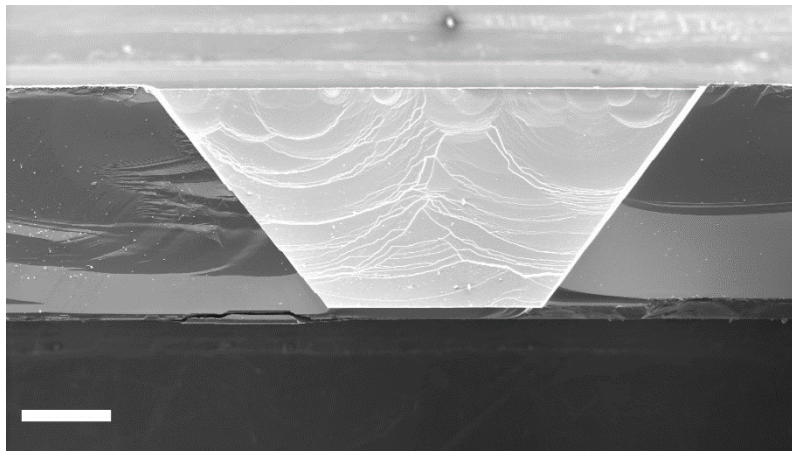
Figure 3.11. SEM of cross section of TMAH and ICP-etched pit to observe sidewall profile. Scale bar is 250 µm.

The individual chips were placed onto a plain glass carrier wafer for ICP etching through the remaining silicon of approximately 100 µm thickness. RIE etching was then used for the SiO_2 layer (Figure 3.10 (C)). Etching is completed in successive steps, and visual observation of 'breakthrough' of successive layers (firstly from silicon to the SiO_2 layer, and subsequently to the nanographite layer) can be made using optical microscopy from the backside as shown in Figure 3.12 (A-C). After breakthrough to the nanographite layer, there was typically a period of over-etching of around 30 seconds to ensure the SiO_2 layer is fuly etched, thus the nanographite is exposed to this RIE etching step. The selectivity of etch rate between nanographite and SiO_2 under this etch is high (under 3 nm compared with around 30 nm for SiO_2. Both cases were measured using ellipsometry) and the etching of the nanographite layer is small. Finally, the front-side SiO_2 layer is removed using RIE (Figure 3.10 (D)). A microscope image of a fully released membrane is shown in Figure 3.13; this device has a thickness of 275 nm and is 193 µm square in lateral dimensions.
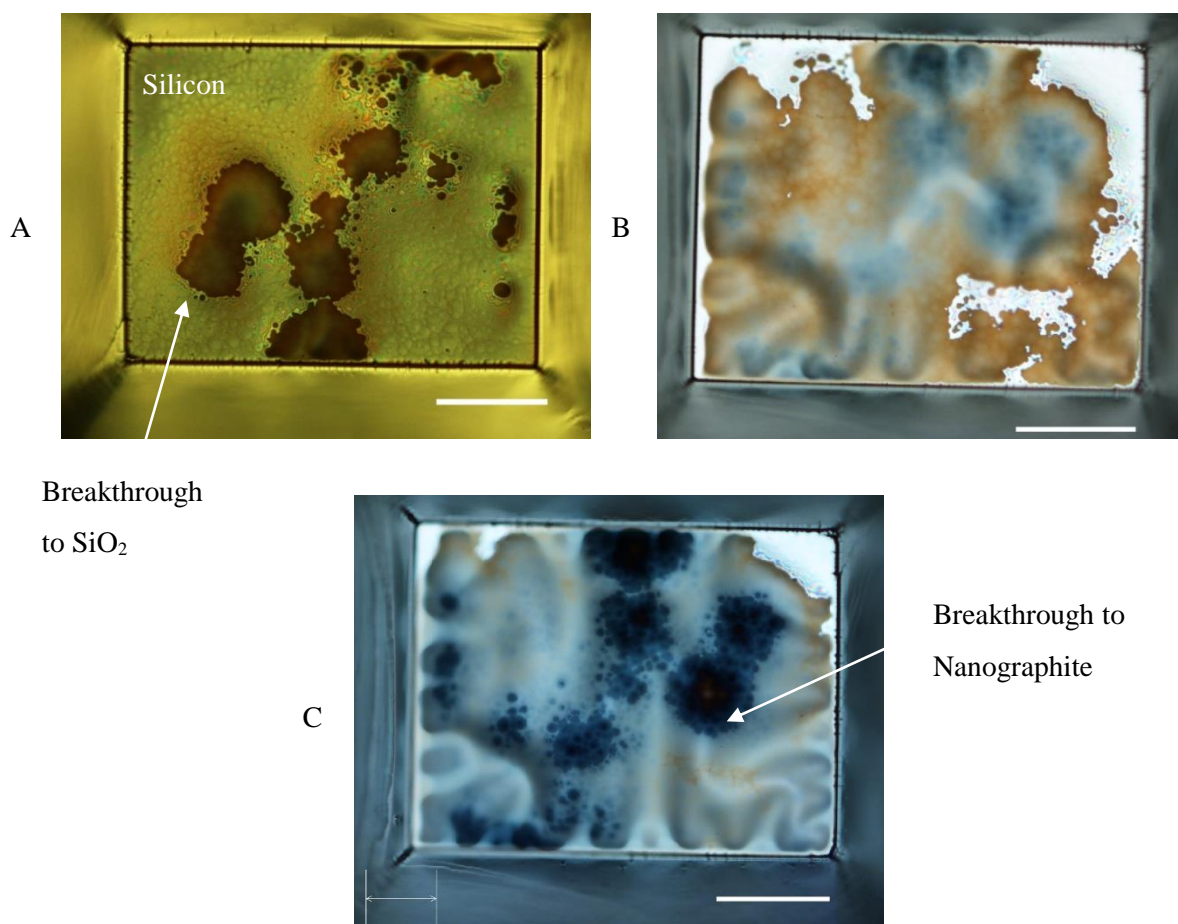
Figure 3.12. Optical microscope images showing etching of the membrane: (A-B) Full etching of the silicon bulk wafer using ICP. (C) Etching of SiO_2 using RIE reaching the nanographite layer. Scale bars are 50 µm.
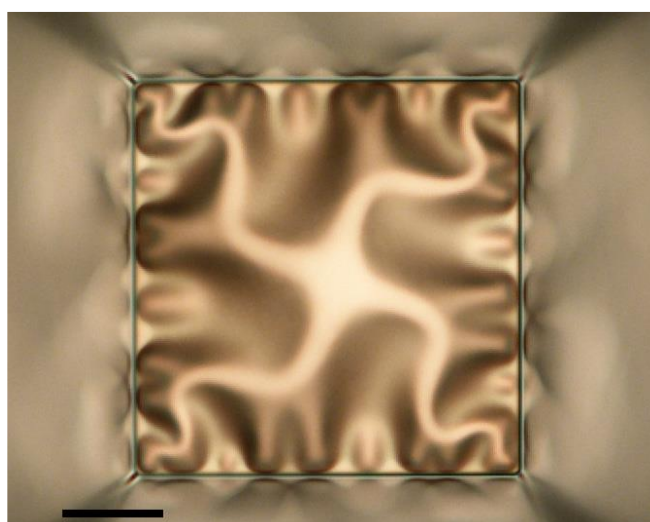
Figure 3.13. Optical microscope image of 193 µm nanographite square membrane. View taken from backside. Scale bar is 50 µm.

For testing the gas permeation of nanographite membranes, amorphous fused quartz substrates were used, for two main reasons:

- The lower thermal coefficient of expansion of fused quartz reduces the thermal stress in the nanographite layer compared with using a silicon substrate. Lower stress membranes are more stable under a differential pressure.

- The use of a fused quartz substrate enables fabrication of circular membranes due to the amorphous crystal structure, thus an isotropic etchant hydrofluoric acid (HF) can be used. Circular membranes have significantly lower stress concentration than square membranes, which focus stress at the corners. Lower stress concentration is important to enable relatively higher pressure gradients across the membrane during permeation. Larger area membranes can be fabricated at this lower stress state, with a higher absolute gas flux.

To fabricate the membranes, nanographite is deposited to a thickness of 350 nm onto one side of a doubly-polished 4-inch fused quartz wafer. The basic process is to produce windows in the backside mask, and isotropically etch the fused quartz through to the nanographite layer. The process flow for fabricating these membranes is based on work by Jin *et. al* [119].
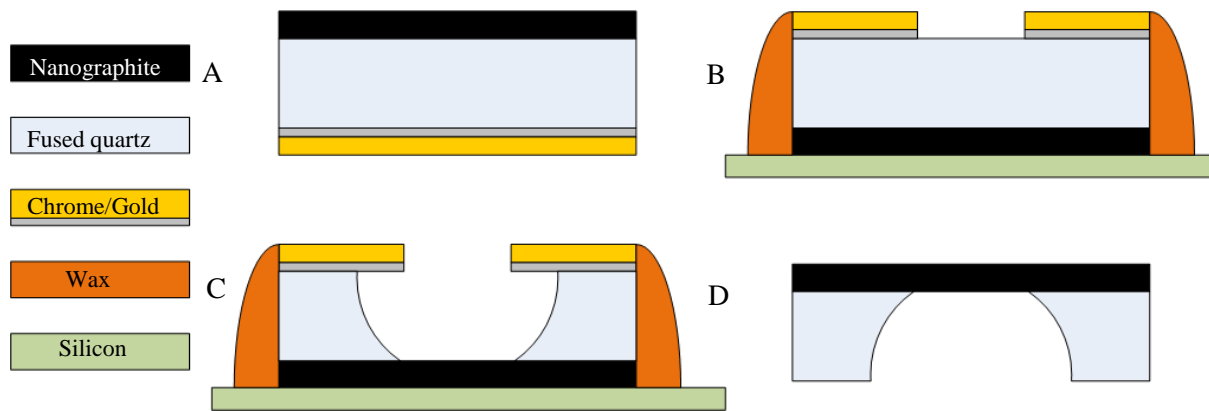
Figure 3.14. Process flow showing the main fabrication steps for membranes using a fused quartz substrate.

The backside mask used to pattern the openings to release the membranes is of 10 nm chrome, which acts as an adhesion layer to the fused quartz, followed by 300 nm gold with both layers deposited by thermal evaporation (Figure 3.14 (A)). The gold layer is then coated with AZ4330 positive resist. This acts as a mask to firstly pattern the gold/chrome layers, but also greatly aids in reducing the density of pinholes during the deep HF etching step by acting as a further protective layer. The resist is spun at 1000 RPM and then baked at 95 °C, yielding a layer of 7 µm. The resist is then exposed with a circular pattern sized between 25 to 100 µm. The resist is developed for 60 seconds using AZ

developer, and then post-baked for 20 minutes at 120 °C in an oven. This post-baking step is used to make the resist layer more hydrophobic thereby reducing the HF diffusion through to the gold layer [119]. The gold and chrome layers are etched using wet etchants, with a DI water rinse in between (Aldrich gold etchant and Microchrome Technology, CEP-200 chrome etchant). The metal layers are confirmed to be fully etched by microscope inspection. The wafer is then diced into individual chips after this stage.

To protect the sides and front (nanographite side) of each chip, wax is used to adhere the chip to a carrier, an offcut piece of blank silicon wafer. The wax is placed onto the carrier and heated to 100 °C using a hotplate. At this temperature the wax is in a viscous, liquid state, and the patterned chip is then pushed into the wax, face down, ensuring the sides are fully covered (Figure 3.14 (B)).

49% HF acid is used to etch through the bulk of the fused quartz wafer, until the nanographite layer is reached, which is clearly visible during microscopy inspection. The HF etch step takes roughly 16 hours to reach the nanographite (Figure 3.14 (C)). Finally, the chip and carrier is heated to 100 °C on a hotplate, melting the wax and releasing the chip from the carrier. The released chip is placed in acetone overnight to remove the residual wax (Figure 3.14 (D)). A completed membrane is shown in Figure 3.15, and is slightly wrinkled due to compressive stress in the film.
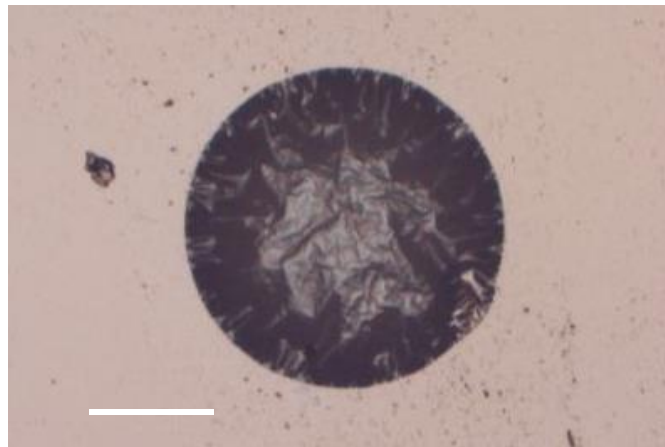
Figure 3.15. Optical microscope image of a nanographite membrane fabricated on a fused quartz substrate. Scale bar is 100 µm.

3.3 Measurement of MEMS resonators

The resonator devices I have fabricated are electrically actuated and detected optically using laser Doppler vibrometry (LDV). Here, the methods for actuation and measurement of the nanographite resonator structures are detailed, with both doubly-clamped beams and cantilever resonators using the same systems.

3.3.1 Electrostatic actuation

The released devices were electrostatically actuated by applying voltage $V = V_{DC} + V_{AC} \cdot cos\ (\omega t)$ between the beam and the grounded silicon substrate. Here V_{DC} is the DC bias and V_{AC} is the amplitude of the AC voltage bias, applied at radial frequency ω, (equal to $2\pi \times f$ where f is the frequency in Hz). This generates an electrostatic force F_e applied on the beam. F_e may be calculated as in Equation 3.1 [26]. As the forcing frequency f becomes close to the natural frequency of vibration of the mechanical beam f_0, the natural mode shape of the beam is excited and the vibration amplitude becomes large, this is known as resonance.

$$F_e \approx -\frac{1}{2}\frac{\partial C}{\partial r}\left(V_{DC}^2 + 2V_{DC}V_{ac}\cos\left(\omega t\right)\right) \qquad (3.1)$$

where C is the effective capacitance between the resonator area and the underlying substrate at a separation distance r. During testing, a DC bias of 2 V and AC voltage of 0.2 V was used unless otherwise stated.

The voltage output is controlled by the LDV software, linked to a voltage function generator (HP 33120A) and the device electrically contacted with probe needles (Cascade MH2-B positioners) for measurement at ambient pressure. One sample was wire-bonded using gold wire for actuation and measurement under vacuum. A custom built vacuum chamber with a window for the LDV was used, with the base pressure measured a by manometer gauge (MKS Baratron).

3.3.2 Vibration measurements

A commercial LDV system (Polytec 300-F) was used to measure the vibrational velocity of the beam during actuation. The software may be used to sweep the frequency f of the AC signal V_{AC} between 0 and 1 MHz and measures the corresponding velocity of vibration of the beam at that frequency. A schematic of the setup is shown in Figure 3.16, and is configured to measure out-of-plane motion of the microfabricated test structures.

The LDV uses a polarised helium-neon laser, the spot size of which is around 10 μm diameter, and is focused on the centre of the beam for doubly-clamped devices, and at the beam end for cantilevers. To measure the velocity of the structure, the laser is split into a 'reference' and 'object' path. The motion of the structure adds a Doppler shift onto the object path, $f_{Doppler} = 2\times v\left(t\right) \times cos\left(\eta\right)/\lambda$ where $v\ (t)$ is the velocity of the target as a function of time t, η is the angle between the laser beam and the velocity vector of the target, and λ is the wavelength of the light (633nm) [120].
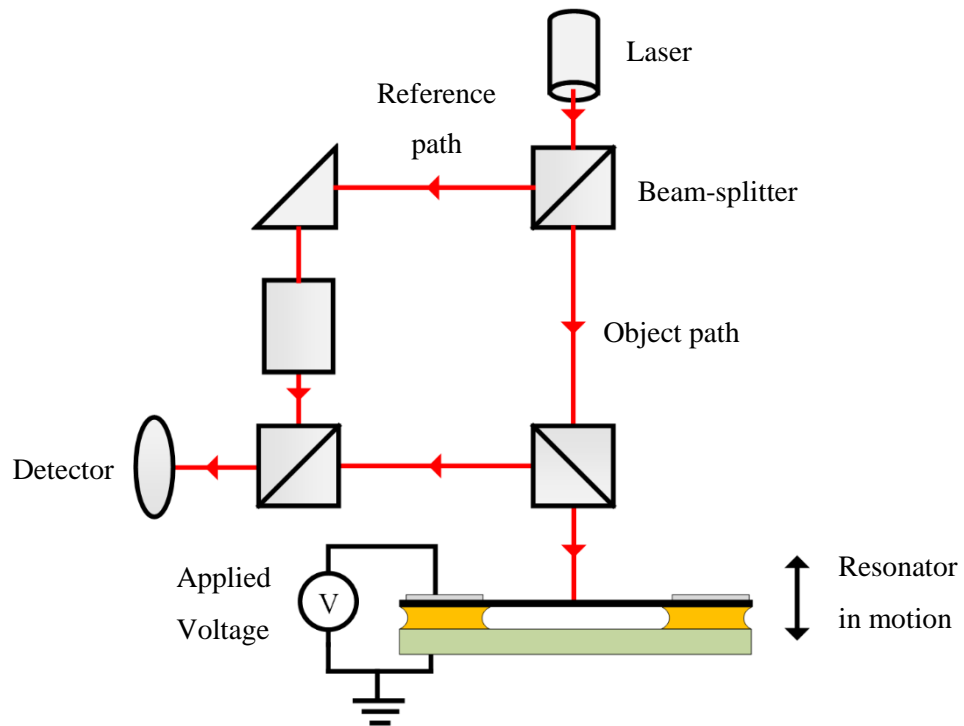
Figure 3.16. Schematic of LDV head measuring a MEMS resonator.

3.4.3 Vibration analysis

A schematic of a resonance spectrum is shown in Figure 3.17. To determine the vibration frequency and Q, a Lorentzian curve was fitted to the data. The natural frequency of vibration is shown as f_o and the full width half maximum is FWHM and the peak amplitude is A_0. The FWHM is defined for a power spectrum as $A_0^2 / 2$. Thus in the amplitude spectrum the FHWM corresponds to $A_0 / \sqrt{2}$.

3.4 Membrane permeation testing rig

The fabricated membranes were used for gas permeation testing with the permeance to various gases characterised. The experimental setup and technique is summarised here.

3.4.1 Criteria for testing apparatus

For permeation testing of the nanographite membranes, a system which fulfilled the following criteria was required:

- Repeatable and accurate measurement of gas flow, sensitive to many different types of gas.
- Measurement of membranes of diameter ~ 1 mm.
- Enable permeation testing at elevated temperatures.
- Non-destructive to the membrane with repeat measurements possible.

The flow of gases through the membrane is calculated by measuring the downstream pressure of gas using a residual gas analyser (RGA) type mass spectrometer. Figures 3.17 and 3.18 show the system constructed and is similar to permeation testing rigs in other research [121,122].

Pure gas was used from 10 L cylinders (Air Liquide AlphaGaz). Prior to any experiment to fill the HV chamber with gas, the gas line was fully evacuated, with the cylinder shut off. After evacuation for around 5 minutes, the gas line was filled to a pressure of around 1 Bar. A needle valve was used to fill the HV side in a controllable manner. This ensured that the gas was free of residual air when the system was filled.

The rig comprises two effective chambers; a larger chamber at ultrahigh vacuum (UHV) in which sensitive gas partial pressure measurements are made using the RGA, and a smaller chamber evacuated to high vacuum (HV) conditions, which during testing is filled with the analyte gas to a pressure in the range 30 to 100 Torr. The two chambers are separated by the membrane, yielding a concentration gradient across the membrane. Thus if the membrane is permeable, gas will flow into the UHV chamber and be measured under suitable conditions by the RGA.

The UHV chamber was evacuated using a Varian V-551 turbomolecular pump rated to 550 L sec^{-1}. This chamber comprises stainless steel components with copper gasket sealing 'Conflat' flanges (rated leak-tight to $\sim 1 \times 10^{-13}$ Torr). The system was thoroughly baked overnight using external heater tapes at $\sim 150°C$ to remove water vapour and other contaminants from the system walls. After baking, a UHV base pressure of around 1×10^{-10} Torr was achieved.

The HV side comprises a series of crosses and valves sealed using Viton O-ring seals. This was evacuated using a turbo pump (BOC Edwards EXT) rated to 50 L sec^{-1}.
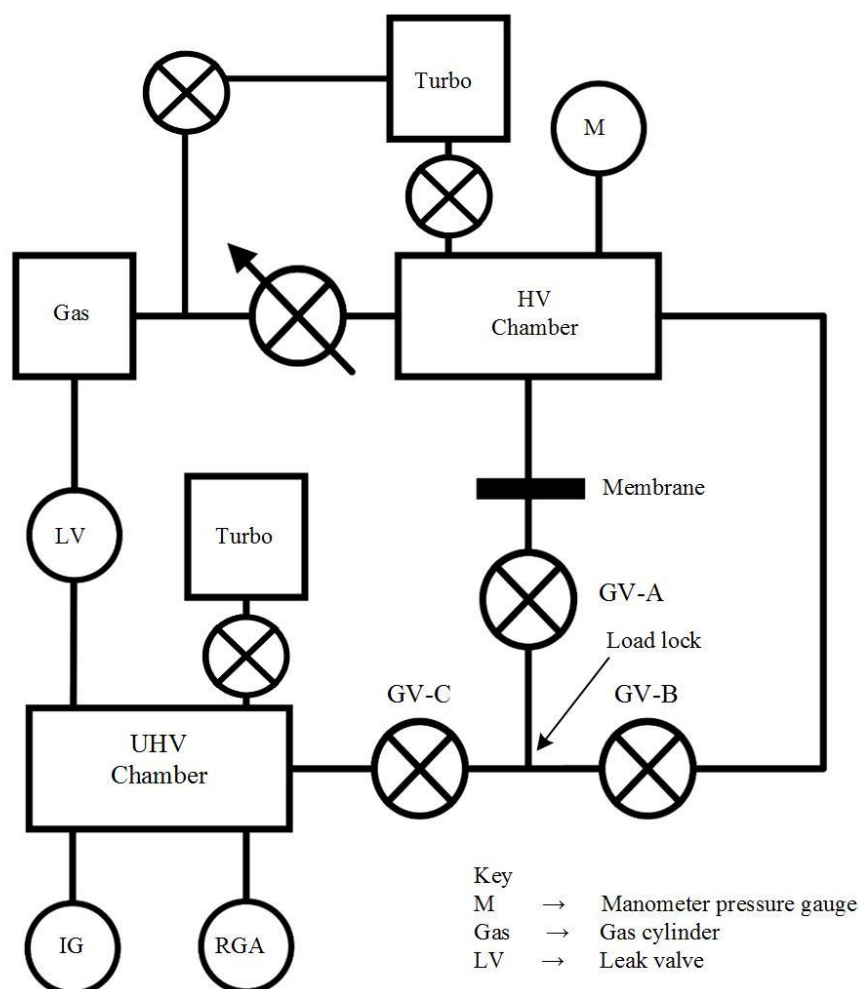
Figure 3.17. Schematic of the UHV gas permeation rig.
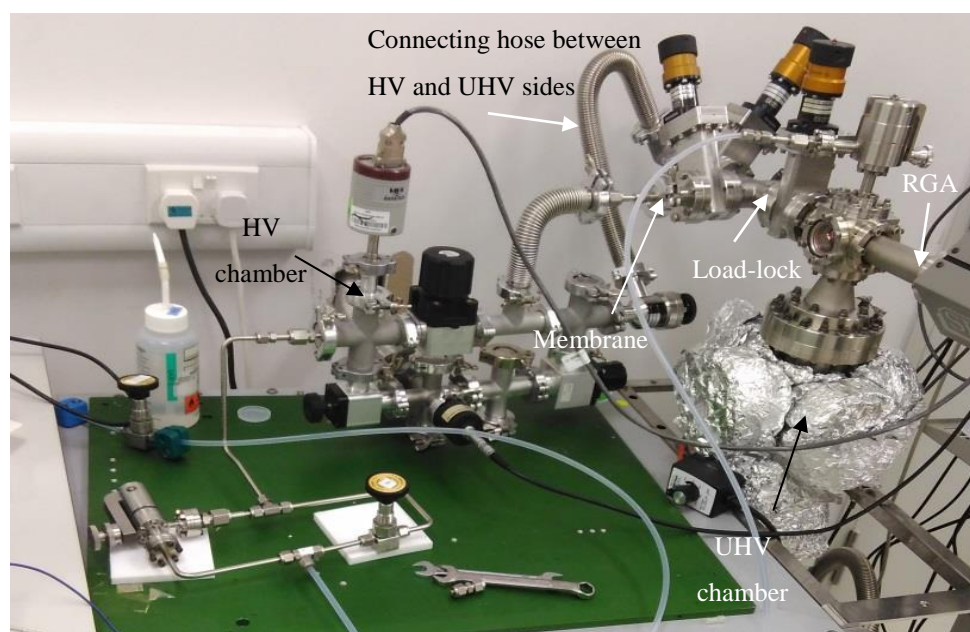
Figure 3.18. Photograph of the gas permeation rig

To install the membrane, UHV rated 2-part epoxy glue (Allectra 330s-GLUE1-M3) was used to adhere the membrane over a stainless steel gasket. The gasket was then adhered over the orifice of a Swagelok-CF adapter as shown in Figure 3.19. Leak-tightness was confirmed by adhering a 'blank' chip, which was a fused quartz chip without membrane, with no measurable gas flow observed.
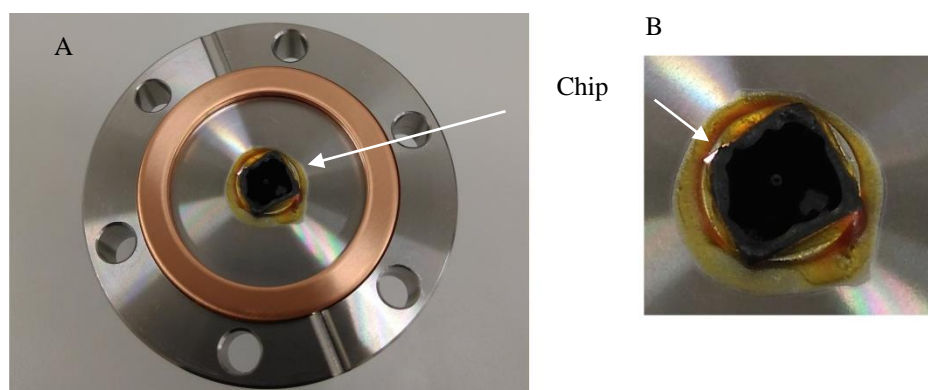
Figure 3.19 (A) Photograph of a membrane chip adhered over an orifice of a UHV fitting. (B) Close-up image of adhered chip, showing UHV glue providing a seal around the gasket edge.

The membrane is too fragile to withstand a differential pressure of 1 atmosphere, therefore the chambers surrounding both sides of the membrane had to be evacuated simultaneously. This was enabled by having the HV and UHV chambers linked with a separate hose. Thus, referring to Figure 3.17, for installing a membrane, gate valve (GV) B and A were open, GV C was shut (this ensured the main UHV chamber was kept under UHV) and the top load-lock section and HV chamber were vented to atmosphere (and conversely, evacuated) equally on both sides of the membrane.

3.4.2 RGA partial pressure operation and calibration

The RGA is a quadrupole mass spectrometer, measuring the ion current at discreet mass/charge values, which can be used to calculate the pressure of each individual gas (partial pressure) present in a system.

The basic principle of operation is as follows, this summary is a precis from the RGA manufacturer [123]. A filament, as shown in Figure 3.20 is held at negative potential and is resistively heated to incandescence; this becomes the source of electrons which is used to ionise gas molecules in the system. Electrons from the heated filament are accelerated toward a positive charged anode grid. An electron may ionise a gas molecule present between the filament and anode grid and molecules are ionised into fragments. The ions formed within the grid are attracted to the negative potential of the focus plate, which draws ions and focuses them into the filter section. Within the filter, the ions are separated based on their mass-to-charge ratio. The ion current at each mass-to-charge ratio is a

function of the abundance of the associated molecule in the system, which is thus used to calculate the partial pressure.
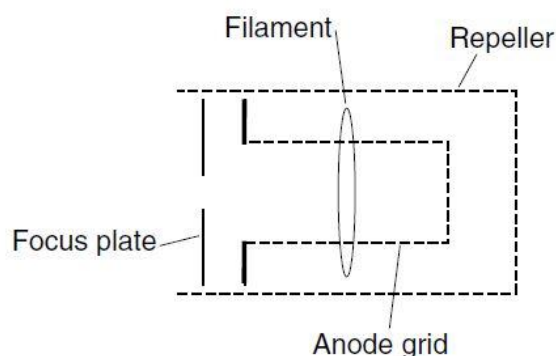
Figure 3.20. Schematic of the RGA ioniser. Image from [123].

I used a calibration system as recommended by the manufacturer to calculate the partial pressure. Using a leak valve, the analyte gas is introduced into the system, raising the overall pressure of the system from, for example, a base pressure of $\sim 3\times10^{-10}$ to $\sim4\times10^{-6}$ Torr. In this condition, it is clear that the pressure of the system is dominated by the partial pressure of the analyte. The overall pressure is measured by an ionisation gauge (IG). Thus a graph plotting the RGA ion current for the analyte gas vs. the IG pressure shows the conversion factor k between the uncalibrated RGA gauge and the known IG pressure. These plots are shown in Appendix 3.

It is noted that the IG is not a calibrated instrument. Without access to a suitable calibrated total pressure gauge, such as a spinning rotor gauge, this error is considered unavoidable in the scope of this work.

3.4.3 Permeation measurement using closed volume method

Two separate methods to measure the membrane permeation were used, and a comparison of the results is made in Chapter 6. The first detailed is the 'closed-volume' method. In this, the UHV chamber is shut off from the evacuating turbo-pump, and the permeate pressure is allowed to build up without being removed by the pump. The pressure rise over time into the known chamber volume is used to calculate the molar flux and permeance through the membrane. The volume of the chamber was calculated from the volume of 3D computer-aided-design models of each separate component of the system.

The membrane leak rate Q_m (Pa m^3 sec^{-1}) can be calculated by measuring the change in partial pressure of the analyte gas with time, as described in Equation 3.2:

$$Q_m = \left[\left(\Delta p_{AVG} / \Delta t\right) - \left(\Delta p_0 / \Delta t\right)\right] \cdot v \qquad (3.2)$$

where Δp_{AVG} is the measured change in pressure over a time period Δt, Δp_0 is the measured change in background pressure arising from gases emanating from the vacuum chamber internal surfaces and v is the measured volume of the chamber [124]. From the leak rate, the molar flux, J, (moles sec^{-1} m^{-2}) may be calculated by:

$$J = \frac{Q_m}{RTa} \tag{3.3}$$

Where a is the geometric surface area of the membrane, R is the molar gas constant and T is the absolute temperature. The permeance, B, mol m^{-2} sec^{-1} Pa^{-1} is defined as [125]:

$$B = \frac{J}{\Delta p_{ups}} \tag{3.4}$$

Where p_{UPS} is the upstream pressure of the gas, in the HV chamber.

3.4.4 Permeation measurement using the vacuum method

A second measurement scheme has been employed to compare the permeation values of the membrane as measured by two separate methods. Here, the molar flux through the membrane is measured during constant pumping of the UHV chamber. By definition, the total number of molecules flowing into a system per second N_t, in moles, is the flux J multiplied by area (m^{-2})

$$N_t = J \cdot a \tag{3.5}$$

Experimentally the ideal gas equation is used to calculate the molar gas flow as [121]:

$$N_t = \frac{p \cdot EPS}{RT} \tag{3.6}$$

Where P is the pressure and EPS is the effective pumping speed, which is the volume removed per unit time by the system pump. Combining Equations 3.5 and 3.6 yields the molar flux as:

$$J = \frac{p \cdot EPS}{RTa} \tag{3.7}$$

From which the permeance can be calculated as before:

$$B = \frac{J}{\Delta P_{ups}} \tag{3.8}$$

In Equation 3.7, EPS must be measured. The quoted value for the turbo pump (550 L sec^{-1}) represents an ideal case which cannot be readily achieved in a real-life experiment. Furthermore, to increase the pressure of the analyte gas and thereby increase the sensitivity of the method, the turbo pump can be throttled (the pumping speed effectively reduced) by partially closing the gate valve above the turbo pump. In order to calculate the EPS, including in the case of throttling the gate valve, I used a leak valve to introduce a flow of gas into the UHV system. The leak rate Q_{leak} is measured using the closed volume method, as in Equation 3.2, with the gate valve closed.

The system is then pumped with the gate valve open (or throttled) and with the leak valve kept open at the same level. The partial pressure of the analyte gas p_{leak} is measured and hence the EPS pumping speed can be calculated as:

$$EPS = Q_{leak} \, / \, p_{leak}$$ (3.9)

3.4.5 Measuring gases in the presence of residual gas peaks

UHV systems typically have measureable peaks due to the following residual gases in the system. Large residual gas peaks typically arise from the following:

- Water. This arises from the humidity in the air. The quantity of water in the system can be reduced by 'baking' the chamber walls. Water has a main RGA peak at 18 AMU (H_2O – 74.4 %), with other peaks at 17 (HO - 17.1 %), 16 (O - 8.2 %), 20 (H2+O - 0.2 %) and 19 (H+O - 0.07 %).

- Carbon dioxide, carbon monoxide and hydrogen are all present due to diffusion of gases from the chamber walls which are made from stainless steel. These elements diffuse from the region of high concentration and high diffusivity in the grain boundaries of the steel [126]. For example, carbon dioxide has peaks at 44 (CO_2 - 78.4 %), 28 (CO - 8.6 %), 16 (O - 7.1 %), 12 (C - 4.7 %), 45 ($C+O_2$ - 0.8%) 46 (CO_2++ - 0.4%).

An example of a typical residual gas background of a mass spectrometry graph is shown in Figure 3.21. The presence of these residual elements is important because they can effectively 'mask' the flow of the analyte gas when they share a common mass to charge ratio. For example, Nitrogen is ionised into N_2 (28 AMU - 92.6%), N (14 AMU - 6.7%) and N_2+ (29 AMU - 0.7%). During measurement of nitrogen permeation through a membrane a problem arises from outgassing of carbon monoxide from the vacuum chamber walls because CO also has atomic mass 28 AMU. If the rate of diffusion at 28 AMU from CO is considerably higher than the measured N_2 flow through the membrane; (this equates to the Δp_0 in Equation 3.2), the permeation of N_2 cannot be measured.
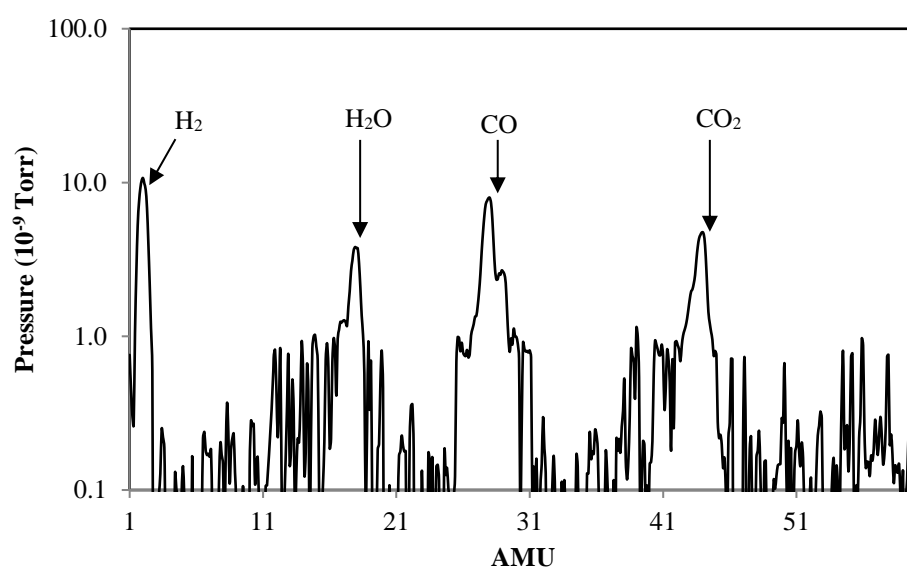
Figure 3.21. Graph showing a typical background reading of gases obtained by mass spectrometry in the UHV apparatus.

4. Mechanical characterisation of nanocrystalline graphite using buckled microstructures

4.1 Introduction

MEMS and NEMS devices are fabricated in a similar way to integrated electronic circuits, by patterning and etching of thin films on substrates. However, MEMS have moving mechanical parts as well as electrical parts. The Young's modulus ($E)$ of the material is fundamental to the behaviour of MEMS and NEMS devices which undergo any actuation, sensing or deflection. In this Chapter, I have measured the value of E of the nanographite thin film.

Techniques of characterising E of thin films, using released microstructures, were first described in the late 1970's [127] by measuring the resonant frequency of cantilever beams. Some other methods to measure E using microstructures are summarised here. Sundararajan *et al.* [128] fabricated micro-beams from silicon and SiO_2, and then used atomic force microscope to deflect the beams in a 3-point-bend test. This is a downscaled version of the method described in international standards [129] for measuring E for macroscopic samples. Another very widely used technique for measuring both the built-in stress and E of thin films is known as the 'bulge test'[130] which has recently been used to measure the these two properties of Silicon Carbide [54]. In the bulge test, membranes are subjected to a pressure on one side, and the deflection of the membrane can be used to calculate both the stress and E.

There are various methods of characterising the Young's modulus of thin films. In order for accurate measurement of this physical parameter, all experimental errors must be taken account of. Osterberg *et. al*. state that a reasonable goal for accuracy should be within a few percent [131] and this is generally the order of error stated in literature [54,127,132]. Experimental errors may arise from fabrication imperfections, such as over-etching, or excessive curvature due to stress gradients. These imperfections create boundary conditions which are different to the typically 'ideal' models, and may create significant differences if not accounted for [131].

Here, two types of released microstructures using nanographite thin films were fabricated: membranes and beams. Nanographite, when deposited onto a silicon substrate, is under a high compressive built-in stress. As a result, both types of structure exhibit a significant out-of-plane buckling when they are released. This is generally not sought after for MEMS; nonlinear buckling of structures creates difficulty in modelling and design. However, in this Chapter I have used the buckling effect as a measurement tool. The amplitude of both types of buckled structure is a function of E. Firstly, I used white light interferometry to measure the deflection of a number of buckled membranes, and fitted these results to an analytical model for buckling of membranes, to extract a

value for *E*. Using this value, I then used analytical and finite element models to predict the amplitude of doubly-clamped buckled beams. Finally, these results were compared with the experimentally measured buckling amplitude. I also present the material characterisation of nanographite by Raman spectroscopy and scanning electron microscopy. These results help to describe the grain structure of the material, thereby enabling a clear comparison with other carbon thin films.

This work is based on my publication "S. J. Fishlock *et al.* Mechanical characterisation of nanocrystalline graphite using micromechanical structures, Microelectronic Engineering. 159 (2016)."

4.2 Material characterisation of nanographite

Graphitic materials are varied and may have a very wide range of electrical and mechanical properties. The large variation is largely due to the grain structure of graphite, which is highly anisotropic. The in-plane covalent bonds are very stiff, whilst the out-of-plane van der Waals bonds are very weak [133]. As a result, it is difficult to accurately predict *E* for graphitic materials, which may vary from very low: 10 GPa [134] , to very high: 1060 GPa [5]. Here, the results of material characterisation using Raman spectroscopy are presented, to relate the mechanical and structural properties of nanographite.

4.2.1 Raman Spectroscopy

Raman spectroscopy (Renishaw inVia) was used to characterise the structural properties of the nanographite film, using a 532 nm wavelength excitation laser, with a spot size of around 10 µm. Raman is a non-destructive characterisation technique, and was performed on the thin film when it was still adhered to the substrate, prior to the microfabrication of any devices.

A Raman spectrum obtained from a nanographite thin film is shown in Figure 4.1, with the main peaks highlighted. The D peak at 1350 cm^{-1} arises from defects within the graphite lattice, such as grain boundaries and dislocations [135]. The G peak is so-called as it shows graphite is present and arises from graphitic bonded carbon. The 2D, also known as G' peak also arises from graphite bonds, and D+D' is related to the defects in the material. The amplitude of the D peak with respect to the G peak I_D/I_G of 1.7 shows that this is a nanocrystalline graphite [81].
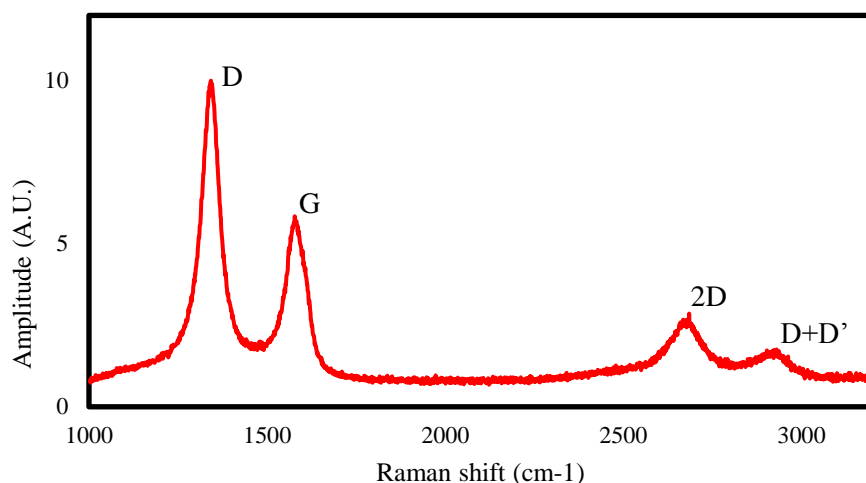
Figure 4.1. Raman spectrum of nanographite with main peaks denoted.

4.2.2 Scanning electron microscopy

Scanning electron microscopy is a useful tool to visually examine the crystal structure of a material. Figure 4.2 shows an SEM image (taken with a JEOL JSM FESEM 6700F). The image shows crystallites which are generally of diameter below 50 nm.
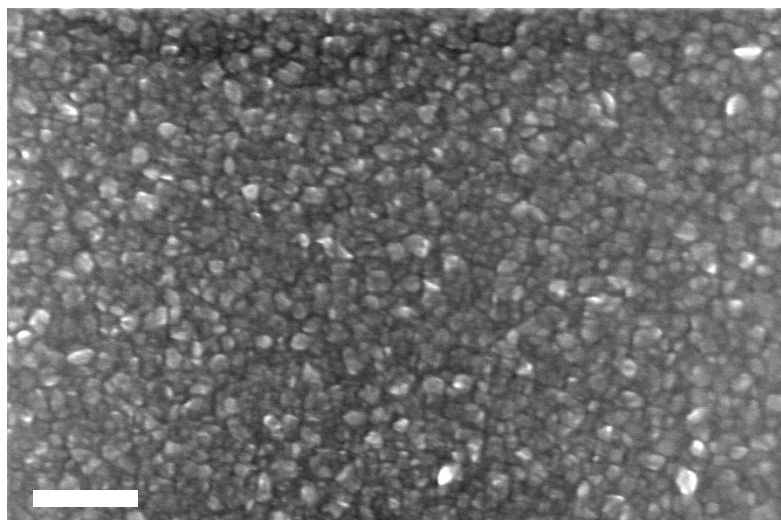
Figure 4.2. SEM image showing the surface of a nanographite film. The scale bar is 200 nm.

4.2.3 X-ray reflectivity for density measurement

X-ray reflectivity was performed on a nanographite film deposited on a fused quartz substrate. The data for this was fitted using 'X'Pert Reflectivity' software and the plot of the X-ray reflectivity intensity with angle of incidence is shown in Figure 4.3. This measurement is used to empirically obtain the mass density of the film. The data was fitted to a generic model for carbon which gave a mass density of 1900 kg m^{-3}.
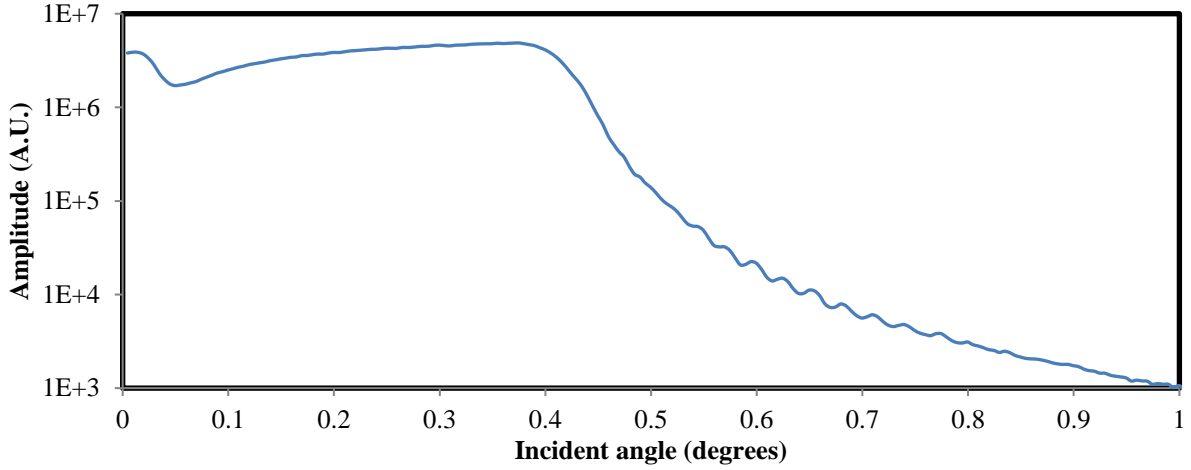
Figure 4.3. X-Ray reflectivity intensity vs angle of incidence for a nanographite 240 nm film on a fused quartz substrate.

4.3 Theory governing the buckling behaviour of beams and membranes

4.3.1 Membrane buckling

A structure, such as a membrane or beam, under compressive loading F, will deflect linearly if the magnitude of the load lies below a critical buckling load F_{crit} as shown in Figure 4.4 (A). If the magnitude of the load is increased beyond a critical buckling load, the structure will not be able to deflect linearly and will be forced to buckle out-of-plane as in Figure 4.4 (B). The amplitude of the post-buckled state is a function of both the size of the load F and the stiffness of the structure, and this relationship may be used to calculate E for the material.
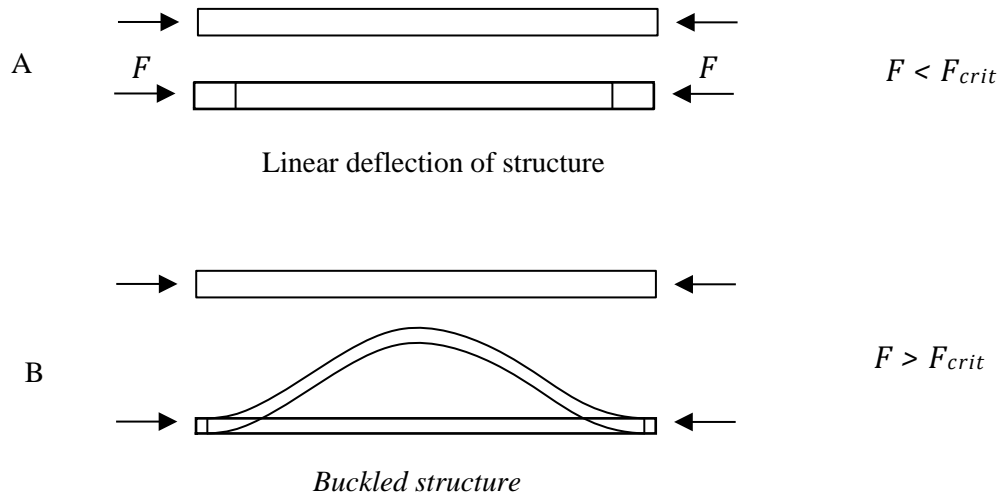
Figure 4.4. Schematic of how a structure can undergo: (A) Linear deflection under small compressive loads. (B) Buckling under higher compressive loads.

In work by Ziebart *et al.* [136] the buckling behaviour of square micromechanical membranes was analysed and presented as a method to measure the Young's modulus of silicon nitride (Si_3N_4). Here,

56

the buckling characterisation of membranes is applied to nanographite membranes, the fabrication for which was described in Chapter 3. An example of a nanographite buckled membrane can be viewed in Figure 4.5. The membrane buckling pattern may at first appear random, but on closer inspection has a clear rotation symmetry which can be predicted mathematically.
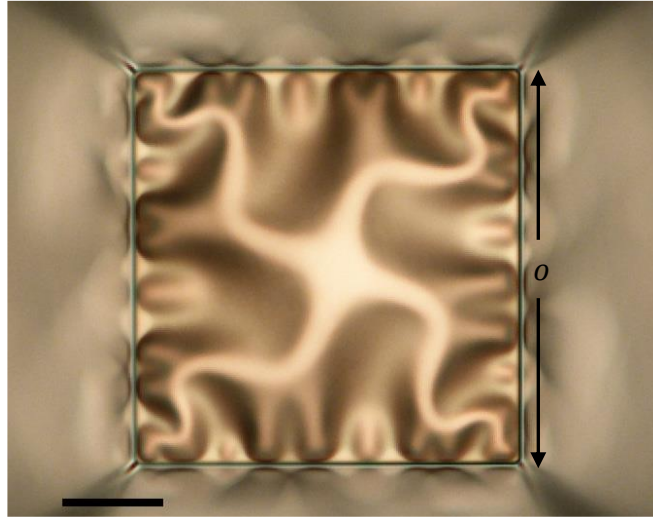
Figure 4.5. Optical microscope image, taken from the back-side showing a buckled nanographite square membrane of 193 µm side-length o. Scale bar is 50 µm.

The geometry of compressively stressed square membranes lies within 3 regimes, defined by their buckling shape, which depends on the level of in-plane stress, σ.

- For regime 1, $\sigma < \sigma_{crit1}$ and the membrane is flat. Here the membrane is not buckled and has no significant out-of-plane deflection.
- In regime 2, when $\sigma_{crit1} < \sigma < \sigma_{crit2}$, the membrane is buckled with rotational and four-fold symmetry (symmetrical about the x- and y-axes and the 45 ° diagonals). As the level of buckling increases, the shape becomes increasingly complex, with further stages of wrinkling progressing.
- In regime 3, $\sigma > \sigma_{crit2}$ and the membrane is buckled with rotational symmetry only. All the nanographite membranes are in this regime. Figure 4.5 shows an example of a nanographite membrane buckled in this stage.

The mathematical analysis of Ziebart *et al.* using energy-minimisation technique of the buckling behaviour of square membranes is summarised here. In this analysis, trial displacement functions are applied to the deformation of the membrane, the boundary conditions are set as zero displacement along the membrane clamped sides. From the strain energy analysis of the trial functions, an energy minima which represents the true deformation of the membrane may be found. The analysis is performed for an isotropic material. Polycrystalline and nanocrystalline materials may be

approximated as having an isotropic Young's modulus, as the anisotropic elastic constants (in graphite, the mismatch between stiff, covalent in-plane bonds and flexible Van der Waals out-of-plane) are negated by the mismatch in angle between individual grains. Similar behaviour is observed in isotropic graphite [134], DLC and nanocrystalline diamond [137].

This analysis establishes a relation between the maximum out-of-plane amplitude of a buckled square membrane, and the in-plane strain of the material. The analysis uses dimensionless displacements where the pre-strain $\overline{\varepsilon}_0$ is given in Equation 4.1, in terms of the strain ε, side length o, and thickness h. The strain ε is the physical built-in strain of the material. The dimensionless prestrain $\overline{\varepsilon}_0$ is a function of the strain which accounts for the physical dimensions of the membrane, for a simpler mathematical analysis.

$$\overline{\varepsilon}_0 = \frac{\varepsilon \cdot o^2}{h^2} \tag{4.1}$$

The dimensionless deflection $\overline{w}$ is defined in terms of the real maximum deflection w:

$$\overline{w} = \frac{w}{h} \tag{4.2}$$

From their work, and accompanying simulation, a fitted displacement function was extracted. This enables a relatively simple extraction of the pre-strain $\overline{\varepsilon}_0$ by measuring the maximum amplitude of buckling. This function can be calculated as:

$$\overline{w}_{0\,fit} = \sqrt{\Delta\overline{\varepsilon}_0(c_1 + c_2 \tanh\left\{c_3\Delta\overline{\varepsilon}_0\right\} + \frac{\left\{c_4\Delta\overline{\varepsilon}_0 + c_5\Delta\overline{\varepsilon}_0^{\,2}\right\}}{1 - c_6\Delta\overline{\varepsilon}_0^{\,3}}} \tag{4.3}$$

Where $\overline{w}_{0\,fit}$ is the measured maximum buckling amplitude and where the fitting parameters $c_1 - c_6$ are calculated as in Equation 4.4, where v is the Poisson's ratio.

$$\begin{pmatrix} c_1 \\ c_2 \\ c_3 \\ c_4 \\ c_5 \\ c_6 \end{pmatrix} = \begin{pmatrix} -0.4972 & -0.2314 & -0.2128 \\ 0.0698 & 0.1625 & 0.200 \\ -7.19\times10^{-3} & -0.0466 & 0.0367 \\ -1.19\times10^{-3} & 0 & 5.51\times10^{-3} \\ -3.34\times10^{-6} & -7.43\times10^{-5} & 1.28\times10^{-4} \\ 3.16\times10^{-6} & 4.80\times10^{-6} & -1.52\times10^{-5} \end{pmatrix} \bullet \begin{pmatrix} 1 \\ v \\ v^2 \end{pmatrix} \tag{4.4}$$

The deflection $\overline{w}_{0\,fit}$ obtained from Equation 4.4 is a weak function of the Poisson's ratio of the material. The constants in Equation 4.4 were obtained empirically from computer simulations, measuring the deflection of materials of Poisson's ratio $0 \leq v \leq 0.5$.

The stress has been separately calculated by measuring the change in the level of deflection or bowing of the substrate before and after the deposition of the nanographite film, using the commonly used

Stoney's Equation (4.5) [138], where σ_0 is the biaxial film stress, E_S is the Young's modulus of the substrate, v_s is the substrate Poisson's ratio, h_s and h_f are the thickness of the substrate and film respectively, and u_0 and u are the radius of curvature before and after film deposition.

$$\sigma_0 = \frac{E_s}{6(1-v_s)}\frac{h_s^2}{h_f}\left(\frac{1}{u}-\frac{1}{u_0}\right) \tag{4.5}$$

From the measured values of stress and strain, ε, E can be extracted from the definition of biaxial stress [136]:

$$E = \frac{(1-v)\sigma_0}{\varepsilon} \tag{4.6}$$

From the calculated values of stress and strain, ε, E can be extracted from the definition of biaxial stress [136]:

4.3.2 Beam buckling

I have then measured the buckling amplitude of doubly-clamped beams, in order to provide a second, independent measurement of the Young's modulus of the nanographite film. This has been done by measuring the buckling amplitude of nanographite buckled beams, and fitting the experimentally measured value of beam buckling amplitude to (i) an analytical model and (ii) a finite element (FE) simulation model.

An analytical solution for the amplitude of a doubly-clamped beam is presented by Nayfeh *et al.* [139]. The beam follows the cosine mode shape as described in Equation 4.7, where the non-dimensional amplitude w along the length x is given by:

$$w(x) = s\left[1-\cos(2\pi x)\right] \tag{4.7}$$

where

$$s = \pm 2\sqrt{\frac{Fl^2}{EI\lambda^2}-1} \tag{4.8}$$

and

$$w = \frac{\hat{w}}{\sqrt{I/a}} \tag{4.9}$$

and

$$I = \frac{bh^3}{12} \tag{4.10}$$

where l is the beam length, the in-plane force is F, and second moment of area is I, calculated using Equation 4.10 where b is the beam width and h is the beam thickness. The cross-sectional area of the beam is a, λ is an eigenvalue corresponding to the mode shape and $\hat{w}$ is the out of plane buckling amplitude. Since the beam is considered a 'wide' beam (of a width to thickness ratio $b/h > 5$), it is under a plane strain condition and E may be modelled as an effective Young's modulus

$\widehat{E} = E / (1 - v^2)$ [131]. The plane strain condition is a simplification that satisfied in 'wide' beams as there is negligible strain through the beam thickness.

4.4 Simulation of the mechanical behaviour of nanographite buckled beams

The analytical result shown in Equation 4.7 models the structure as a perfect beam, with the effective boundary conditions shown in Figure 4.6 (A). However, as a result of the fabrication process, there is one clear imperfection between the modeled structure and the real structure. The release process creates 'steps' or 'kinks' in the beam at either clamped end, equal to the thickness of the sacrificial layer, shown schematically in Figure 4.6 (B).
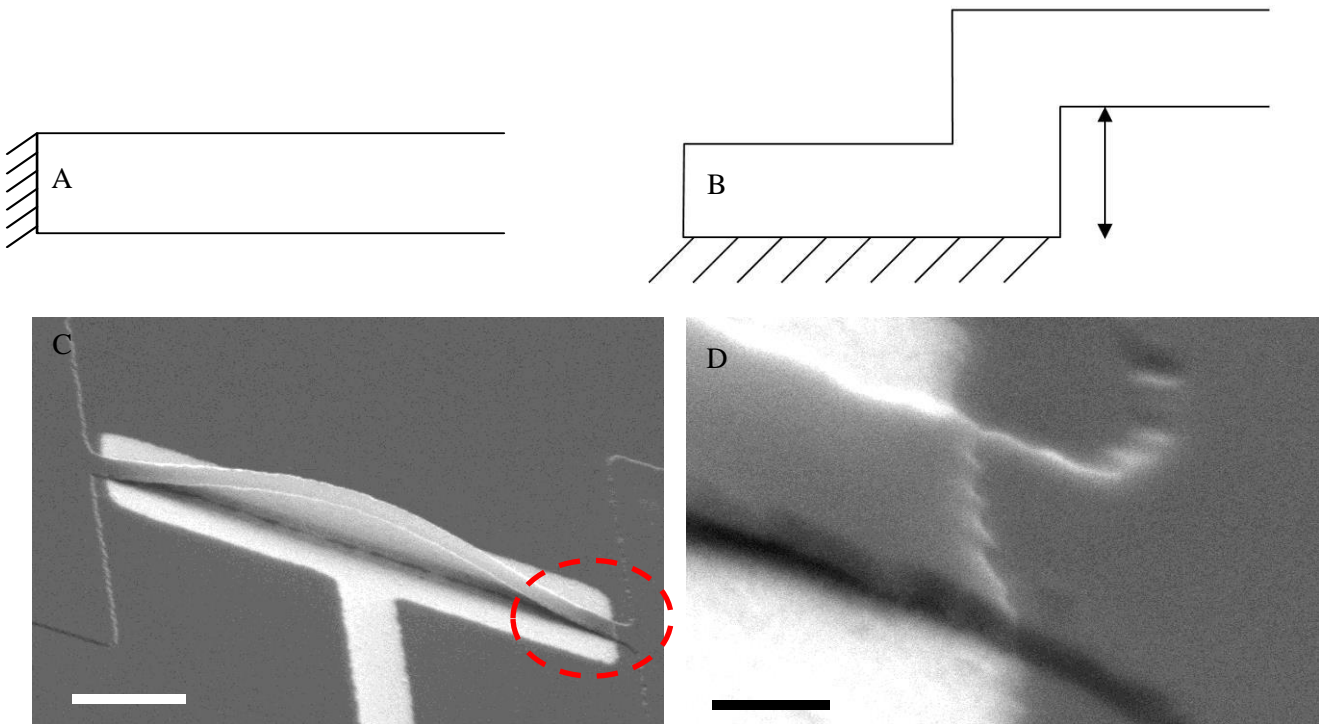
Figure 4.6. (A-B) Comparison of the ideal and actual clamping conditions of the fabricated beams. (C-D) SEM images of the clamping conditions of a buckled doubly-clamped beam. (D) is a higher magnification of the circled region in (C). Scale bars are 30 and 3 µm, respectively, for (C) and (D).

To account for the imperfection of the fabricated structure, the doubly-clamped beams were modelled using FE analysis software ANSYS. This was performed by applying biaxial thermal strain to the beam. The Young's modulus of the model was varied until the simulated value of the buckling amplitude matched that of the experimental structure.

The beam was modelled using 2D shell elements (SHELL 281). Nonlinear static analysis was undertaken, with the maximum buckled amplitude measured. Figure 4.7 shows part of the model end clamping conditions, with the stepped anchors modelled on Figure 4.6 (D). The results are presented in the following subsection alongside the experimental and analytical values. Other input values for

the FE simulation are summarised in Table 4.1. A full input code for the simulation is shown in Appendix 1, with mesh refinement study.
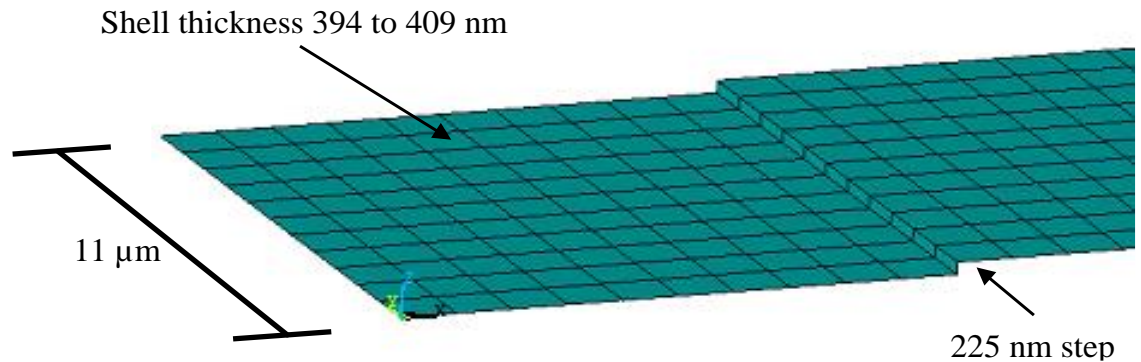
Figure 4.7. An image of a part of an FE model of one of the clamped anchors of the beam.

Young's modulus (GPa)	23
Biaxial stress (MPa)	436
Biaxial strain	-0.01896
Beam length (µm)	65 / 90 / 140
Beam width (µm)	11
Beam thickness (nm)	394 to 409
Step thickness (nm)	225

Table 4.1. Summary of the input values used for FE simulation of doubly-clamped nanographite beams.

4.5 Results of the mechanical characterisation of nanographite using buckled microstructures

4.5.1 Buckling behaviour of nanographite membranes

The buckling amplitude of square nanographite membranes were analysed using white-light interferometry (Polytec MSA-400). The thickness of each membrane was measured using ellipsometry (J. A. Woolham M2000), and side length was measured using optical microscopy. A total of six square membranes were characterised, and an example of the buckling profile obtained through interferometry is shown in Figure 4.8 for a 221 µm long, 281 nm thick square membrane.
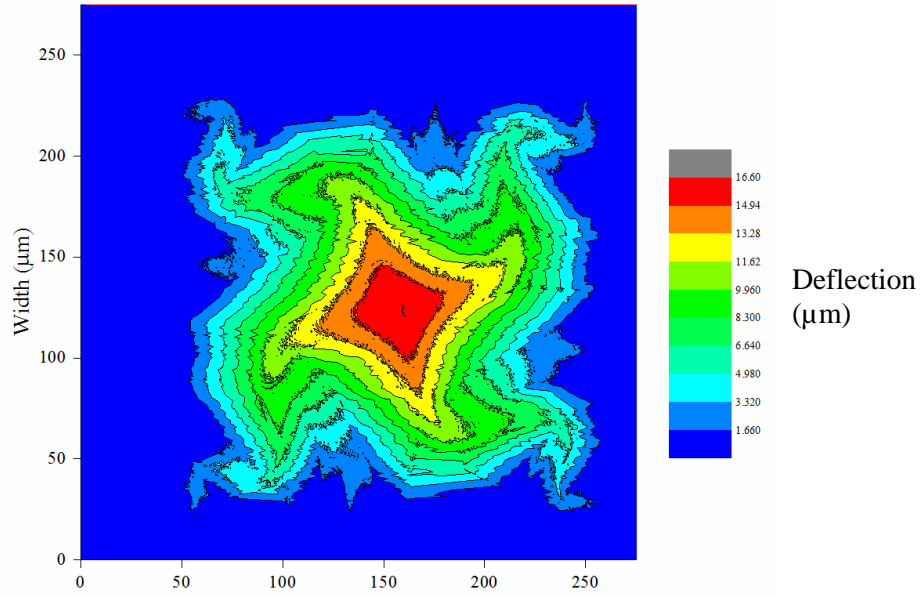
Figure 4.8. Interferometric contour plot taken from the front side of a buckled square membrane of 221 µm.

Side length (µm)	Maximum Deflection (µm)	Thickness (nm)	Strain ε
221.0	16.6	281	-0.013
193.3	15.3	281	-0.014
273.4	24.0	285	-0.017
224.9	19.2	285	-0.016
217.4	15.8	275	-0.012
192.6	14.9	296	-0.013
		Average	-0.014

Table 4.2 Summary of the buckling results for six nanographite square membranes.

Table 4.2 summarises the geometry, deflection and calculated strain results of each membrane. This yields an average strain ε value of -0.0142 (where the negative sign indicates compression). The Poisson's ratio of the nanographite film has not been measured, but a value of this is required here to calculate E. For example, the constants required to calculate the strain in 4.4 show a weak dependency on the Poisson's ratio ν of nanographite. In this case, an estimate that ν lies between 0.17, of highly-ordered graphite, [5] and 0.31, of isotropic graphite [140] was made. A central estimate of 0.25 has been used as the base figure, including for simulation. The error estimation includes the use of these high and low possible values. The stress was measured as 436 MPa, and using Equation 4.6, I obtain a Young's modulus value of 23 ± 1.4 GPa.

4.5.2 Experimental buckling amplitude of microfabricated beams

The microfabricated buckled beams were measured using interferometry (Veeco, Wyko DMEMS NT3300). An interferometry graph of a 140 µm long beam is shown in Figure 4.9 (A) with the corresponding profile in 4.9 (B).
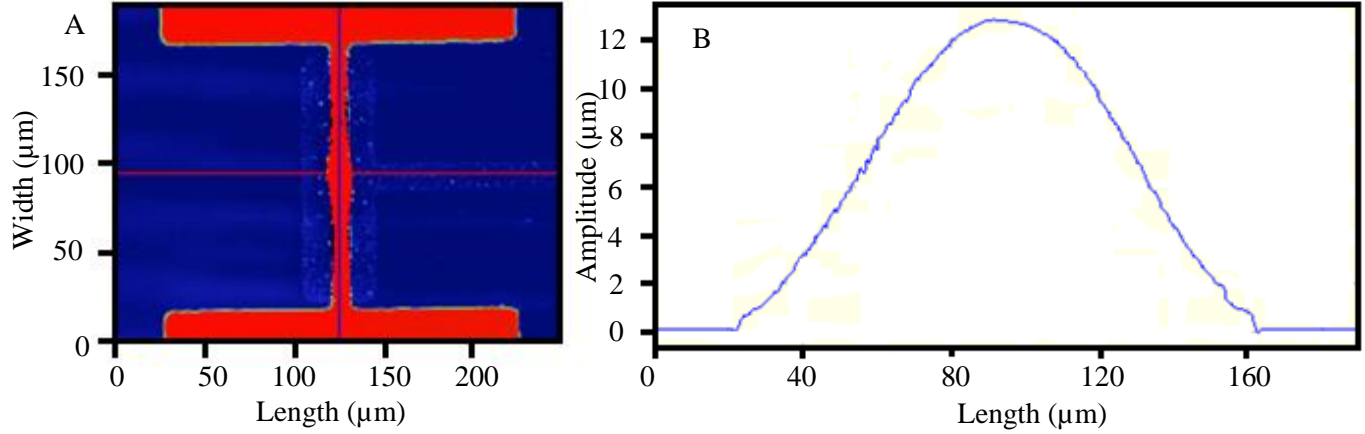
Figure 4.9. (A) Image showing the interferometry graph of a buckled 140 µm beam. (B) The associated profile along the beam.

A summary of the results for the buckling amplitude of beams is shown along with the estimated results in Table 4.3.

4.5.3 Calculating E from the analytical solution of beam buckling amplitude

The buckling profile of doubly-clamped beams of length between 65, 90 and 140 µm (as calculated analytically using Equation 4.7) is shown for three beams length 65 to 140 µm in Figure 4.10. Here, the value of E for each beam was calculated by equating the buckling amplitude of the analytical result to the experimentally measured value. The calculated value of E in each case is shown in Table 4.3, along with the result from the FE simulation.
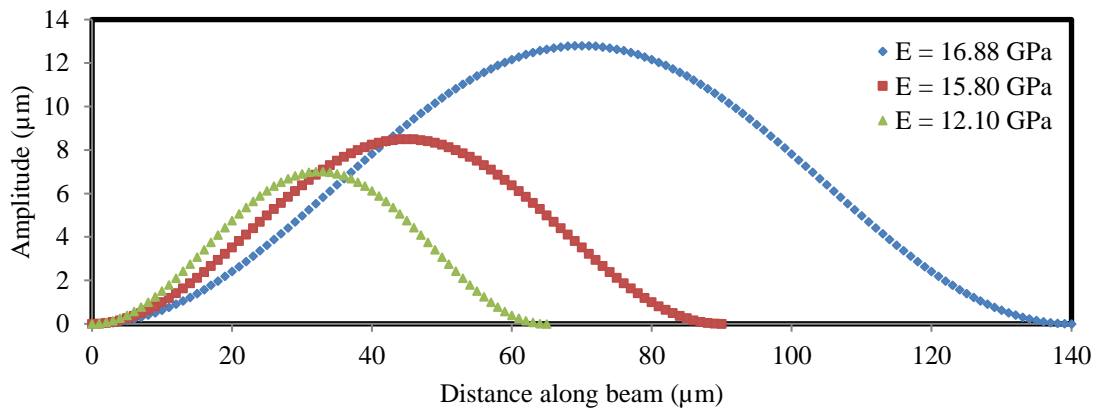
Figure 4.10. Buckling profile of doubly-clamped beams, length 65, 90 and 140 µm, as predicted by the mathematical model.

63

The calculated value of E from the analytical results shows a large range of 12.10 to 16.88 GPa. The calculated value of E increases with the longer beams.

Beam length (μm)	Thickness (nm)	Amplitude measured (μm)	Calculated E, Analytical model (GPa)	Calculated E, FE simulation (GPa)
65.0	409	**7.0**	12.10	15.76
90.0	398	**8.5**	15.80	20.92
140.0	394	**12.8**	16.88	22.01

Table 4.3 Summary of the predicted values of the amplitude of buckled beams through an analytical model and FE simulation, compared with the experimentally measured value.

4.5.4 Calculating E from the FE simulation of beam buckling amplitude

Beams of length 65, 90 and 140 µm were simulated using ANSYS finite element simulation. The input value of E was varied between 15 and 25 GPa, and the maximum amplitude of buckling was calculated. A plot of the value of input E versus the bucking amplitude is shown in Figure 4.11. From this, the calculated value of E which gives an equal result to the experimental buckling amplitude was calculated and shown in Table 4.3. The simulated deflection result of a 140 µm beam, after nonlinear thermal buckling is shown in Figure 4.12-A, and the corresponding Von Mises stress is shown in Figure 4.12-B.
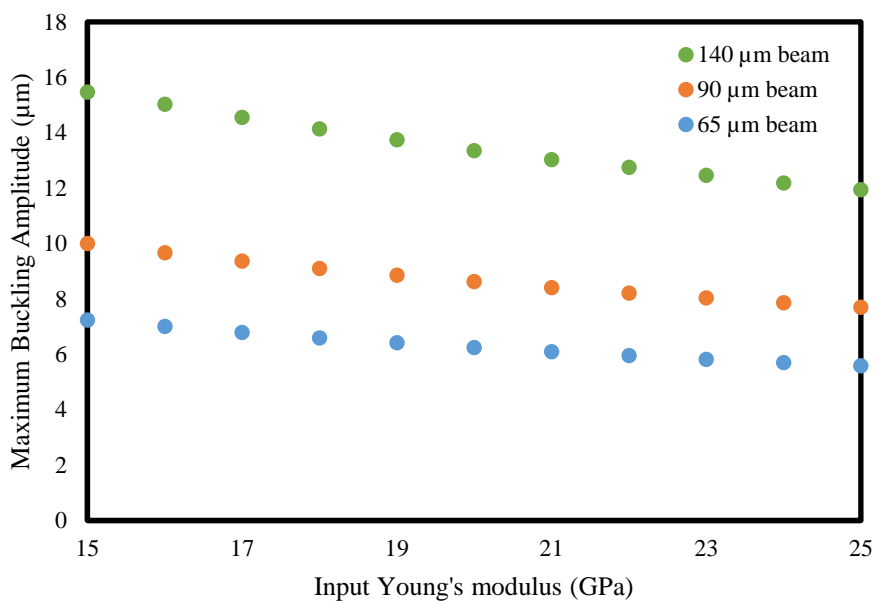
Figure 4.11. Plot showing the variation of buckling amplitude, calculated using FE simulation, with varying input value of Young's modulus.

A

| 0 | 1.41 | 2.83 | 4.24 | 5.66 | 7.07 | 8.49 | 9.90 | 11.3 | 12.7 |

Deflection (µm)

B

| 0.00 | 0.16 | 0.31 | 0.47 | 0.63 | 0.78 | 0.94 | 1.10 | 1.25 | 1.41 |

Stress (GPa)
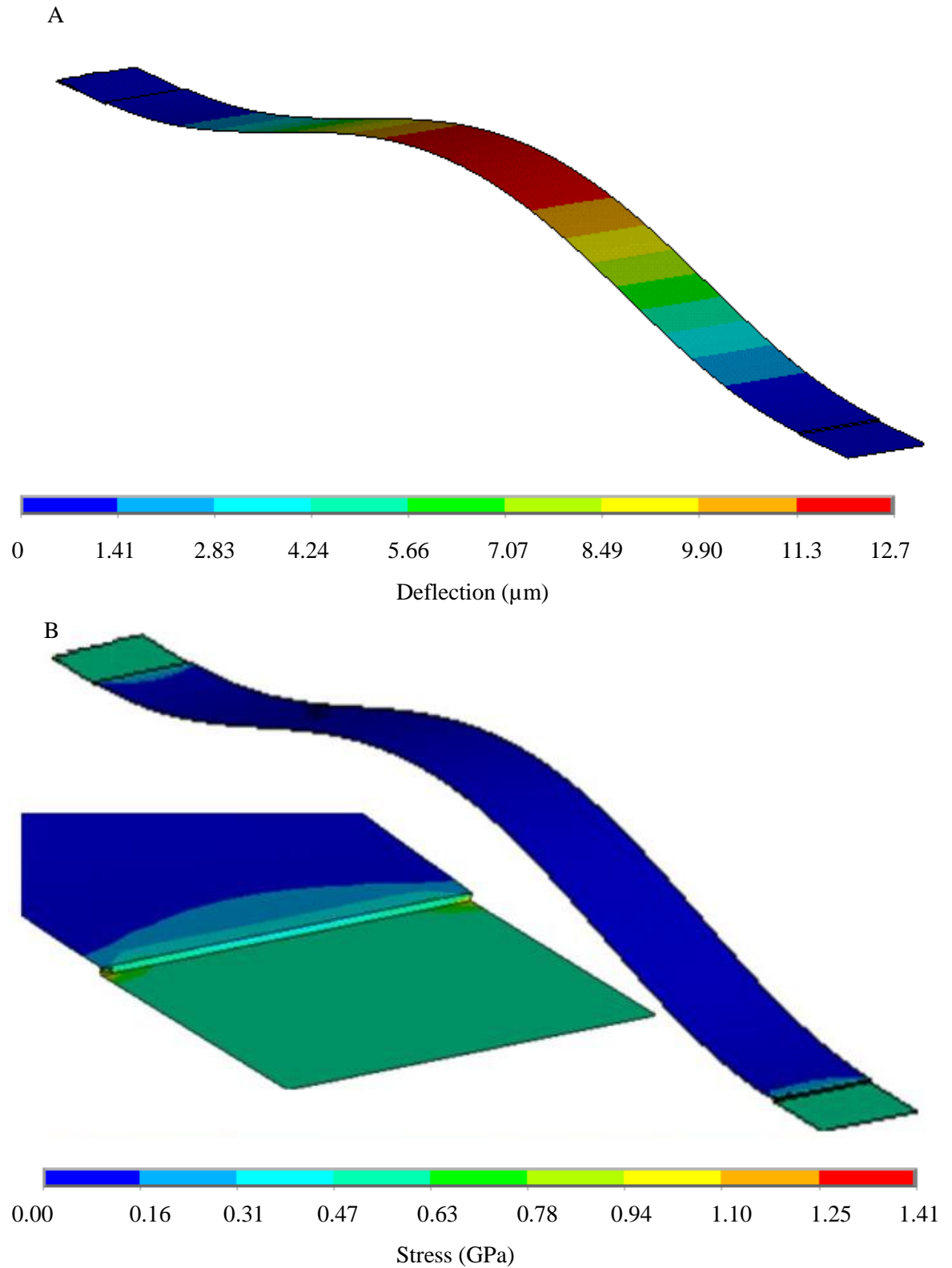
Figure 4.12. FE simulation result of the buckling amplitude of a 140 µm long nanographite beam, with $E = 22.0$ GPa input. (A) Result showing the deflection (B) Result showing the Von Mises stress of the same simulation.

The simulated results give a range of E values between 15.76 to 22.01 GPa. This is lower than calculated using the membrane structures, but higher than calculated from the analytical model of beam buckling. The disparity between the result extracted from the FE simulation and analytical models to be expected as the FE result more closely models the real structure. In the real structure, the steps act as local stress concentrators, thereby lowering the effective stiffness of the structure. Figure 4.12-B shows the Von Mises stress plot of the buckled beam. This confirms that the stress is concentrated at these steps caused by the release of the beam.

4.5.5 Comparison of the predicted and measured values of buckling amplitude of beams

A comparison of the value of E extracted from the FE simulation and analytical results is made here. For both FE and analytical models the value of E is lower than that calculated from the membrane structures. Both sets, however, show a trend of increasing value of E at the longest beam lengths (with closest agreement at 140 µm).

The different results obtained from the analytical method and FE simulation suggest that the imperfections caused by fabrication (the steps in the structure) have a large effect on the buckling behaviour. Consequently, the results obtained by modelling the buckled structure using the 'ideal' analytical method should be treated with caution, and the FE result should be preferred.

The FE results show closer agreement with that obtained using the buckled membranes, but there is still a relatively large range of results (15.76 to 22.01 GPa), with a mean value of 19.56 ± 5.16 GPa. There appears to be a systematic error which affects the buckling behaviour of shorter beams more strongly. Kobrinksy *et al.* [141] found a similar behaviour, whereby shorter beams were found to buckle at significantly lower loads than were predicted ideally. The amplitude of buckling for shorter beams was also larger than predicted in their simulations. This was due to some compliance, residual stress and rotation in the beam anchors which may not be fully accounted for in the FE analysis. As a result, the most reliable result obtained for E from the buckled beams is most likely from the 140 µm beam (22.01 GPa), which is in agreement with the result obtained using the membranes (23 ± 1.4 GPa).

4.6 Discussion of results

4.6.1 Comparison with the mechanical properties of other related carbons

In this Chapter, the static buckling of membranes and beams have been used to extract E of thin film nanographite. The measured E value extracted as 23 GPa is relatively low compared with pristine graphite or graphene and other carbon forms such as diamond-like carbon (~300 GPa) [11]. The value is more similar to that obtained by poorly orientated graphitic materials, such as isotropic graphite with E of 9.5 GPa [134]. Table 4.4 summarises the Young's modulus, and notes the grain

structure of a number of related carbon materials. *E* for polycrystalline graphite is strongly dependent on the orientation of its grains, and the misalignment between grains parallel to the substrate causes a low in-plane stiffness [133]. In less-oriented graphite *E* becomes dominated by the weak van der Waals inter-grain forces.

Material	Grain structure, size	In-plane Young's Modulus (GPa)
Highly-ordered pyrolytic graphite [5]	Well aligned graphite grains, 20 to 50 µm.	1060
Pyrolytic graphite [142]	Average grain size ~ 32 nm.	83.5
DLC [83]	Mixture of diamond and graphitic bonding.	300
Nanocrystalline diamond [78]	All diamond bonds, 5 to 15 nm grain size.	840
Isotropic graphite [134]	Isotropic graphite, ~20 µm grains size.	9.5
Single crystal graphene [62]	Single layer of graphite without grain boundaries.	1000
This work [143]	**Grain size 30 to 50 nm. Primarily graphitic bonding.**	**23**

Table 4.4. Comparison of the Young's modulus of the nanographite obtained in this work with other related carbons.

The membrane length dimensions were measured using an optical microscope, with an accuracy of ± 2.5 µm and the thickness was measured using ellipsometry, by averaging three points around the membrane edge, with an error of ± 5 nm. To measure the thickness of a film using ellipsometry, the change in polarisation of light is measured, which is then fitted to a model of the film with optical constants and extinction coefficient. The main source error associated with ellipsometry is due to imperfections in the modelling of the film. The amplitude of buckling was measured using white light interferometry, and was repeated three times with an error of ± 0.1 µm, which is the resolution of the interferometer. The combined errors of all these geometric uncertainties were accounted for in the quoted value of strain and Young's modulus.

The beam dimensions were measured using an optical microscope with an error of ± 2.5 µm, and thickness was measured using stylus profilometry, averaged over three measurements with an error of ± 5 nm. The amplitude of buckling was measured using white light interferometry, and was repeated three times with an error of ± 100 nm.

<u>4.6.2 Potential use of nanographite in MEMS and NEMS</u>

The work in this Thesis is geared towards using and characterising nanographite in MEMS and NEMS applications. Many such applications require a material of high stiffness, which may be obtained using materials (1) such as diamond, which has a high value of E or (2) materials which have a large tensile stress such as Si_3N_4 [2]. The greater stiffness of such materials enables, for example, higher natural frequencies for resonators. As a result, most MEMS research has been geared towards high E and high tensile stress materials. However, for some applications, materials with low stiffness may be sought after. Nanographite shows promise as a material for MEMS, particularly for applications where the combination of low E, good electrical conductivity and high temperature resistance are required. For example, two possible applications are:

- A membrane made of nanographite has a higher deflection to an applied pressure and may therefore have a higher sensitivity over a stiffer material. The high temperature properties can enable use in harsh environments, such as pressure sensing in combustion engines [46].
- A NEMS switch which has a lower pull-in voltage compared with one fabricated from a high modulus material. Indeed, in recent work the use of buckled nanographite for use in NEMS switches has been demonstrated [68]. However, the modulus value extracted from this work is 860 GPa; considerably larger than the value obtained here. The reason for the disparity of result is clear: that work uses a lumped or effective modulus which does not separate the effect of stress on the bending stiffness.

The results have highlighted an issue of note with respect to the fabrication of released nanographite MEMS-type structures; that fully-clamped structures, where the compressive stress cannot be released, leads to buckling. This is clearly undesirable for most types of application, and some methods to reduce the level of compressive stress have been employed for other materials. For example in Si_3N_4 deposited using PECVD, tuning of the parameters of deposition may be used to lower built-in stress [144]. Using a different substrate or a composite substrate may also be used to lower the thermal stress [145]. Such techniques may be useful to fabricate nanographite structures with low compressive stress or moderate tensile stress.

<u>4.6.3 Summary and conclusions</u>

In this Chapter, I have used two types of micromechanical structure to measure the Young's modulus of nanographite. Both types of structure were buckled due to the in-built compressive stress in the nanographite film, which arises from thermal mismatch, and intrinsic stresses due to deposition. Buckling of this nature is not typically desirable for MEMS-type applications, however in this case I used the buckling behaviour to measure E for nanographite, which is a key parameter for designing MEMS.

I measured the buckling profile of square nanographite membranes and fitted the result to a mathematical model to calculate the in-built strain, which gave a value of -0.0142. Separately the biaxial stress was measured as 436 MPa and from these two measurements a value of 23 ± 1.4 GPa for the Young's modulus was obtained.

I then repeated a similar experiment, using the buckling behaviour of doubly clamped beams, and calculated the value of E from these structures, for an independent measurement, using an analytical model and using FE simulation. From this analytical model, values of E between 12.10 to 16.88 GPa were obtained, significantly below that calculated using the membranes. The FE results gave a range of E between 15.76 to 22.01 GPa, higher than the analytical model results. The FE analysis showed that the microfabrication imperfections lowered the overall stiffness of the structure by concentrating stress at the beam anchors (which was not accounted for in the simple analysis). As a result, the mathematical analysis is likely to underestimate the value of E. The value of E calculated from the FE was in the range of 15.76 to 22.01 GPa, with a mean value of 19.56 ± 5.16 GPa. However the result systemically increased with longer beams. Comparable results have been observed in similar studies of buckled micro beams [141] whereby shorter beams were found to buckle at significantly lower loads than were predicted ideally. Consequently, the result obtained using the longest beam likely represents the most accurate value (22.01 GPa) which is in agreement with that obtained using the membranes (23 ± 1.4 GPa).

5. Using nanographite in MEMS resonators

5.1 Introduction

A resonator is a structure which naturally oscillates with a high amplitude at certain 'natural' frequencies and can be made on the microscale by the fabrication of thin films. In Chapter 3, I described the fabrication of doubly-clamped and cantilever beams from nanographite for use as MEMS resonators. Such devices may be used as sensors of pressure [31] mass [40] and strain [42].

Novel materials for resonators are under research in order to extend their usage into harsh conditions, such as in high temperature [56] or under corrosive and radiative environments [146,147]. Nanographite is a potential candidate for such applications due to the combination of its characteristics: large-area deposition, the retention of mechanical properties at high temperature for graphitic materials [7] and chemical resistance [113]. PECVD may also be used to deposit films of ultra-low thickness (2.5 to 3 nm [22,66]) which may be used to fabricate downscaled NEMS devices, for use as high resolution sensors, for example. Here, however, thicker films (> 300 nm) have been used for MEMS-scaled structures, to demonstrate methods of fabrication for nanographite MEMS, and to characterise its performance as a resonator.

I present the results and analysis of the use of electrostatically-actuated MEMS nanographite resonators; both doubly-clamped and clamped-free (cantilever) beams. I made arrays of devices using microfabrication, and present a method of obtaining a tensile stressed structure from a thin film of overall compressive stress. This is achieved through altering the undercut and beam clamping conditions. I studied the effect of the undercut on the resonance of cantilevers using finite element simulation. I used laser Doppler vibrometry (LDV) to characterise the natural frequencies and quality factor of a number of devices under ambient and vacuum conditions. The work here is aimed to demonstrate the use of nanographite within a prototype device to provide knowledge for future applications.

5.2 Theory of resonators

5.2.1 Basic theory of resonance and resonators

The resonance of a structure occurs where the amplitude of its oscillation becomes large at certain natural frequencies, where a natural mode shape of vibration is excited. This concept can be used in resonator-based sensors, for example, where a physical stimulus, such as an added mass or stress creates a change in the natural frequency. Here, the background and theory for the resonant frequency of structures is presented.

A resonator may be simply modelled as a single degree-of-freedom (SDOF) mechanical system, with a varying force F at radial frequency ω applied to the mass m of the system, connected to a spring of stiffness k and damping coefficient c as in Figure 5.1 (A). The Equation of motion for this system can be written as [148]:

$$kx + c\dot{x} + m\ddot{x} = F\cos\omega t \tag{5.1}$$

The natural frequency ω_0 (rad s^{-1}) and f_0 (Hz) of a structure of spring constant k and mass m can be obtained using [148]:

$$\omega_0 = \sqrt{\frac{k}{m}} \rightarrow f_0 = \frac{1}{2\pi}\sqrt{\frac{k}{m}} \tag{5.2}$$

Equation 5.1 may be quite confusing when compared to a real resonator structure. In Figure 5.1, the cantilever beam is *both* the mass and spring of the system and is in this case damped primarily by viscous damping of the surrounding environment, represented by gas molecules.
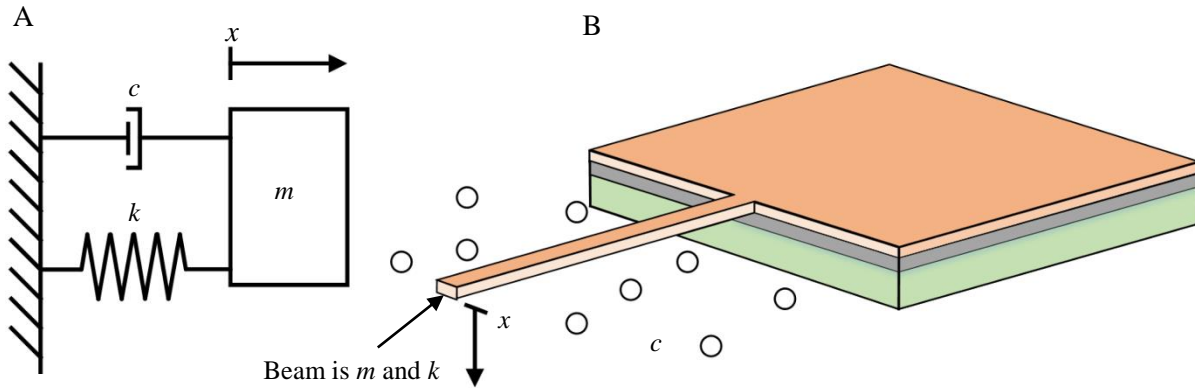
Figure 5.1. (A) Schematic showing a model of a spring-mass-damper system and (B) how this relates to a model of a cantilever beam.

Whilst Equation 5.2 relates to the motion of any generic SDOF harmonic oscillator, the structures under analysis are beams, which as noted above, represent both the mass and spring in the system. The natural frequency f_0 of a cantilever beam is calculated using Equation 5.3, where the length of the beam is l, Young's modulus is E, second moment of area is I, density is ρ and cross-sectional area is a [149].

$$f_0 = \frac{1}{2\pi}\left(\frac{1.875}{l}\right)^2\sqrt{\frac{EI}{\rho a}} \tag{5.3}$$

The amplitude of a forced structure at resonance can be described as in Equation 5.5, where x is the initial static displacement calculated according to Hooke's law [148]:

$$F = k \cdot x \tag{5.4}$$

where F is the applied force and k is the spring constant,

$$x_{steady-state} = \frac{x}{\sqrt{\left(1 - \left(\frac{\omega}{\omega_0}\right)^2\right)^2 + \left(2\zeta\frac{\omega}{\omega_0}\right)^2}} \cos\left(\omega t - \phi\right) \qquad (5.5)$$

where ζ is the damping ratio. This gives the ratio c/c_c where c_c is the critical damping level. This is defined as the level of damping which provides the fastest approach to steady-state vibration amplitude.

The steady-state amplitude of the system becomes large when the forcing frequency ω becomes close to the natural frequency ω_0. Figure 5.2 shows the variation of amplitude for a system, with different damping ratios from 0.01 to 0.03.
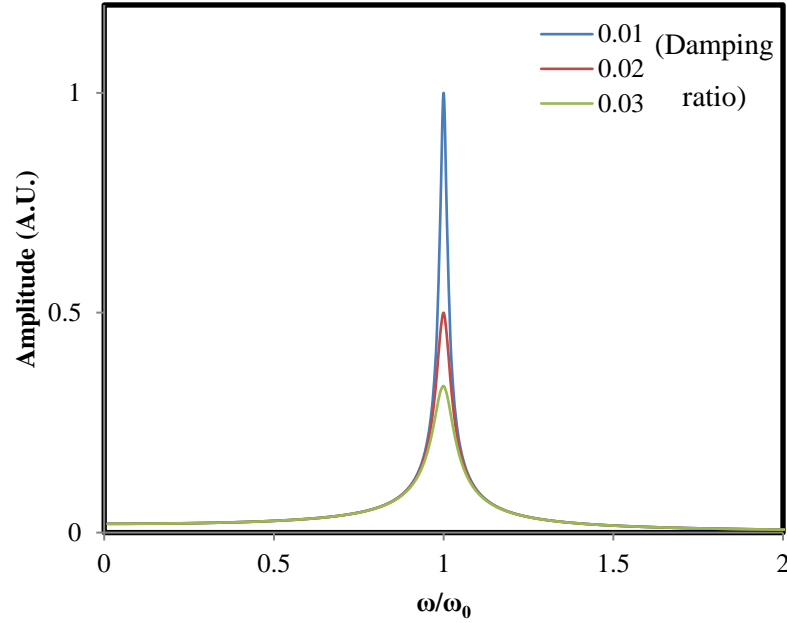
Figure 5.2 Graph showing the relative amplitude of a structure with a force applied at varying forcing frequency, with different damping ratios.

In resonator applications, it is more common to quote the quality factor Q rather than the damping ratio ζ. The quality factor is defined as [150]:

$$Q = \frac{\omega_0}{\Delta\omega} \qquad (5.6)$$

Where $\Delta\omega$ is the full-width at half maximum power. Q is linked to ζ as follows [151]:

$$\zeta = \frac{1}{2Q} \qquad (5.7)$$

<u>5.2.2 Effect of stress on cantilevers and on resonance of doubly-clamped beams</u>

A cantilever is a singly-clamped beam and is unconstrained at one end. In the case of the cantilever, the built-in stress of the material is released through deformation (contraction or bending) at this free end. This is the case for cantilevers made of nanographite, which are under a stress gradient, whereby the top of the film is more compressive than the bottom. Stress gradients cause a resultant moment about the neutral axis of the beam and create downwards curvature in the cantilever as visible in Figure 5.3. The stress gradient of the nanographite was calculated by measuring the curvature u of released cantilever beams by SEM inspection. The stress gradient of a beam of thickness h can be calculated by using Equation 5.8 [43].

$$\sigma_{grad} = \frac{h}{2u}\frac{E}{(1-\nu)}$$
(5.8)
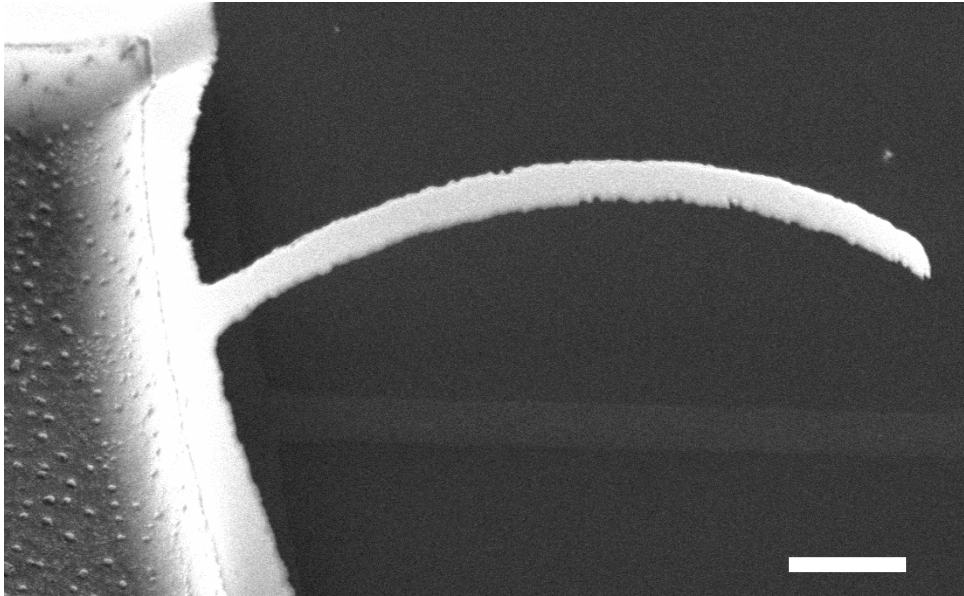
Figure 5.3. SEM image showing the curvature of a released 150 µm long cantilever beam. The scale bar is 20 µm.

For cantilevers the average stress is zero. However, for a doubly-clamped beam, the built-in stress may not be released since the clamping conditions do not allow the beam to elongate freely. In thin film materials deposited at high temperature like nanographite, the stress can be highly compressive or tensile due to differential contraction (from the deposition temperature of 750 °C to room temperature) relative to the substrate. I measured the compressive biaxial stress as 436 MPa using the change in curvature of the silicon substrate due to deposition of the nanographite film (the wafer bow method as described in Equation 4.6).

A beam under high tensile stress is analogous to a guitar string being pulled taut and can produce a large increase in its natural frequency. The natural frequency of a doubly-clamped beam with axial tensile stress σ is calculated as [152,153]:

$$f = \left(1.03\frac{h}{l^2}\sqrt{\frac{E}{\rho}}\right)\sqrt{1+\frac{\sigma l^2}{3.4Eh^2}} \tag{5.9}$$

Figure 5.4 plots a graph of the natural frequency of a theoretical beam under increasing axial stress. It is clear here that even at relatively low values (compared with the amplitude of the in-built compressive stress of nanographite when deposited on silicon), the magnitude of the frequency becomes dominated by the effect of stress.

eam parameters	
ength (μm)	150
idth (μm)	10
ickness (nm)	350
oung's modulus (GPa)	23
ensity (kg/m³)	1900
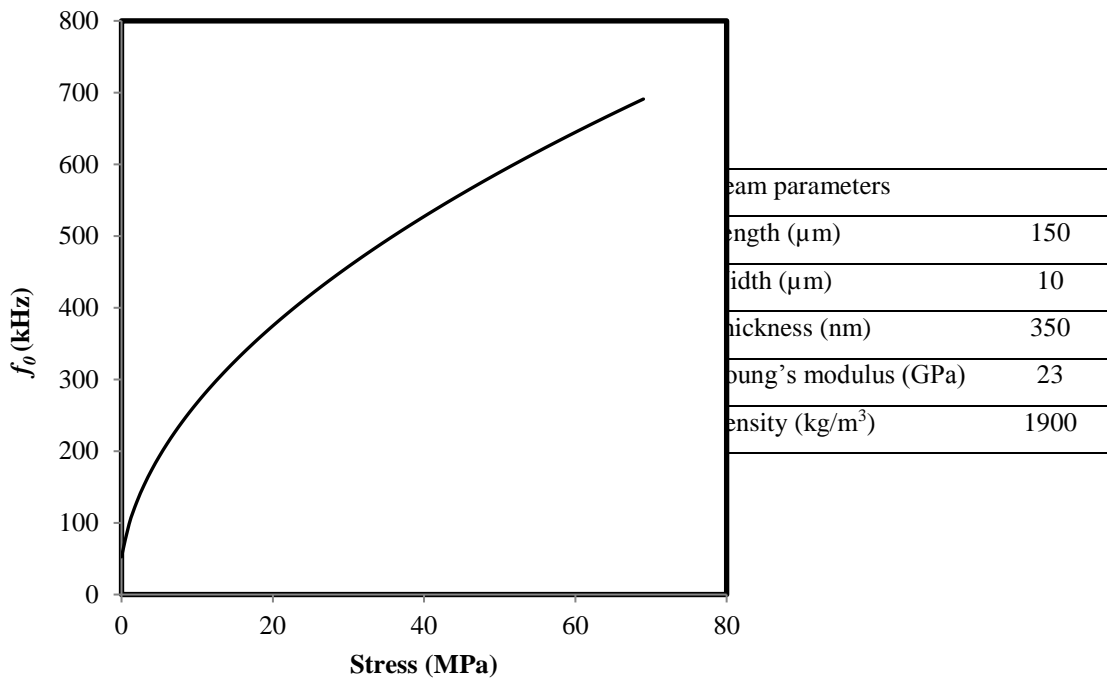
Figure 5.4. Graph showing the theoretical variation of the fundamental natural frequency of a doubly-clamped beam with applied stress. A summary of the beam properties is provided in the inset table.

5.2.3 Changing the natural frequency by changing the DC bias.

The resonators are actuated electrically, with a potential difference V applied between the beam and the substrate. The electrostatic force F_e applied to the cantilever is depicted in Figure 5.5. This force can be calculated using Equation 5.10 [26]:

$$F_e = -\frac{V^2}{2}\frac{\partial C}{\partial r} \approx -\frac{V^2 C_0}{2r}\left[1+2\left(\frac{x}{r}\right)\right] \tag{5.10}$$

where C is the effective capacitance between the resonator area and the underlying substrate at a separation distance r and x is the deflection caused by the electrostatic force. C_0 is the capacitance at zero displacement.
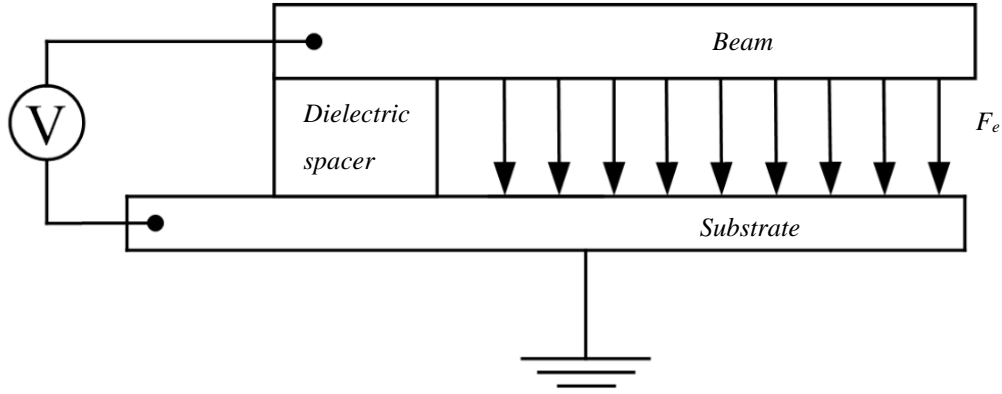
Figure 5.5. Schematic showing a cantilever subject to an electrostatic force.

V is comprised of DC and AC components and thus V^2 is equal to:

$$V^2 = (V_{DC} + V_{ac}\cos(\omega t))^2 = V_{DC}^2 + \frac{1}{2}V_{ac}^2 + \frac{1}{2}V_{ac}^2\cos(2\omega t) + 2V_{DC}V_{ac}\cos(\omega t) \qquad (5.11)$$

Inserting V^2 into Equation 5.10 gives:

$$F_e = -\frac{1}{2}\frac{\partial C}{\partial r}\left(V_{DC}^2 + \frac{1}{2}V_{ac}^2 + \frac{1}{2}V_{ac}^2\cos(2\omega t) + 2V_{DC}V_{ac}\cos(\omega t)\right) \qquad (5.12)$$

Equation 5.12 shows that F_e has components at zero frequency, ω and 2ω. However, the aim is to have F_e at ω. This may be achieved if $V_{AC} \ll V_{DC}$ thus, removing the terms with no dependence on V_{DC}.

$$F_e \approx -\frac{1}{2}\frac{\partial C}{\partial r}\left(V_{DC}^2 + 2V_{DC}V_{ac}\cos(\omega t)\right) \qquad (5.13)$$

and inserting this value of V^2 into Equation 5.10 yields:

$$F_e \approx -\frac{C_0}{2r}\left[1 + 2\left(\frac{x}{r}\right)\right]V^2 \approx -\frac{C_0 V_{DC}^2}{2r} - \frac{C_0 V_{DC}V_{ac}}{r}\cos\omega t - \frac{C_0 V_{DC}^2 \cdot x}{r^2} - \frac{2C_0 V_{DC}V_{ac} \cdot x}{r^2}\cos\omega t$$

$$(5.14)$$

Using Hooke's law $F = k \cdot x$, an electrostatic spring constant k_e may be calculated. These are the third and fourth terms, since these vary with the beam displacement x. However, if $V_{AC} \ll V_{DC}$ then the third term dominates over the fourth term. Thus:

$$k_e \approx -\frac{C_0 V_{DC}^2}{r^2} \qquad (5.15)$$

The electrostatic spring constant works in opposition to the restoring force of the beam mechanical spring constant. This enables the resonant frequency to be tuned by changing the electrostatic spring according to Equation 5.16 [26]:

$$\omega = \omega_0 \sqrt{1 - \frac{k_e}{k_m}} \tag{5.16}$$

5.2.4 Simulation of nanographite resonators

In Equation 5.3, the fundamental natural frequency of an ideal cantilever beam can be calculated. This may be used to compare the experimental results with theory. However, in the fabricated structures, there are two deviations from the ideal model:

1) There is an undercut of around 25 to 30 µm, as shown in Figure 5.6 (this has been measured by SEM and is also visible in optical microscopy). In previous studies this type of undercut has been shown to add an 'effective length' Δl to the device, lowering the resonant frequency below the nominal value [154] according to Equation 5.17 and 5.18 respectively. This added length is due to the fact that the undercut section is compliant, compared with a fully-fixed anchor. Δl is not equal to the length of the undercut, however.

2) In addition, a stress gradient σ_{grad} of 142 MPa / µm exists within the film, which causes curvature in cantilevers (Equation 5.8). The deflection of the cantilever changes the mass distribution of the cantilever, which may alter the natural frequency compared to a straight cantilever off the same dimension.

$$f = \frac{1}{2\pi} \left(\frac{1.875}{l + \Delta l} \right)^2 \sqrt{\frac{EI}{\rho A}} \tag{5.17}$$

$$f = \left(1.03 \frac{h}{(l + \Delta l)^2} \sqrt{\frac{E}{\rho}} \right) \sqrt{1 + \frac{\sigma(l + 2\Delta l)^2}{3.4 E h^2}} \tag{5.18}$$
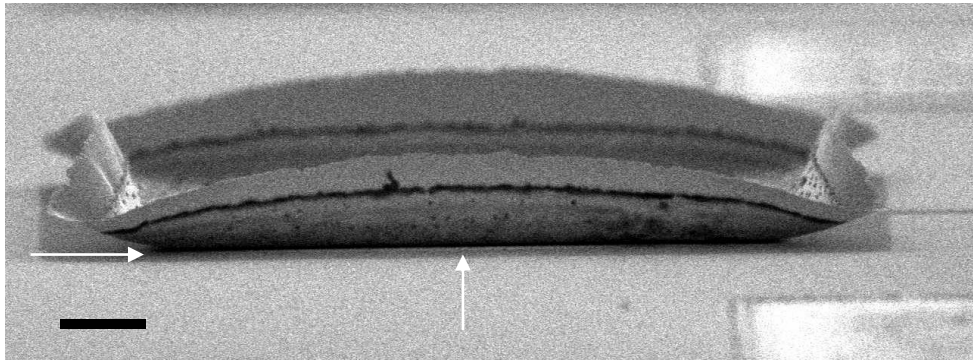
Figure 5.6. High angle SEM image of the anchor of a broken beam device, showing the undercut of around 25 µm, caused by over-etching the SiO₂ layer. Scale bar is 20 µm.
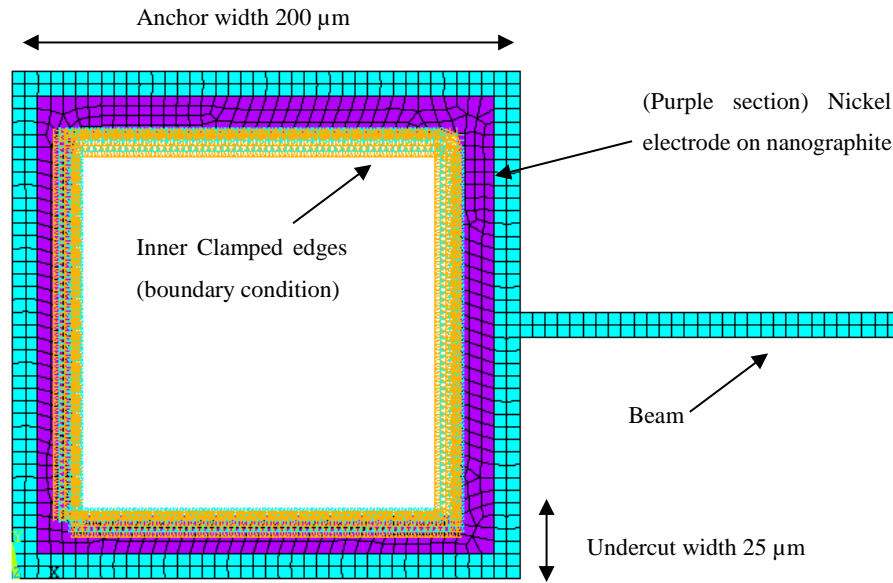
Figure 5.7. Meshed finite element model of a 150 µm cantilever beam.

The average compressive stress of the nanographite was obtained by measuring the wafer bow before and after deposition of the nanographite (this was done in Chapter 4) as 436 MPa. The material was modeled using shell elements (ANSYS SHELL281) with 5 layers of equal thickness defined (the total thickness was 350 nm). A linear variation in coefficient of thermal expansion *CTE* was applied to each layer to create a differential expansion through the thickness, and strain ε was applied by applying a temperature increase *ΔT* where $\varepsilon = \Delta T \cdot CTE$. The stress gradient is - 142 MPa / µm, which was measured from the curvature of cantilever beams. Assuming a linear gradient of stress through the film, the stress level of each layer is shown in Figure 5.8.
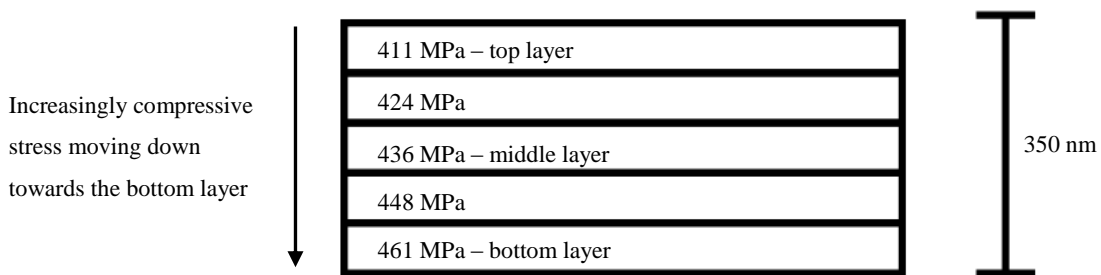
Figure 5.8. Schematic of the stress gradient through the thickness of the film.

I performed FE simulations to take account of these two deviations. A summary of the model parameters is made in Table 5.1. Figure 5.7 shows the meshed FE model. The simulations and analytical calculations are summarised as:

- Analytical result: Cantilever analytical model using Equation 5.3.

78

- Simulation A: FE simulation of ideal cantilever beam, with no stress gradient and no undercut.
- Simulation B: FE simulation of cantilever beam with the presence of a stress gradient but no undercut.
- Simulation C: FE simulation of cantilever beam with the presence of a stress gradient and undercut.

The comparison of the results of the four sets of results are made in Table 5.2. The value of $\varDelta l$ was extracted by using the value of f_0 as calculated by the simulation C, and equating it to Equation 5.17. All the parameters are known except for the value of $\varDelta l$.

The boundary conditions of the simulation are that the edge of the undercut section, where the overhang is adhered to the substrate, is fully constrained. As a result of the boundary conditions, a large section of the model (the central square under the electrode, where the material is fully clamped to the substrate) is redundant and removed from the model. This reduction in the size of the model represents a simplification of the structure, thereby reducing the computational expense, but maintains the governing boundary conditions of the real structure.

The FE analysis solver takes two steps: (1) a nonlinear static analysis is used to obtain the deflection and stress caused by the gradient, followed by (2) a modal analysis of the stressed structure to obtain the vibration modes and frequencies. Figure 5.9 (A) shows a model after being subject to nonlinear static defection caused by the thermal stress, in comparison to the deflection of the actual device.

Beam Width (µm)	10
Beam length (µm)	50, 75, 100
Anchor width (µm)	200
Density (kg/m^3)	1900
Nanographite thickness (nm)	350
Electrode width/length (µm)	170
Undercut (µm)	25
Nanographite E (GPa)	23
Nanographite average stress (MPa)	- 436
Nanographite stress gradient (MPa/µm)	- 142
Nickel E (GPa) [155]	200

Table 5.1. Summary of the input parameters used for the FE model.

Beam length (μm)	Analytical f_0 (kHz)	Simulation A - ideal beam f_0 (kHz)	Simulation B - curved beam f_0 (kHz)	Simulation C – full deflection f_0 (kHz)
75	34.97	35.18	33.48	30.85
100	19.67	19.76	19.00	17.86
150	8.74	8.77	8.46	8.10

Table 5.2 Comparison of f_0 as calculated and simulated using a range of models, for beams of length 75 to 150 μm.

Figure 5.10 shows the plot comparing the results of the ideal analytical result and simulated result. Simulation C shows a systematic decrease in the natural frequency caused by the undercut. Simulation B shows a slight decrease in f_o over simulation A, the effect of the stress gradient and undercut may be lumped together as an added length Δl (as in Equation 5.17) as shown in Figure 5.10. This is similar to the result obtained by Gavan *et al.* [154] with the measurement of silicon nitride cantilevers. The undercut region is not a perfectly 'clamped' structure as modeled in theory. This overhang is free to deflect, which means the nominal length l is lengthened by amount Δl. The value of Δl has been calculated by fitting the results of f_0 from Simulation C to f_0 as calculated in Equation 5.3. Thus, for these structures, which were all fabricated with a 25 μm undercut, the added effective length Δl is 4.85 μm. Figure 5.10 plots the f_0 as calculated by (1) Equation 5.3, using nominal length l, (2) the results of Simulation C and (3) using Equation 5.18 where $\Delta l = 4.85$ μm. The result of using Equation 5.17 with Δl shows a good approximation to Simulation C.

A

B
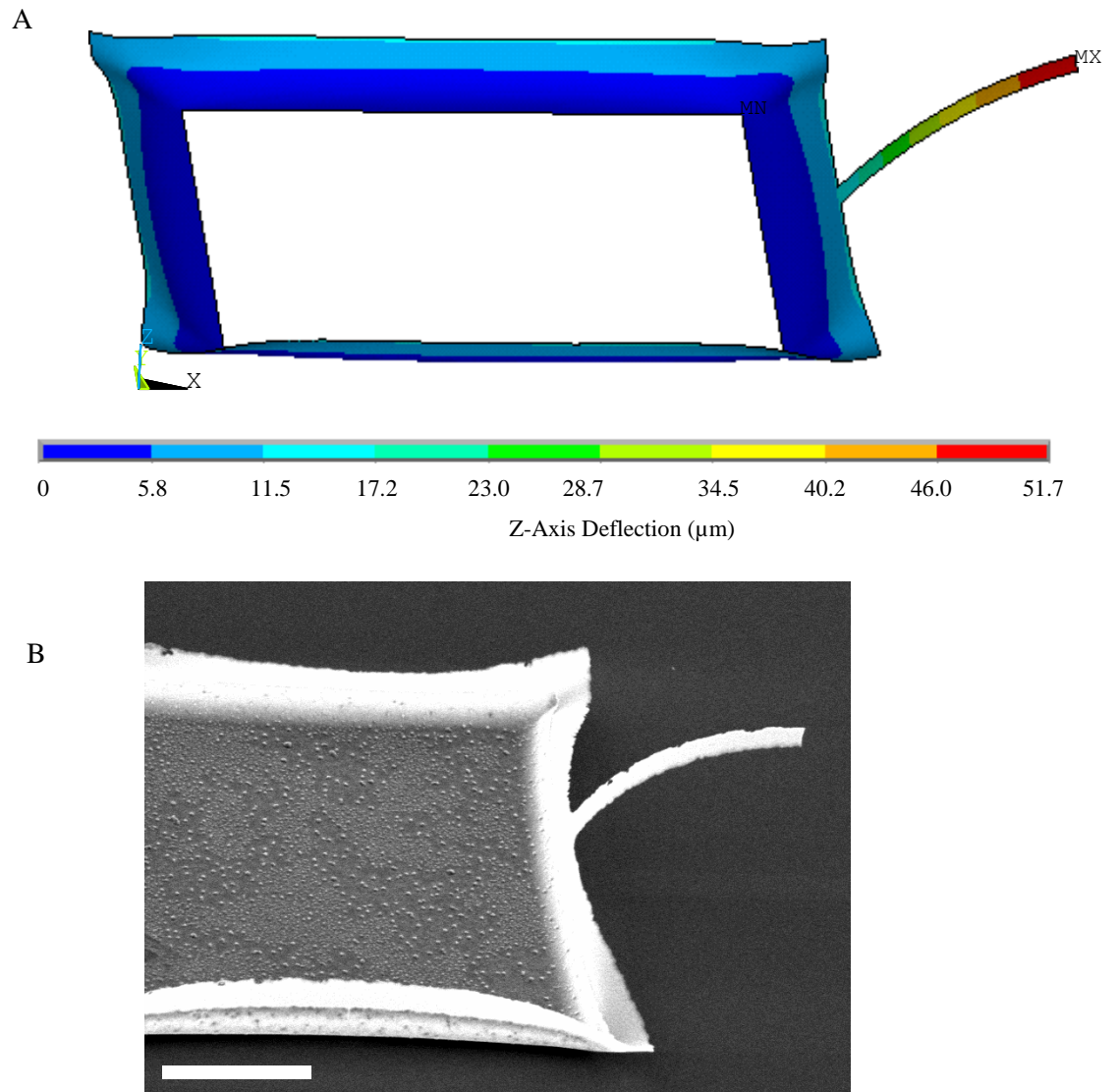
Figure 5.9. (A) Comparison of the deflection of the Simulation C of a 75 µm cantilever resonator. (B) SEM image of corresponding real cantilever structure with a 50 µm scale bar.
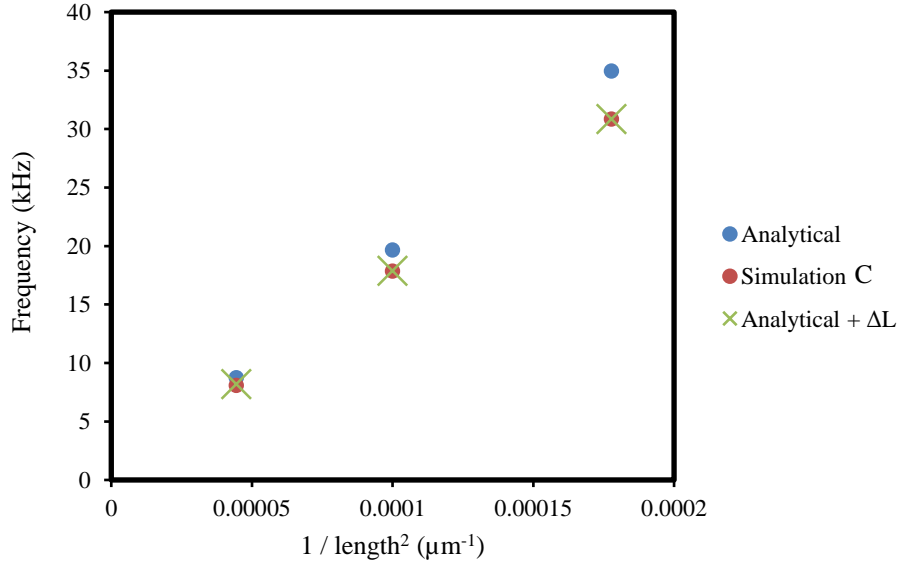
Figure 5.10. Comparison of Simulation C and analytical values of cantilever beams, taking account of the undercut.

5.3 Results

The fabricated structures were characterised as prototype resonators by measuring their natural frequency and Q. The structures were actuated electrostatically and the vibration modes measured using LDV. The majority of the results were performed in ambient conditions, and low values of Q were measured as the motion was highly damped by the surrounding air. One sample was wire-bonded and actuated under vacuum conditions, enabling measurement of the Q when the structure is not dominated by viscous damping.

5.3.1 Resonance of cantilever structures

11 resonator structures, from 4 separate chips were measured. The fundamental mode for a cantilever is a 'flapping mode', shown in the schematic in Figure 5.11. The measurement of the fundamental mode was confirmed as the amplitude was at maximum when the laser location was placed at any location along the beam length. Figure 5.12 shows a resonance spectrum of the first peak for a 150 μm long cantilever, with a Lorentzian curve fitted to the data, from which the Q of 5.6 and f_0 of 27.06 kHz is found. The low value of Q is due to the dominant effect of viscous damping under the ambient conditions.
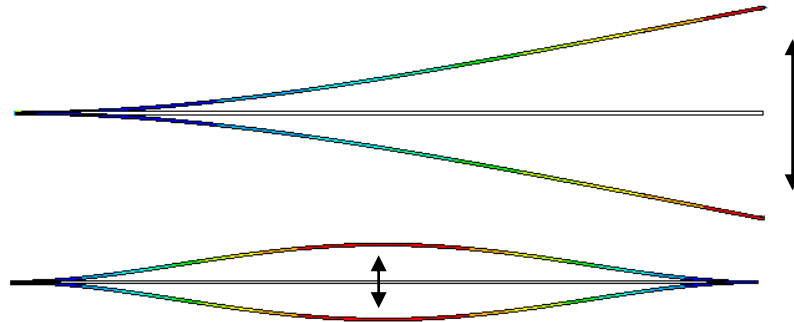
Figure 5.11. Depiction of the fundamental vibration modes of cantilever and doubly-clamped beams.
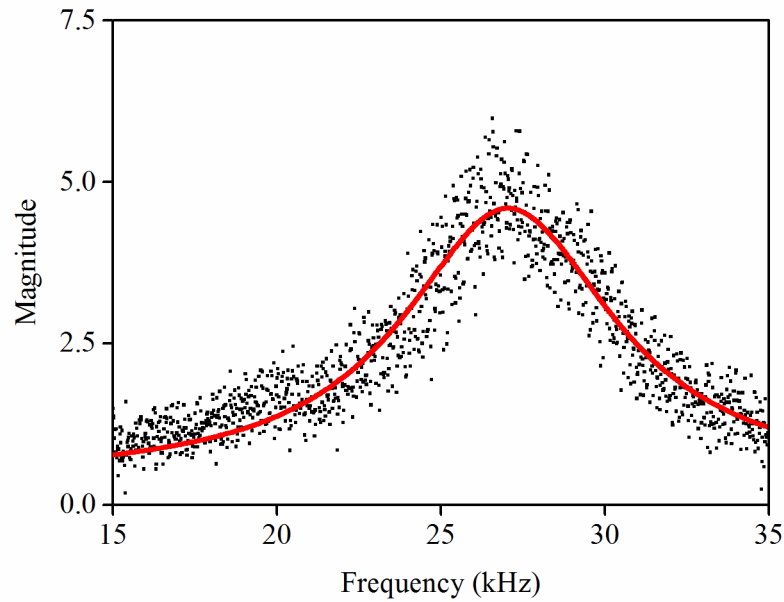
Figure 5.12. A plot showing the frequency response of the fundamental vibration mode of a 75 µm long cantilever beam. The red line is a fitted Lorentzian curve.

Cantilevers of lengths between 75 to 150 µm were measured, with frequencies in the range of 5.3 to 27.0 kHz and Q of around 5 to 10. The thickness of the nanographite on each of the 4 chips was measured by stylus profilometry, as between 270 and 340 nm. The theoretical dashed line shown in Figure 5.13 shows f_0 against t / l^2 as calculated by Equation 5.6, using the value of $E = 23$ GPa as obtained in the previous Chapter. The results give close agreement, within experimental uncertainties due to fabrication variations in undercut length, length, and thickness. Outlying results may be accounted for small thickness variations in the chip after etching. The thickness of the layer on each chip was measured using profilometry. However, due to the large deflection of each device, the thickness of another artifact on the chip (a section of writing) was measured, not the beam itself. The thickness of this artifact was measured three times per chip. There may be a slight variation in the

thickness of the artifact and the beam which leads to a slight disagreement in the results. As a result, the main error associated with the results shown in Figure 5.13 are of beam geometry and the error bars are horizontal as a result.
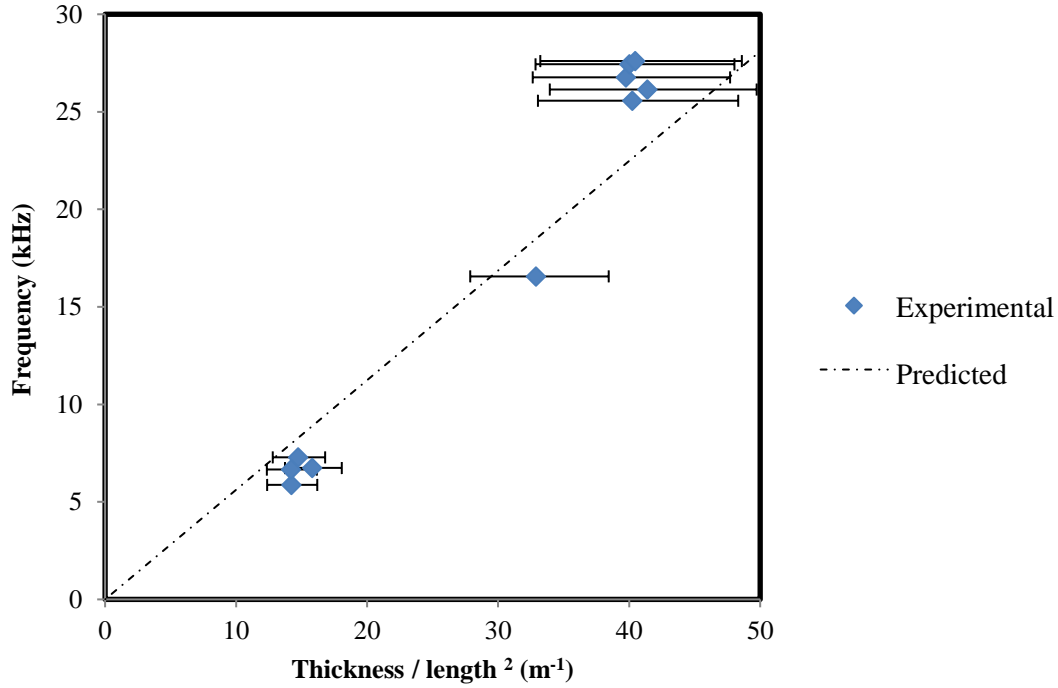
Figure 5.13. Frequency of the fundamental resonance mode of cantilever devices, plotted against thickness divided by length^2 and compared with the theoretical value of f_0 using the value of 23 GPa.

5.3.2 Resonance of doubly-clamped beam structures

14 doubly-clamped beams were characterised in the same way as the cantilevers. Whilst the stress of a cantilever beam is zero, these doubly-clamped beams were under a tensile stress. This is because for doubly-clamped beams, the built-in stress cannot be released from the structure and this affects the bending stiffness. The stress in these doubly-clamped beams arises from the geometric effect of the anchors, which lift up and impart a tensile strain to the beam section.

Figure 5.14 shows the fundamental frequency of 14 doubly-clamped beams, plotted against t/l^2. The structures have nominal lengths and natural frequencies of 566 to 640 kHz (75 µm beams), 414 to 474 kHz (100 µm beams) and 245 to 267 kHz (150 µm beams). The values of Q for these structures lie around 20 to 30 under ambient conditions. The plot in Figure 5.14 includes a comparison of the experimental results to the analytical results using Equation 5.8. In the analytical results, the length is varied from 75 to 150 µm, with a set thickness of 350 nm and stress values of 10 and 20 MPa. Small variations in the undercut of devices between different chips may cause changes in the stress and effective length of the structures, which can explain some of the small deviations from a single

value of stress. The difference in undercut is due to the inhomogeneity of HF vapour etching using the home-built setup.
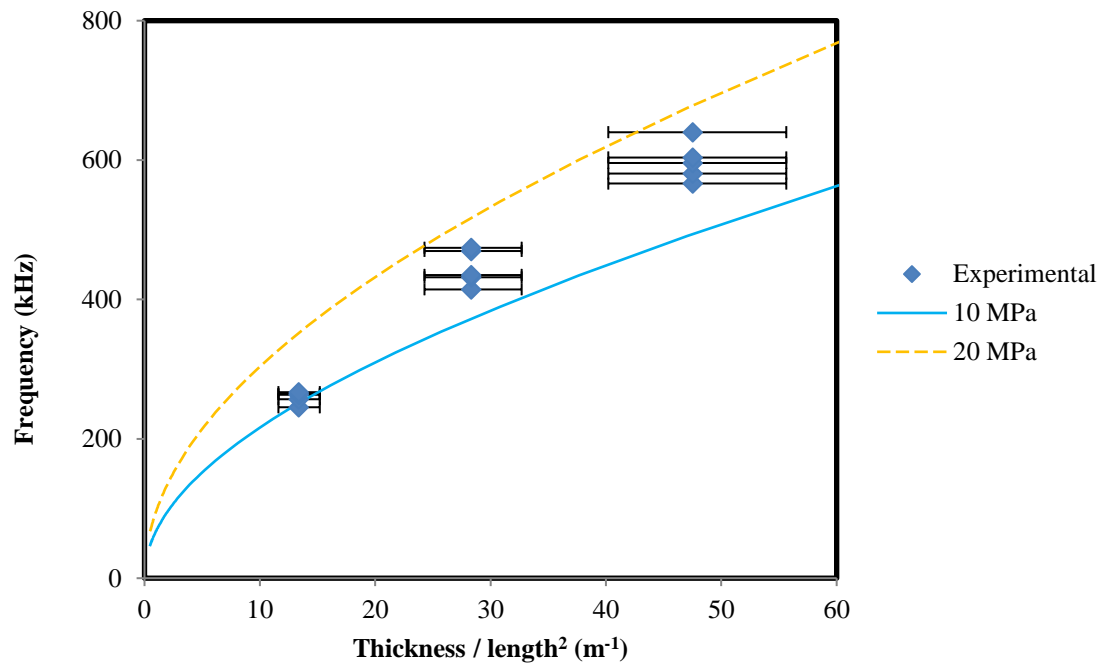
Figure 5.14. Frequency of the fundamental resonance mode of doubly-clamped beam devices, plotted against thickness divided by length^2 and compared with the theoretical line of resonance with applied stress of 10 to 20 MPa.

One device was wire bonded, and actuated under vacuum conditions. Figure 5.15 shows the resonance peak of a 150 µm device under vacuum conditions (30 mTorr). The value of Q under vacuum was > 1819, compared with > 27 at ambient pressure. As expected, Q for beams under ambient pressure is dominated by the external viscous damping.
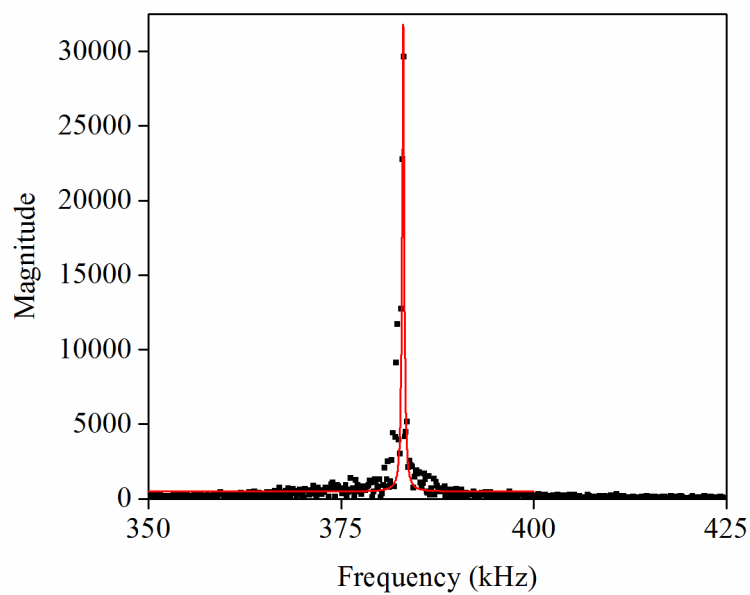
Figure 5.15. A plot showing the frequency response of the fundamental vibration mode of a 100 µm long doubly-clamped beam, under 30 mTorr vacuum.

85

5.3.3 Tuning the natural frequency with DC bias

For many resonator devices, the ability to control the resonant frequency is very useful, as it allows tuning to a set frequency. For these devices, tuning can be achieved by applying a varying DC bias between the beam and substrate, according to Equations 5.14 - 5.15. This creates an electrostatic 'spring' which opposes the spring constant of the beam itself, and lowers the natural frequency. Figure 5.16 shows the variation in the frequency response of a doubly-clamped beam, actuated under vacuum conditions, with different values of DC bias.
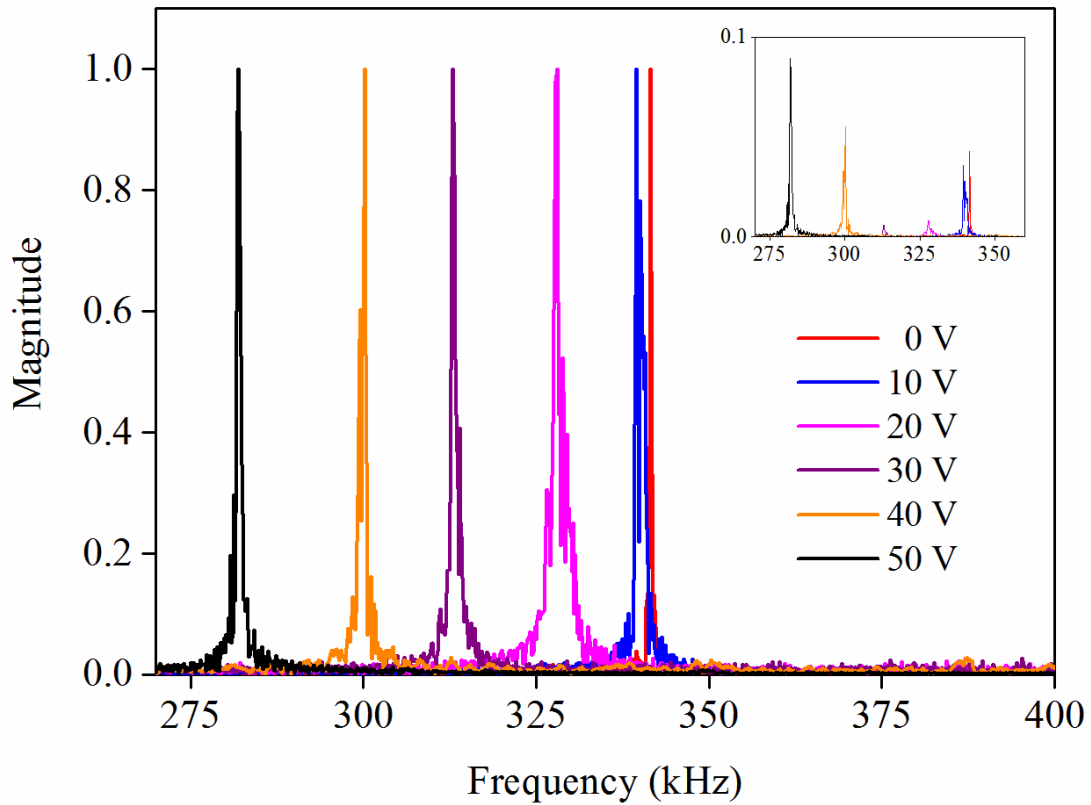
Figure 5.16. A plot showing the varying frequency response for one doubly-clamped beam with an increasing DC bias applied between the beam (top electrode) and substrate (bottom electrode). The graph shows velocities of each measurement equalised to the same value for ease of viewing. The inset graph shows the magnitude without equalisation.

Figure 5.17 shows the variation in the fundamental frequency for the doubly-clamped beam actuated under vacuum conditions, plotted against the voltage squared. According to Equation 5.17 this is a linear relationship for small deflections. It is clear that the f_0 vs. V^2 is linear up until a point of ~ 900 V^2 (30 V). Past this value of 30 V, the relationship deviates away from linearity and starts to become stiffer with increasing voltage. This is due to the high DC bias causing a relatively higher

deflection of the beam. This high deflection causes the beam to bend outside of its linear regime, and becomes increasingly stiff, and the relationship in Equation 5.14 - 5.15 does not hold.
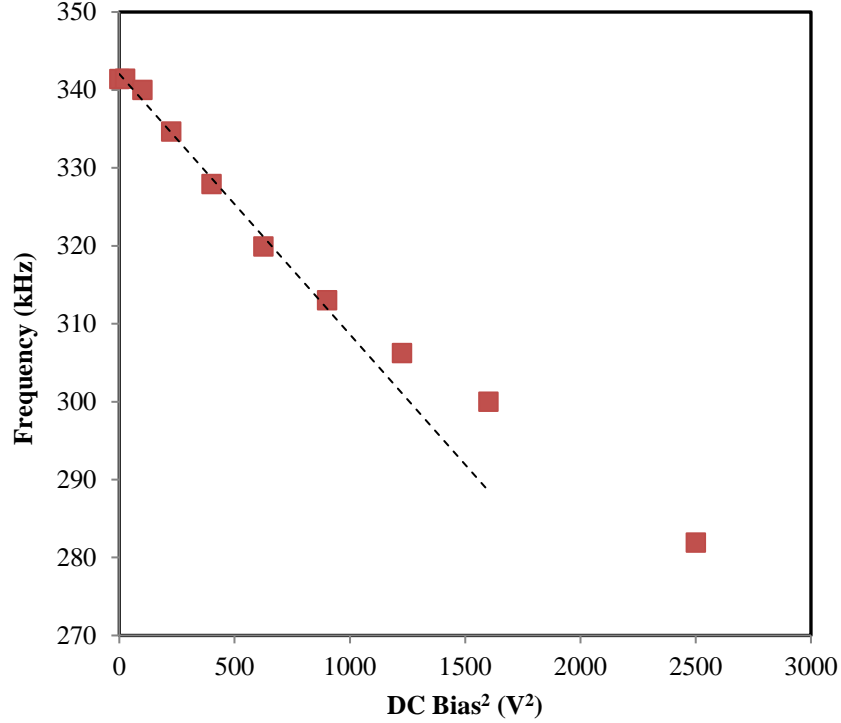
Figure 5.17. A plot of the natural frequency of a doubly-clamped beam against the applied V_{DC}^2. The dotted line is fitted for the results up to 900 V^2.

5.4 Discussion of results

Here, I showed the performance of MEMS resonators made from nanographite. The devices were fabricated using standard microfabrication and MEMS-type processes. A Q value of up to 1800 was measured, and highlighted a novel type of process flow where the undercut can be used to effectively change the stress state of the device.

I note that, only a single device has been measured under vacuum conditions and no trend in the variation of Q against the length or volume of the device has been obtained. The low number of devices tested under vacuum conditions was due to the difficulty in bonding to the nickel electrodes. The single measured device at vacuum pressure has a reasonable value of Q, this is likely to be dominated by a combination of intrinsic losses within the material [156] and losses through the anchors [157]. Nanocrystalline materials typically have intrinsic material losses due to the presence of defects near the surface of the material [158], though this needs to be studied further in the case of nanographite. Table 5.3 shows a comparison of the Q and frequency range of this work with comparable carbon-based resonators.

The devices I have fabricated are from a material which is highly compressive (-436 MPa), but I have demonstrated a method by which the beam section is under an effective tensile stress of 10 to 20 MPa, calculated by fitting the experimental results to Equation 5.18 (a model of a doubly-clamped beam under tensile stress) as shown in Figure 5.14. This was achieved by the geometric effect of undercutting the structure anchors. This is a simple way to obtain tensile-stressed structures from a compressively-stressed material. For this application, the simple method of fabrication enabled the effective stiffness and natural frequency to be increased by means of the application of tensile stress. It is noted that the deformation of the beam lifted the beam around 10 µm away from the ground electrode. This reduces the likelihood of stiction during fabrication, as the beam is pulled away from the substrate. However, in the case of a resonator with capacitive feedback such as the doubly clamped beam in research by Wiser *et al.* [159], the increase in distance between beam and ground electrode would notably reduce the capacitance, and thus reduce the motional current which is used to sense motion. The undercut is controllable, using the homebuilt HF vapour etching setup to within ± 5 µm.

The method of inducing tensile stress through undercutting the anchors could have potential applications for different types of MEMS devices. For example, many doubly-clamped beam structures fabricated from carbon thin films in the literature appear to suffer from buckling [68,71,82] which greatly increases unreliability and irreproducibility. Furthermore, the stiffness of an out-of-plane MEMS or NEMS switching device could be tuned using this geometric method, thereby altering the pull-in voltage. For example, a material of compressive stress could be designed to be fabricate a 'slack' beam (as opposed to the 'pulled tight' example in this work) which would have a low effective stress (and stiffness), and therefore a low pull-in voltage for switching applications.

Material	Frequency range	Q (Vacuum)	Growth	Actuation
Nanocrystalline diamond [39]	17 to 66 MHz	600 to 2400	MPCVD	Magnetomotive
Nanocrystalline diamond [78]	6 to 30 MHz	2400 to 3500	MPCVD	Piezoelectric
Nanocrystalline diamond [156]	14 to 157 MHz	~3500	MPCVD	Piezoelectric
Diamond-like carbon [82]	192 MHz	~ 1400	PVD	Electrostatic
Single – multilayer graphene (single crystal) [62]	1 to 170 MHz	20 to 850	Exfoliation from graphite	Optical / Electrostatic
Few-layer graphene [71]	3 to 50 MHz	50 to 700	Annealing SiC	Optical
This work	**245 to 640 kHz**	**1800**	**PECVD**	**Electrostatic**

Table 5.3. Comparison of the behaviour of carbon doubly-clamped beam flexural resonators.

Graphitic materials such as few layer graphene [9], highly-ordered pyrolytic graphite [160] and related materials such as DLC [82] and nanodiamond [156] have been sought after as a material for MEMS and NEMS. The main material properties of interest for these materials are as summarised below:

- High value of modulus, for high-frequency resonator applications.
- Low value of thickness/mass for graphene which enables potentially high mass sensitivity and also low pull-in voltage switches.
- High chemical and temperature stability for harsh environment sensing.

Nanographite has a low value of Young's modulus which generally would not be sought-after for high frequency resonators, and this suggests it may be more suited for low-powered MEMS and NEMS switching applications (where a low stiffness and subsequent pull-in voltage are required). However, I have shown here a method to alter the stress-state of the structure, and thus giving a much higher overall stiffness, thereby, to some degree, overcoming the low value of Young's modulus to give the beam a high effective stiffness. The scalability and compatibility of the PECVD synthesis route means that nanographite may be much more easily and cheaply produced compared with other related materials, such as thin film graphite or graphene produced by thermal CVD [17,19], which

shows it may be a promising graphitic thin film for upscaling to industrial applications. As such, nanographite is considered a potentially useful material for MEMS applications, in particular for harsh environment sensing and for switching applications.

My aim here and in the previous Chapter was to present examples for fabricating nanographite MEMS and characterising the key mechanical property of the Young's modulus. This work should better enable the future design of nanographite MEMS and NEMS, going forward towards real life applications.

5.5 Summary and conclusions

Here in this Chapter, I have presented the characterisation of MEMS nanographite resonators which were fabricated using standard micromachining technology. I fabricated prototype resonators to show the feasibility of fabricating MEMS devices from the nanographite thin film and actuated them electrostatically.

Cantilever beams of length 75 to 150 µm were electrostatically actuated and measured using LDV, with natural frequencies between 5.3 to 27 kHz. The undercut of around 25 µm was found to increase the effective length of the beams by just under 5 µm. The natural frequency of the cantilever beams showed that the Young's modulus value of 23 GPa, which was extracted empirically in the previous Chapter, agrees well.

Although the material is under a high compressive stress, I was able to obtain tensile stressed doubly-clamped beams. The high undercut, coupled with the stress gradient in the film acts to lift up the beam anchors, and thereby 'pull' the beam tight. This is a technique which may be of wide-ranging interest, as the literature showed a large number of carbon doubly-clamped devices which undergo buckling [68,71,82].

The wide-area and reproducible synthesis route of nanographite mean that it may be well placed to be scaled up for MEMS and NEMS use, and the results show it is a promising material for NEMS resonators and for NEMS switches. This work provides technology to pave the road towards scalable NEMS based on graphitic films, thereby opening up technologies for highly sensitive sensors.

6. Investigation of the permeance of gas through nanographite membranes

6.1 Introduction

In the previous Chapter, nanographite was used as a MEMS resonator. The primary aims of that work were to demonstrate the use of the material in a MEMS-type application and to present an example of microfabricating a device using a highly stressed film. In this following work, the gas permeation behaviour of freestanding nanographite membranes is investigated. This work was undertaken to consider two questions:

1. Can the permeability of a thin nanographite membrane be *high* enough and show sufficient selectivity between gases such that it can be used as a molecular sieve? The basis for a molecular sieve membrane is that the gas of interest should have a high flux through the membrane, and the rejected gas should have a low flux.

2. Can the permeability of a relatively thick nanographite membrane be *low* enough such that it can be used as a membrane based pressure sensor? The sensing basis for a membrane-based pressure sensor is that a differential pressure applied across the membrane will cause a deflection, which may be measured piezoresistively or capacitively, for example. A material which is so porous whereby the level of escaping gases will not enable a steady deflection under pressure is not a viable material.

These questions cannot be simply answered using analytical modelling methods, since the permeability of a membrane to gases is highly dependent on the grain structure and pore size (d_p). There has currently been no study on d_p in nanographite and this is not simple to measure. In this Chapter, the flux of various gases through nanographite membranes was measured, in order to help answer the two above questions.

Some of the main requirements for materials used for gas filtration and separation are:

- High flux of a certain 'analyte' gas and low flux of the 'reject' gas. The ratio of the fluxes of these two gases (α) is known as the separation factor or selectivity.
- Suitability for large area membrane development to be scaled for industrial applications.
- High chemical and temperature resistance.

The typical applications for gas separations are the purification of H_2 [161] from CO_2, and of He from other gases [98]. Recent research has shown high performance of graphene-based materials for such applications, whereby the intrinsic defects within the crystal structure of graphene-oxide [16]

porated graphene [12] and polycrystalline graphene [116] have been shown as having highly selective gas permeation characteristics. In these materials, a relatively low density of defects in the lattice led to modest permeance of H_2 for the relative thickness [16]. Nanographite has a crystal structure related to these materials and may have similar sieving qualities which is of interest to improve the performance of membrane molecular sieves.

As a secondary aim, the work in this Chapter demonstrates another important property of nanographite which strongly links to the work of nanographite MEMS resonators. The use of membrane structures as pressure sensors is well established. There is a particular requirement for cheaper, high temperature-resistant sensors for high temperature applications [159] of which nanographite is a good candidate due to its high temperature resistance and simple and scalable synthesis route. The work in this Chapter helps towards furthering this application by:

1. Presenting the fabrication of nanographite membranes on a suitable high temperature substrate such as fused-silica.
2. Testing the permeation of the nanographite film. Other carbon films are susceptible to tears and defects [14] which mean they cannot currently realistically be used in real-life applications.

Here, results for the gas permeation through nanographite are presented. A mass spectrometry system using UHV equipment was constructed and used to evaluate the flow of gases through the material.

6.2 Behaviour of gases flowing through membranes.

To provide a basic description, a permeable membrane is a thin sheet which is porous to gases by means of molecular diffusion. The permeation may be selective to different molecules, such that the flow rate of one gas at a given pressure and temperature will be higher than that of a different gas under the same conditions.

The mechanism of permeation depends on the material properties and here the relevant theory to the gas diffusion and separation processes through thin porous membranes is presented.

6.2.1 Basic concept of diffusion through membranes.

The molecular flux J through a membrane of thickness L is the number of molecules which pass through a unit area, per unit time. The flux is proportional to the concentration gradient, ΔG, between

the two sides of the membrane, which can be expressed as in Equation 6.1 [101] and is depicted in Figure 6.1.

$$J = -D \frac{dG}{dx}$$ (6.1)

Where D is the diffusivity constant, G is the concentration and x is the position across the membrane. The flux can be approximated as Equation 6.2 by assuming a linear concentration gradient through the membrane where the up and down-stream concentrations are G_1 and G_2 respectively.
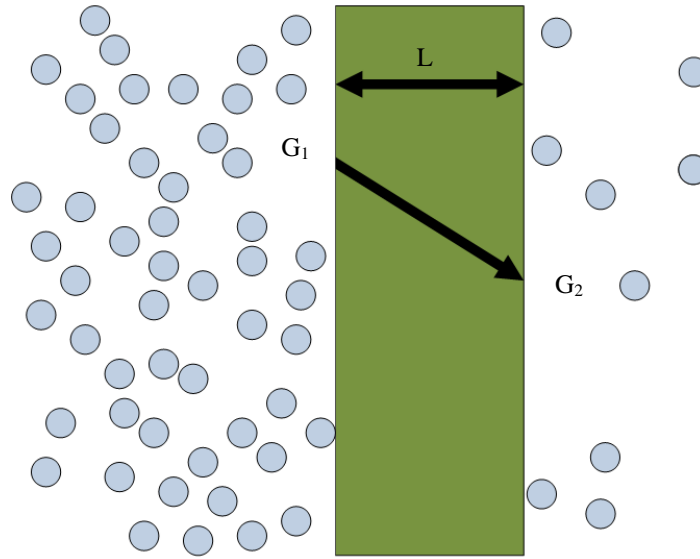
Figure 6.1 Schematic showing the decrease in concentration of a gas, across two sides of a permeable membrane.

$$J = D \frac{G_1 - G_2}{L}$$ (6.2)

The permeance B, is the area a and pressure p normalised flux and may be calculated as [101]:

$$B = \frac{J}{ap}$$ (6.3)

The permeance is clearly related to the external conditions (G_1 and G_2) of the membrane, and its thickness L. The *intrinsic material* characteristics are all 'contained' within D. The mechanism by which molecules travel through a porous membrane is largely controlled by the relative size of the molecule k_d (kinetic diameter) to d_p. The three main mechanisms of molecular permeation are shown schematically in Figure 6.2.

In this regime molecules are in the gas phase and are filtered by mass according to the length of their differing mean free paths.

Here molecules are adsorbed to the pore walls and hop, in a vibrational state, between adsorption sites to move through the pore. Filtering occurs as molecules have different adsorption energies with the pore material.

Gas translational diffusion is similar to Knudsen diffusion, but here the pore size is smaller, and the molecules must (1) overcome an energy barrier imposed by the pore, and then (2) flow in the gas translation regime.

Figure 6.2. Schematic and summary of the three discussed mechanisms of gas permeation through porous membranes.

6.2.2 Knudsen diffusion

Here, a description of the relevant basic theory regarding the mechanisms of gas flow through porous membranes is presented [162,163]. This provides a framework for the analysis of the measurements of nanographite membranes, obtained from the permeation experiment described in Chapter 3.

Knudsen diffusion occurs when the diameter of the pore is considerably smaller than the mean free path of the molecule but greater than the size of the molecule. The size of a molecule may be approximated as its kinetic diameter k_d. This is the distance at which the inter-particle potential is zero, if the molecule is modelled as a sphere [164,165].

In membranes where Knudsen diffusion dominates, each molecule is much more likely to collide with the pore walls than with other gas molecules. During a collision with the pore wall, the molecule is adsorbed and desorbed. The differing mean free path of molecules of mass M leads to a differing

average velocity through the pore, thus giving differing flux. The diffusion constant (D_k) of permeation for a membrane dominated by Knudsen diffusion is [163]:

$$D_k = \frac{d_p}{3} \sqrt{\frac{8RT}{\pi M}} \tag{6.4}$$

where d_p, is the pore size, R is the gas constant and T is the temperature. Thus, the selectivity α (the ratio of D for each gas) for two gases comprising molecules of mass M_1 and M_2 is the square root of the ratio of the masses of the molecules:

$$\alpha_{knudsen} = \sqrt{\frac{M_1}{M_2}} \tag{6.5}$$

6.2.3 Surface diffusion

In a membrane made of a material with pores which are closer to the size of the molecular diameter of the diffusing species, the mechanism of mass transport becomes different from purely Knudsen diffusion. This is the case of surface-dominated flow, where the probability and frequency of collisions between the molecule and pore walls increases, and is therefore more likely to adsorb. In surface diffusion, the transport of molecules takes place by jumping between adsorption sites. The diffusion coefficient D_s of molecules in this phase may be expressed as [166]:

$$D_s = \frac{1}{z} \tau^2 \psi \exp\left(-\frac{E_s}{RT}\right) \tag{6.6}$$

where z is a constriction of probability factor, τ is the diffusional length which is the average distance between jumps (Equation 6.7 [167]), ψ is the jump frequency and E_S is the activation energy for surface diffusion.

$$\tau = \frac{k_B T}{\sqrt{2} \pi \sigma_{ii}^2 p} \tag{6.7}$$

where k_B is the Boltzmann constant and σ_{ii} is the collision diameter of the molecule (the collision diameter is the intermolecular distance between two molecules where the potential energy is zero [168]) and p is the pressure.

6.2.4 Gas translational diffusion

At higher temperatures, and with molecules that adsorb less easily, the amount of adsorbed molecules is less than in the surface diffusion. In gas translational (GT) diffusion, there is an activated step where the molecule must overcome an energy barrier imposed by restrictions in the pore structure, followed by gas-state diffusion in the Knudsen regime. During the Knudsen diffusion step, there is little potential energy on the molecule from interaction with the pore wall. This is termed 'gas translational', or 'activated Knudsen' diffusion, and has been noted in zeolite [166] and carbon-based membranes [163]. This is an activated process, where the molecules have to overcome an energy

barrier E_{GT} caused by the restrictions of the pore structure. The size of the energy barrier increases with the kinetic diameter of the molecule [162]. Here the diffusion coefficient may be expressed as [163]:

$$D_{GT} = A_{GT} \sqrt{\frac{8RT}{\pi M}} \exp\left(-\frac{E_{GT}}{RT}\right) \tag{6.8}$$

Where A_{GT} is a geometric constant related to the pore size, tortuosity and porosity of the membrane. This is normally inferred by regression of the permeability results [163].

A related permeation mechanism to GT diffusion is known as molecular sieving [162]. The activation energy E_a is related to the ratio of the molecule kinetic diameter to the pore size, whereby larger molecules experience a repulsive force from interaction with the pore walls. The transition from gas translation diffusion to molecular sieving is not sharp, except in molecular sieving the molecule does not freely flow in the gas translational regime, and always under interaction with the pore wall.

6.2.5 Determining the sieving regime

If the process does not show an exponential increase in permeance with temperature, it may be inferred that the dominant mechanism of permeation is Knudsen diffusion. This may also be verified by measuring the permeance of two gases of different molecular weight and checking whether Equation 6.5 holds.

If the permeance of a gas through the membrane shows an exponential change, it may be inferred that one of the activated permeation mechanisms is dominant. The activation energy E_a may be calculated from an Arrhenius plot of the permeance B against the inverse of temperature, as the gradient of this line represents E_a / R. Both surface diffusion and gas translation are activated processes; however the value of the activation energy may be used to determine the mechanism of permeance through the membrane [169]. A negative value of E_a shows that the mechanism of permeation is dominated by surface diffusion. This is because fewer molecules become adsorbed onto the pore walls at higher temperatures, and the number of molecules transported by the surface-diffusion hopping mechanism reduces. A positive value of E_a shows that the mechanism of permeation is dominated by gas translational diffusion, or molecular sieving, as the number of molecules with sufficient energy to overcome the barrier to enter and permeate through the membrane pores increases.

6.3 Results

The description of the UHV gas permeation rig was made in Chapter 3. The apparatus comprises two evacuated chambers separated by a nanographite membrane. One chamber is filled with a pure gas

to pressures of up to 80 Torr. The second chamber is evacuated to ultra-high vacuum conditions, and the flow of analyte gas is measured using a residual-gas-analyser (RGA) type mass spectrometer and calibrated using a total pressure ionisation gauge (IG).

The sample is a suspended nanographite membrane of diameter ~1 mm. The consequences of failure of the membrane during testing were considerable and the resulting sudden spike in pressure into the UHV chamber may cause failure of the RGA and IG ionising filaments. Thus the maximum applied pressure was kept in the 'safe' range of below 80 T to avoid such an outcome.

In Chapter 3, two methods for measuring the gas permeance were detailed, the 'closed volume' method and the 'vacuum' method. These are compared in Section 6.3.4, but all other measurements described excepting these for comparison were made using the closed volume method.

6.3.1 Permeation behaviour with temperature

The flux of He, H_2 and Ne was measured through a nanographite membrane at a range of temperatures from 25 °C to 150 °C. The highest 'safe' pressure of 80 Torr was used throughout, to maximise the absolute flux through the membrane and thus reduce the effect of the absolute errors of background noise. The calculated values of permeance are an average of 5 readings taken at the same pressure.

To measure the variation of gas flux through the membrane at elevated temperatures, the membrane holder and adjacent components were wrapped in heating tape and aluminium foil, to help maintain homogenous heating throughout. A thermocouple was taped to the outer face of the membrane holder using conductive carbon tape and the sample was heated and maintained at temperature for one hour prior to permeation measurement.

Figure 6.3 shows the gas permeation of pure He, Ne and H_2 through a nanographite membrane. For each gas, the permeance increases exponentially with temperature. H_2 and He follow similar trends, and absolute values of permeance. Ne follows a similar exponential trend though with significantly lower absolute values of permeance. The permeance value for He at 150 °C appears to show a leveling-off, though Ne and H_2 show clearer exponential trends over this temperature range.
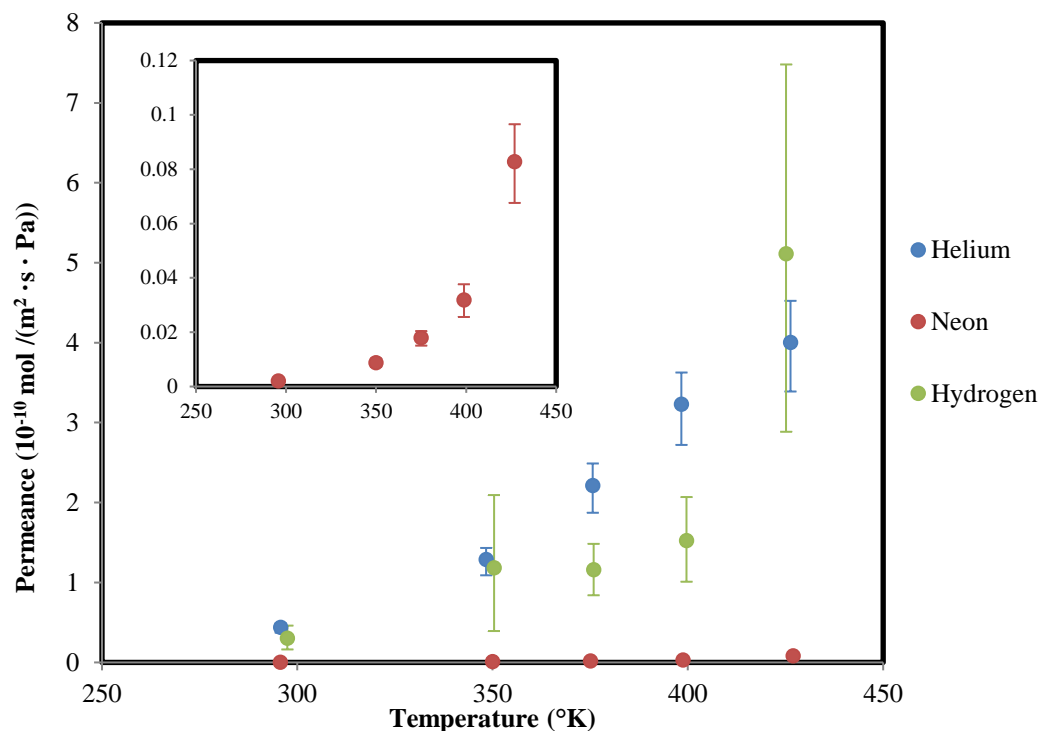
Figure 6.3. Plot showing the permeance of three gases through a membrane as a function of temperature. The inset graph shows the permeance of Ne only, for clarity. The membrane is 350 nm thick and 1.1 mm in diameter.

Figure 6.4 is an Arrhenius plot showing the permeance against the inverse of temperature, which can be used to calculate activation energy as the gradient of the line represents $-E_a/R$ (Table 6.1). The temperature dependence of the permeation shows an activated process for all gases, with the negative slope of the Arrhenius plot indicating that gas translational diffusion dominates the flow.
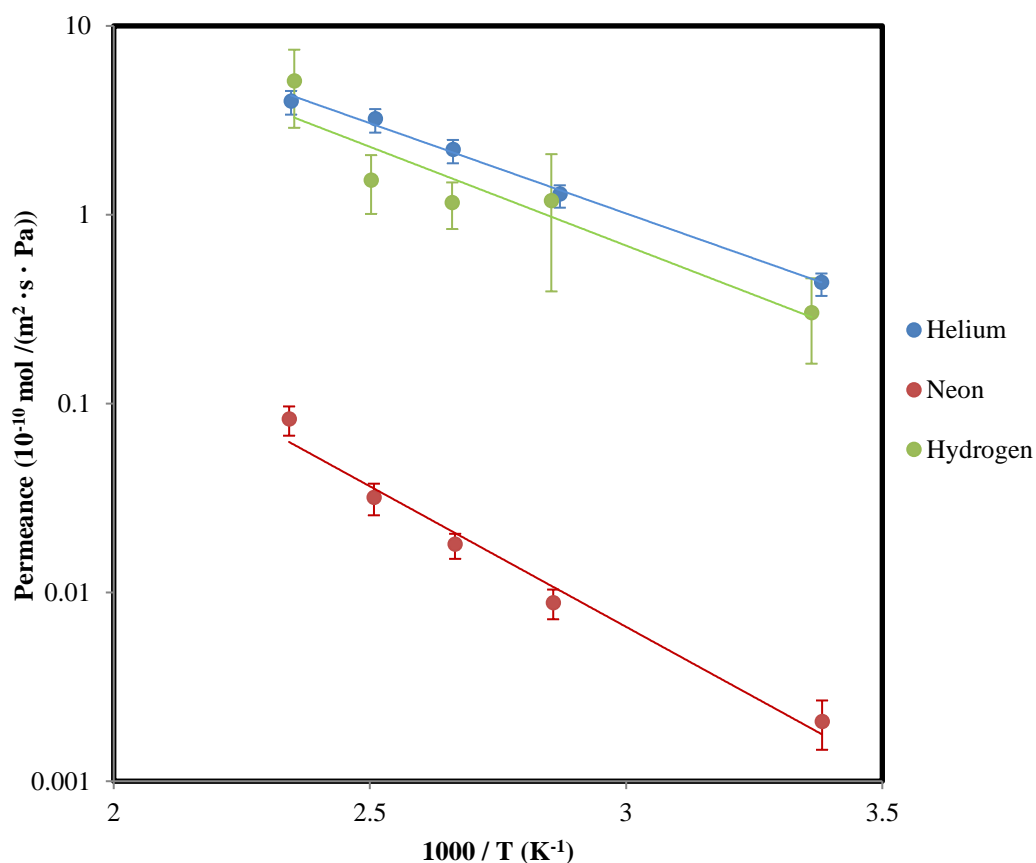
Figure 6.4. Arrhenius plot of Figure 6.3 showing the permeance of a nanographite membrane against the inverse of temperature. The lines are fitted exponential curves. The membrane is 350 nm thick and 1.1 mm in diameter.

Molecule	Activation energy (kJ/Mol)
He	18.31
H_2	20.03
Ne	28.50

Table 6.1. Summary of the calculated values of activation energy for H_2, He and Ne.

6.3.2 Separation behaviour

As observed in Figure 6.4, He and H_2 have similar values of permeance across all measured temperatures, whilst Ne has a value roughly two orders lower than the other two gases. Figure 6.5 and Table 6.2 shows a summary of the separation factors α of these gases, i.e. the ratio of the gas fluxes.

Temperature (°C)	Separation factor α for H_2/Ne	Separation factor α for He/Ne
25	146.3	212.3
75	134.2	145.8
100	64.4	122.9
125	47.8	101.3
150	61.7	48.3

Table 6.2. Summary of the separation factor of H_2 and He, over Ne. The membrane is 350 nm thick and 1.1 mm in diameter.

There is a clear decrease in the selectivity for both gases at higher temperatures. Ne has a higher activation energy than He or H_2, and thus its permeance increases relatively more at higher temperatures. However, at all temperatures, the flow cannot be dominated by Knudsen diffusion because the selectivity is much larger than predicted from Equation 6.5 $\left(\alpha_{knudsen} = \sqrt{M_{Ne}/M_{He}} = 2.2 \right)$. Hence, a mechanism other than pure Knudsen must be occurring.
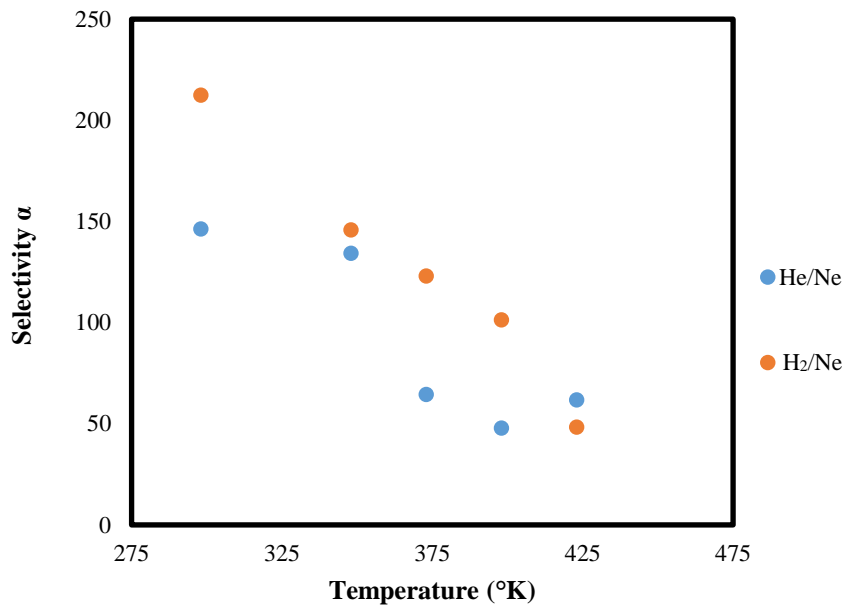
Figure 6.5. Graph showing the separation factor α between He / H_2 and Ne, respectively at a temperature range of 25 to 150 °C. The membrane is 350 nm thick and 1.1 mm in diameter.

100

Here, I compare the results of measurement of the membrane permeation using two separate methods; the 'vacuum method' and the 'closed volume method'. The two methods are similar experimentally and should yield equal results for permeation.

I have used the closed volume method throughout testing and the results in previous Sections are taken from this method solely. This is due to the relatively higher sensitivity obtained from the closed volume method. For example, the permeation of He at temperatures below 100 °C could not be measured using the vacuum method. This non-result was because the measured flux and pressure of the analyte gas was below the RGA background noise pressure at these temperatures. The vacuum method is a continuous method of measurement, whilst the closed volume method enables the pressure to build up over time.
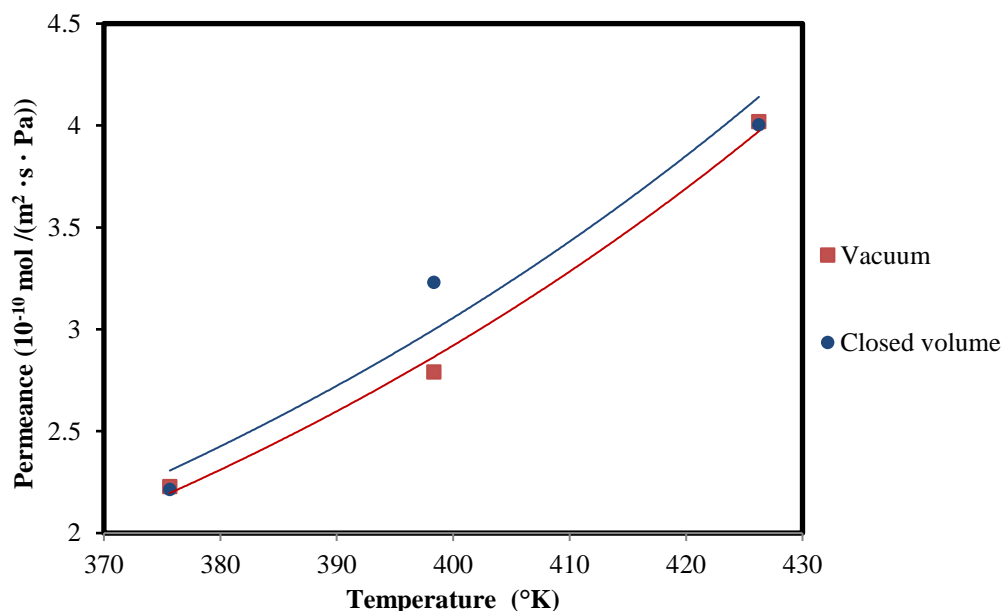
Figure 6.6. Plot showing the comparison of permeance of He flowing through a 350 nm thick nanographite membrane, using two different measurement methods. The lines are fitted exponential curves. The temperature ranges from 100 to 150 °C.

Figure 6.6 shows a graph comparing two results taken under identical conditions and shows that the results of the two method agree very closely. The gradient of the Arrhenius plot, representing the activation energies calculated across this temperature range, give 15.18 and 15.22 kJ/mol, within 0.25 % agreement, for the closed volume and vacuum methods respectively. The values of activation energy are slightly lower than those measured across the larger temperature range of 25 to 150 °C (Table 6.1), and because of the limited temperature range of the data in Figure 6.6 is probably less accurate.

The permeance values are also close, varying by 0.6, 13.6 and 0.4 % at temperatures of 100, 125 and 150 °C, respectively. The two methods appear to agree well and there is clearly no evidence of any systematic error between the two methods.

6.4 Discussion of results

6.4.1 Identification of separation mechanism

The membrane shows activated permeation which is consistent with a gas translation type behaviour since the permeation increases with temperature [169] and the permeance of the most massive molecule (Ne) is lower than that of He and H_2. This is evidenced in the increase in permeation with temperature as shown in Figures 6.3 and 6.4.

Hence, I have modelled the behaviour of permeation versus temperature using the experimentally extracted values of E_a. To do so, in Equation 6.9, I insert the diffusion coefficient D_{GT} (Equation 6.8) into the Equation for permeance (Equation 6.3):

$$B = \frac{G_1 - G_2}{L \cdot a \cdot p} A_{GT} \sqrt{\frac{8RT}{\pi M}} \exp\left(\frac{-E_{GT}}{RT}\right)$$
(6.9)

For each point, all parameters are known except for A_{GT}. The values of E_{GT} are taken from Table 6.1. A_{GT} is a geometric constant which is related to the pore size, tortuosity and porosity of the membrane. Since these parameters are difficult to measure, the value of A_{GT} is normally inferred by regression of the permeability results [163]. In this case, I infer the value of A_{GT} by initially assuming its value to be 1, and then scaling the result to the measured value of permeance. To do so, I took the relative values which were measured and predicted for B at each point, and took the mean of these numbers. For example, assuming $A_{GT}=1$, the predicted value of B (Equation 6.9) for He at 150 °C for a nanographite membrane of 1.1 mm diameter is 6.4×10^4 mol /(m^2 ·s · Pa), whereas the measured value of B is 4.0×10^{-10} mol /(m^2 ·s · Pa). Thus, the value of A for this point is 6.3×10^{-15}. I have averaged the values of A over all the measured points and obtained a mean value of $A_{GT} = 4.33 \times 10^{-15}$ for the nanographite membrane. I have only used the values for He and Ne to obtain this average. This is due to the relatively large errors in the data in the H_2 permeance, which is cause by the large background signal of the RGA for H_2. The predicted plots, using this value of A_{GT}, are shown in Figure 6.7 alongside the experimental results.
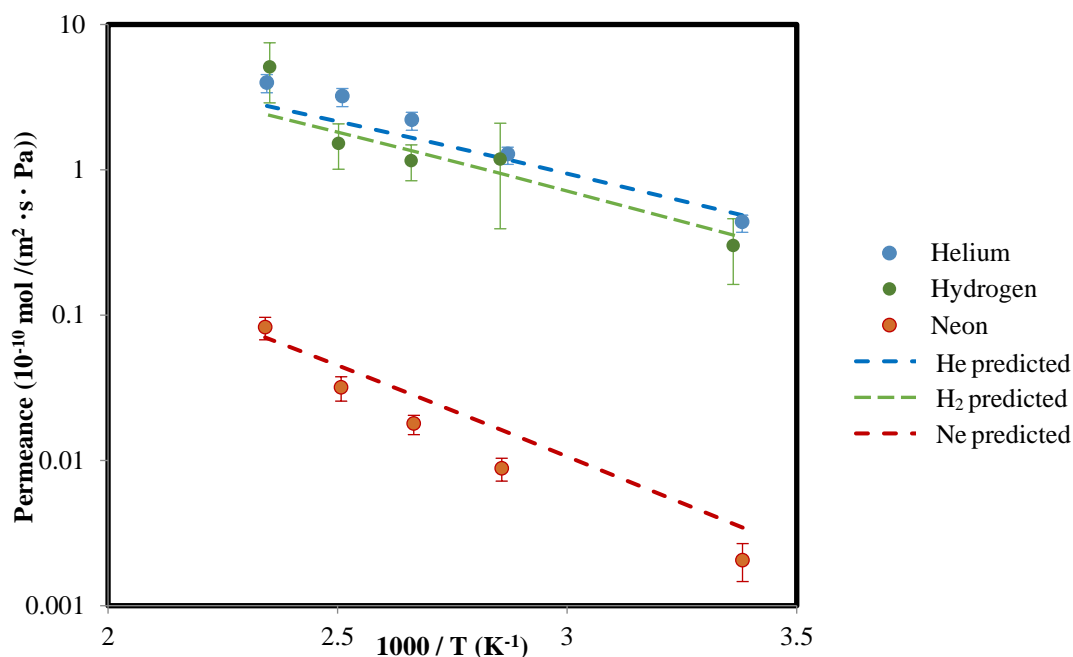
Figure 6.7. The experimental values (solid data points) of permeation for He, Ne and H_2, across a temperature range of 25 to 150 °C for a 350 nm thick membrane. Predicted results modelled using gas translational mechanism (Equation 6.9) are included for comparison (dashed lines). The scaled value of $A = 4.33 \times 10^{-15}$.

Figure 6.7 shows that the general trends of permeation for these three gases can be reasonably approximated using a gas translational diffusion model. There is a slight overestimation of Ne at lower temperatures. However, the model shows a reasonable estimation of the behaviour for these gases, and can be used for predictive purposes. Measurement of other gases, as well as the absorption behaviour, may be useful to better understand the sieving mechanism of nanographite, but have not been measured as part of this work. Part of the difficulty inhibiting this investigation was the very low permeation of most gases through the nanographite membrane, as detailed below.

6.4.2 Measurement of larger molecules

The permeation of CO_2 and O_2 through the nanographite membrane was measured at 125 and 150 °C respectively. In both cases, the permeation of the gas was below the background noise of the system. As a result, no absolute values of gas permeation and separation were obtained. However, I can estimate a maximum possible value of permeance, as set by the experimental noise. I have conservatively estimated that a 50 % increase in the measured pressure, above the background signal, would be the minimum clearly detectable signal. The resulting values are summarised in Table 6.3 along with the corresponding minimum values of gas separation compared to H_2 and He which were also measured for this membrane.

103

Gas	Maximum permeance (mol /(m^2 · s · Pa))	Separation factor α for H$_2$	Separation factor α for He
CO$_2$	1.12×10^{-12}	135	286
O$_2$	4.76×10^{-15}	84,000	107,000

Table 6.3. Summary of the maximum estimated values of CO$_2$ and O$_2$, and the calculated separation factors α of between H$_2$, He and those two gases. The temperature is 150 °C (O$_2$) and 125 °C (CO$_2$), for a 350 nm thick membrane.

The results show that CO$_2$ has a maximum permeance similar to that of Ne, whilst that of O$_2$ is considerably lower. However this is misleading because it is largely due to the vast difference in the size of the background signal in either case. It is important to recall that the noise level varied for each RGA peak because the background pressure rise is different at each mass setting of the RGA, for example the background signal of CO$_2$ (44 AMU) is relatively large due to outgassing occurring from the chamber internal surfaces. Thus it is possible that the actual permeance of CO$_2$ is much lower. In contrast there is very little O$_2$ present in the chamber; and the background signal at 32 AMU is very low. That no permeation of O$_2$ could be detected through the membrane, even above this low background signal, shows the good molecular sieving qualities of the nanographite membrane, as indicated by the very high values of α.

The permeance behaviour has been shown to fit well with a gas translational model. The general trend of membranes which have permeance dominated by gas translational diffusion is that larger molecules and more massive molecules have smaller permeance through the membrane. For example, if the kinetic diameter k_d is slightly larger than the pore size d_p then there is a net repulsive force on the molecule, which may greatly reduce the permeance [164]. This is because the value of E_{GT} in Equation 6.8 depends on the ratio of the pore size to the kinetic diameter of the molecule [162]. If the mechanism of separation is purely gas translational, then it would be expected that the order of permeance would follow the order of k_d for the measured molecules as shown in Table 6.4. A graph showing the permeance against the kinetic diameter of the molecule is shown in Figure 6.8. CO$_2$ is omitted due to the very large error caused by the background noise which means the permeance is unlikely to be a close estimate.

Molecule	Kinetic diameter (Å)
Helium [170]	2.60
Neon [166]	2.75
Hydrogen [170]	2.89
Carbon dioxide [170]	3.39
Oxygen [171]	3.46

Table 6.4. Kinetic diameters of the gases measured in this investigation.
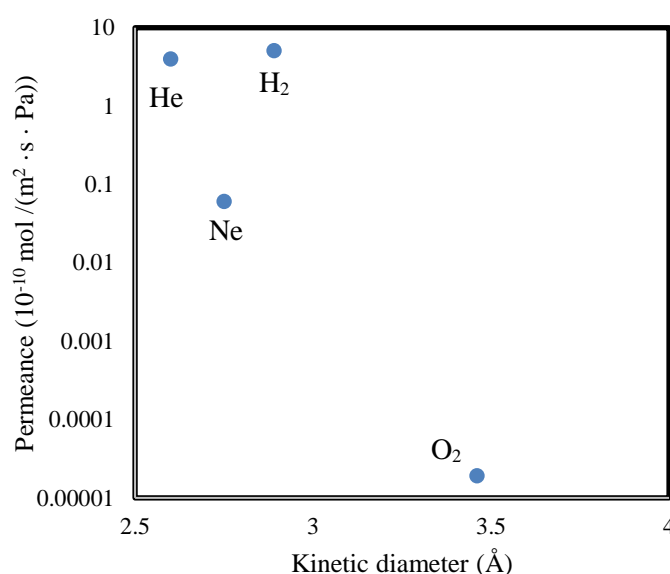
Figure 6.8. Graph showing the permeance of He, Ne, H_2, and O_2 at a temperature of 150 °C, plotted as a function of the kinetic diameter of each gas. The membrane was 350 nm thick.

The results in Figure 6.8 show a general trend of decreasing permeance with larger molecules. The permeation of Ne is lower than may be expected, compared with H_2, which is shown by the higher activation energy compared with H_2 (28.50 compared with 20.03 kJ/Mol). The pre-exponential term in Equation 6.9 includes a dependency on mass; however this dependency only gives rise to separation factors as calculated in Equation 6.5, which is smaller than that observed here. This may be indicative that the mechanism is not purely gas translational, and has some differential surface diffusion occurring [163]. Similar behaviour has been observed in other membranes for which the permeance is dominated by gas translational and molecular sieving. For example, the permeance of H_2 has been observed to be higher than that of He in graphene-oxide membranes [16] and the permeance of H_2 has been measured to be higher than that of Ne in zeolite membranes [166].

Here, I compare the gas separation properties of nanographite membranes with some others from the literature. The most viable and useful current application for gas separation membranes is the separation of CO_2 and H_2. There is plentiful literature on membranes for this purpose [115,172–174] and Figure 6.9 compares the nanographite membrane with literature values of H_2 permeance and α. Although the permeation value for CO_2 is only an estimate, the gas pairing $\alpha_{H2/CO2}$ is most commonly compared, and this, then, enables some comparison with the literature. Note that Figure 6.9 uses the permeation units of Barrer for H_2 which is defined as $10^{-10} \dfrac{cm^3(STP) \cdot cm}{sec \cdot cm^2 \cdot cmHg}$. Therefore, the H_2 permeance for the nanographite membrane is 0.16 Barrer for H_2 and 0.001 Barrer for CO_2. This is a thickness normalised unit, allowing for easier comparison between the materials. Temperature results at around 100 to 150 °C have been used for best comparison, though this was not always available in the literature for all experiments.
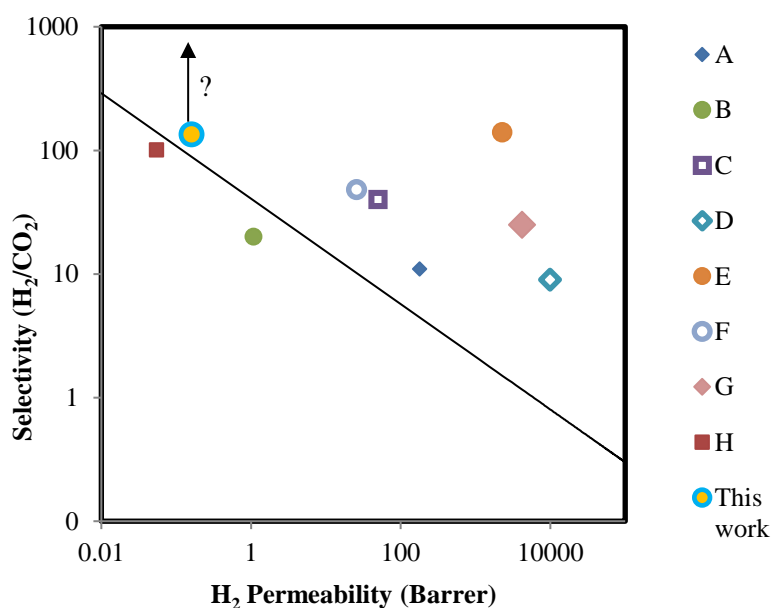
Figure 6.9. Comparison of the H_2 permeability and separation performance with CO_2 of a range of membranes. The black line represents the empirical upper bound for polymeric membranes [103]. References and experimental temperatures listed below:

A [125]   150 °C.   B [16]   100 °C.   C [172]   140 °C.   D [115]   25 °C.

E [173]   200 °C.   F [104]   150 °C.   G [174]   150 °C.   H [175]   35 °C.

This work: 125 °C.

The permeation of H_2 for nanographite is among the lowest of the relevant literature, whilst the selectivity between H_2 and CO_2 is among the highest. This is a common trade off; and shows that nanographite may represent an interesting material for gas separation, but requires a lower thickness than other materials to become useful towards industrial applications. It is interesting to note that the

selectivity value represents a minimum (because the permeance is only a maximum estimate) and the actual value may be much higher than this. The high apparent separation between H_2/O_2 suggests that nanographite exhibits qualities of high sieving of larger molecules.

6.5 Summary and conclusions

In this Chapter, I have studied the gas permeation properties of nanographite membranes using a UHV system which I constructed. The flow of He, Ne, H_2, O_2 and CO_2 was measured and the results all showed an activated permeation process, with permeance increasing with temperature; thus suggesting a gas translational type mechanism. Permeation of He, H_2 and Ne respectively was measured between temperatures of 25 °C and 150 °C. However, the permeance of the larger molecules (O_2 and CO_2) was below the background noise of the RGA and could not be measured.

Overall, the material has a low permeability to all gases. Its permeance for H_2 is amongst the lowest in the literature. However, the overall selectivity of the membrane was high, particularly so for H_2/O_2 (>84,000). This is effectively apparently impermeable to O_2. This combination of gases is uncommon (due to the flammability of H_2 in O_2) and there is little literature to compare to. However, as a related example of molecular sieving, N_2 is a molecule of similar size to O_2 (3.64 Å vs. 3.46 Å), and it is reasonable that the permeance of N_2 and O_2 are similar through a nanographite membrane. A value of α for the gas pair H_2/N_2 of 960 is considered very high [103] [176]. Hence, the separation of H_2/O_2 suggests that the nanographite material may be of significant interest.

A consequence of this low permeability of nanographite is that it may only realistically be used at higher temperatures and low thicknesses to obtain a reasonable trade-off in permeance and selectivity. For example, extrapolating the results of Figure 6.4 to a temperature of 400 °C would yield a permeance of around 2×10^{-9} mol /(m$^2 \cdot$s $\cdot$ Pa) for this membrane, which is 350 nm thick. The thickness of the membrane in this experiment has been limited by the need for a suitably robust freestanding structure, and the temperature has been limited by the stability of the copper gaskets in the UHV system. Another method of using membranes is to support the membrane on a more porous base, thereby enabling a much thinner layer to be used. Reasonably, a 5 nm layer could be used (this was the thickness used for NEMS switches in work by Sun *et al.* [68] which is an application requiring a robust and continuous film). A membrane of this thickness would yield an absolute H_2 permeance of around 14×10^{-8} mol / (m$^2 \cdot$s$\cdot$Pa) at 400 °C, assuming a linear thickness relationship for permeance, which is generally true for most materials, though not in graphene-oxide [16]. This, in terms of absolute permeance would compare well with the reviewed literature in Chapter 2, especially with the promising value of separation for H_2/O_2.

The permeance was modelled as a membrane with diffusion dominated by gas translational diffusion (Equation 6.9). The results of the permeance were scaled to the model using a value for the geometric constant $A_{GT} = 4.33 \times 10^{-15}$. The model gave a reasonable agreement to the experimental result. This demonstrates that the simple model allows for predictions of membrane performance to be made.

The gas permeation results suggest that further study on the use of nanographite molecular sieves is warranted, with promising potential for gas separation. Specifically, measurement of the following is considered useful:

- Measurement of the full permeance of CO_2 and obtaining an accurate H_2/CO_2 separation factor.
- Measurement of the permeance and sieving behaviour at increasingly higher temperatures (400-500 °C) and thereby increase the H_2 and He permeance.
- Measurement of the permeance of ultra-thin (< 10 nm) nanographite membranes.

Methods of modifying the film properties may be of interest to increase the film permeability. For example, annealing nanographite increases its crystallite structure [177], with Raman spectroscopy showing that annealing causes a change in the density of defects of the nanographite film. This change may thereby alter the permeance characteristics. Further study of the annealing behaviour in nanographite and the corresponding effect on permeance would be of interest.

The ease and scalability of fabricating nanographite based membranes is good. For example it can be deposited simply using PECVD and this can be done uniformly over the diameter of an 8-inch silicon wafer. The substrate could then be used as a framework to support the membranes, as shown by Huebner *et al.* [178], or the film could be delaminated from the substrate and used with a porous support. I performed a simple small-scaled experiment by immersing a nanographite coated fused quartz chip (1 cm^2) in 49 % HF acid. Upon immersion in the HF, the film quickly delaminated from the fused quartz, as a single sheet, and floated atop the liquid surface. I then transferred the floating sheet to a patterned silicon chip with a hole etched through its thickness, which is another method to fabricate freestanding nanographite membranes. This method could potentially be scaled up for large-sized supported membranes.

This investigation into the gas permeation properties of nanographite has confirmed that it is a potentially useful material for MEMS membrane-based pressure sensors, for use in harsh environments. This is because the gas permeation for larger molecules is very low, and a thick (>1µm) nanographite membrane would not undergo any significant change in displacement caused

by leakage. The retention of mechanical properties for graphitic materials is very good, and they may be used above 2000 °C [7] in a non-oxidising environment. The fused quartz substrate used for these membranes is also a suitable material for high temperatures, and this material combination represents a promising basis for fabricating nanographite membrane sensors.

Jian *et al.* [179] fabricated from gold/polymer nanocomposite membranes. The nanocomposite had a Young's modulus of between 4.3 to 9.6 GPa and thickness of 25 to 70 nm. The membranes had much higher sensitivity than the theoretical limit of silicon membranes of the same dimensions as a result of the lower thickness. The low modulus of nanographite places this material into a similar stiffness regime as the polymeric nanocomposite, but coupled with the high temperature resistance of nanographite, could be a more widely useful material.

7. Conclusions and future work

7.1 Conclusions

Over the course of this Thesis, the predominant objective has been to characterise nanographite, which is a thin film deposited using catalyst-free PECVD, in applications which use MEMS and NEMS-type fabrication. This has been achieved through the measurement of intrinsic material properties, and also demonstrated through the use of novel fabrication methods.

The first step was to measure the Young's modulus of nanographite. To do so, I fabricated released square membranes, of thickness between 275 and 296 nm, and side length between 193 and 273 µm, by etching through the silicon substrate. As the nanographite film was released from the substrate, its compressive built-in stress caused out-of-plane buckling. I measured the amplitude of buckling using interferometry, and from this, calculated the in-plane strain using a mathematical model by Ziebart *et al.* [136]. From this measurement, I extracted a compressive strain of -0.0142. I also measured the stress of the film, using the change in wafer bowing of the substrate after deposition, as 436 MPa. Using the measured values of stress and strain, the Young's modulus was calculated to be 23 GPa. I then input this value into a nonlinear finite element simulation of doubly-clamped beams, with a close agreement between the simulated and experimental buckling behaviour.

After this first step of measuring the Young's modulus of nanographite, I went on to fabricate resonator devices from cantilever beams and doubly-clamped beams. All the devices were of length between 75 and 150 µm and thickness between 270 and 340 nm. These were fabricated using surface micromachining on a 6-inch silicon substrate, with a 200 nm SiO_2 layer and with titanium / nickel electrodes. A major issue of fabricating released microstructures, such as doubly-clamped beams, from a compressively stressed film is buckling. In this work, a relatively large undercut (25 to 30 µm, of 200 µm wide anchors) was used to overcome buckling. This undercut, due to the stress gradient of the film, caused upward deflection, whereby the anchors deflected up away from the substrate. This effectively applied a tensile force to the beam and stopped the buckling. To characterise the resonant frequencies and quality factors, I actuated the beams electrostatically and used laser Doppler vibrometry to measure the vibration. The resonant frequencies of the cantilevers were between 5 and 25 kHz, and for doubly-clamped beams, were between 245 and 640 kHz. Quality factors under ambient pressure were around 5 to 10 for cantilevers and 20 to 30 for doubly-clamped beams.

I compared the measured resonant frequencies of the cantilevers to a mathematical model for natural frequency, using 23 GPa as the value of Young's modulus. There was a close agreement, which confirmed the measured value of Young's modulus measured from the previous Chapter. I fit the measured results of the resonant frequencies of doubly-clamped beams to a model of beams under tensile force, with a stress of 10 to 20 MPa applied. The effect of the stress was to greatly increase the value of the natural frequency over the stress-free value. One doubly-clamped beam was wire-bonded and measured in vacuum conditions (30 mTorr), with a higher quality factor of around 1800. The fabrication of nanographite MEMS resonators, and particularly the method of obtaining buckling-free structures, may pave the way towards highly sensitive MEMS and NEMS sensors, which may be used in harsh environments.

In my final experiment, I fabricated nanographite membranes on fused quartz substrates. The testing of gas permeance of nanographite membranes was useful for two applications:

- To test the gas permeation and separation for possible application as a molecular sieve.
- To test the gas permeation for possible application as a MEMS-based pressure sensor.

I constructed and used an RGA mass-spectrometry system to measure the permeance of gases through a nanographite membrane. From these measurements, the permeance at 150 °C of H_2, He and Ne of 5.1, 4.0 and 0.08×10^{-10} mol /($m^2 \cdot s \cdot Pa$), respectively, was measured through a 350 nm thick membrane. Whilst the flow of O_2 and CO_2 was so low that it could not be measured using the RGA setup, the estimated minimum H_2/CO_2 separation factor of 135 is promising, and compares well with the available literature. I compared the results of the permeance to a model for gas translational diffusion and the model agreed well with the experimental results, and allows for prediction of the permeance of gases to be made.

7.2 Future work

7.2.1 Optimisation of process conditions for PECVD of nanographite thin films

The stress of the nanographite film is compressive when deposited onto a silicon substrate. A film with a high stress level is not generally ideal for MEMS and NEMS applications, since it causes deflection and buckling after release. The undercut method to obtain tensile-stressed doubly-clamped beams was, in this case, useful and may be applied to other materials. However, it is preferential for some applications, such as membrane-based pressure sensors and switches, for the average stress to be neutral or slightly tensile.

To obtain a film of lower stress level, an optimisation study of the deposition parameters should be undertaken. For example, low frequency excitation of the plasma has been used to tune the stress of silicon nitride deposited by PECVD [144] and this may potentially be employed for the deposition of nanographite. Substitutionally doping boron into the graphite lattice may also be an option to induce a tensile strain [180], since the carbon-boron bond length is larger than the carbon-carbon bond. Using a composite-bonded wafer may also be used to alter the thermal expansion coefficient of the substrate. The thermal expansion coefficient may be tuned to become close to that of nanographite, and thereby reduce thermally induced stresses. A similar method was employed by Delachat *et al.*[145] to fabricate buckling-free silicon membranes.

The optimisation of the PECVD parameters could also alter the grain structure of the film, which may alter its mechanical properties. This is because the Young's modulus of graphitic materials is highly anisotropic, and for polycrystalline graphite depends on the mismatch in orientation of its grains. If the deposition parameters were tuned to produce a film with larger grains, the relative orientation of the grains may rise and therefore increase the Young's modulus of the material. The grain size may also affect the quality factor for a resonator, since smaller grained materials tend to have higher losses [158]. A systematic study on the process parameters for depositing nanographite, and its effect on Young's modulus, quality factor and electrical properties would be useful in the further development of nanographite MEMS and NEMS.

7.2.2 Downscaling the MEMS resonators to NEMS

In this Thesis, the fabrication of devices has been on the micro-scale. This was due to the availability of low-cost lithographic masks using printed transparencies. However, many of the qualities (such as ultra-thin film deposition) of nanographite may be better employed using e-beam lithography for fabrication of NEMS structures. For example, this would better allow ultra-thin (< 5 nm) films to be used, with device feature sizes of < 50 nm. I attempted to fabricate 20 nm thick doubly-clamped resonators, though this was unsuccessful. I attribute this to the very high aspect ratios of the structures (length divided by thickness = 7500) which made release of the films difficult and they suffered stiction. Devices of smaller lateral dimensions may be easier to release, as shown by Sun *et al.* [68].

The scope of the investigation in Chapter 5 was to characterise the cantilevers and doubly-clamped beams as prototype resonators. To build on this work, NEMS nanographite resonators (of thickness < 5 nm) should be fabricated using e-beam lithography, and a method to obtain an electrical readout of the device deflection should be used. This would demonstrate the electrical integration of the nanographite device. For example, a capacitive readout as employed by Chen *et al.* [181] could be used. This device should then be tested under vacuum conditions, and subjected to a strain under a

high temperature thereby demonstrating the potential for highly sensitive nanographite resonators to be used for harsh environment sensing.

7.2.3 Increasing the permeance of nanographite membranes

One of the main difficulties and drawbacks of the investigation into the permeance of gases through nanographite membranes was the inability to fully measure the permeance of larger molecules, O_2 and CO_2. This was because the absolute flux was very low and below the background noise of the RGA. The separation factor α for H_2/CO_2 has therefore not been fully characterised, and this is shortcoming of the investigation at present. Measurement of this parameter will allow more accurate comparison between the molecular sieving properties of nanographite with the literature. Fabrication of a thin membrane, of larger area, would increase the overall flux of gases, and enable the measurement of the actual flux of CO_2. For example, this could be achieved by delaminating the film and using a porous support, or by fabricating a support structure as shown by Huebner *et al.* [178].

The overall permeance of gases through the nanographite membrane is low, and needs to be increased if it is to become industrially useful. To investigate methods of increasing the permeance of nanographite, the relationship between the crystallite structure of nanographite and its permeance should be quantified. For example, as discussed above, the deposition parameters may be tuned to alter the crystallite size of nanographite. The effect of different average crystal size on the gas permeance should be investigated. Similarly, post-deposition annealing has been shown to increase the crystallite size in nanographite films [177], and this may also be investigated for its effect on gas permeance.

A1. Finite element analysis of the buckling amplitude of doubly-clamped nanographite beams

<u>A 1.1. Mesh refinement study</u>
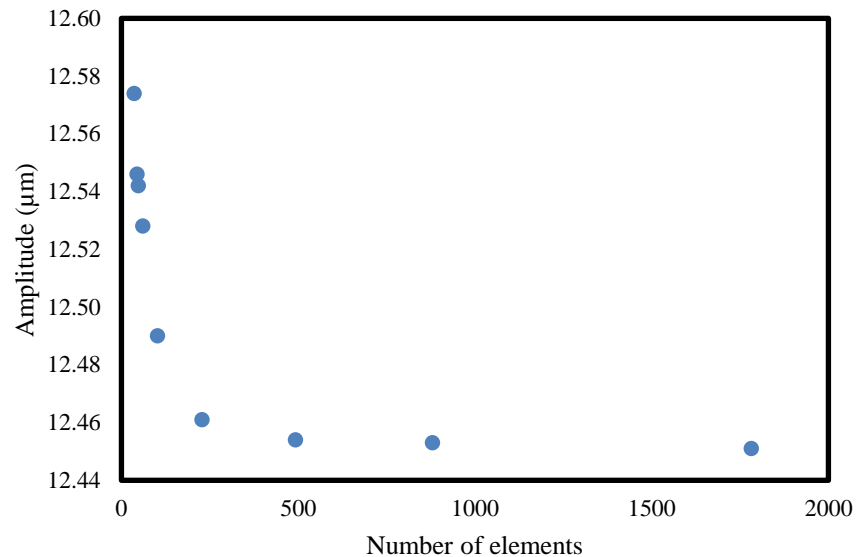
<u>A 1.2. ANSYS parametric design language code for buckled doubly-clamped beam</u>

/TITLE, Amplitude of Buckled nanographite C-C Beam

/PREP7

E=23e9 !Young's modulus

hs=0.394e-6 !Thickness of beam

c=140e-6 !Beam length (released section)

b=11e-6 ! Beam width

j=10e-6 ! Clamped length

t=225e-9 !Step thickness

o=436e6 !Stress

esz=1e-6

MP,EX,1,E

MP,DENS,1,1900 !Density

MP,PRXY,1,0.25 !Poisson's ratio

MP,ALPX,1,(o/E) !CTE is thermally applied strain ε

MP,ALPY,1,(o/E)

ET,1,SHELL281 !2D Shell element

SECTYPE,1,SHELL,

!Geometry
SECDATA,hs,1,0,, !Thickness

k,1,0,0,0
k,2,j,0,0
k,3,j,b,0
k,4,0,b,0
a,1,2,3,4

k,5,j,0,t
k,6,c+j,0,t
k,7,c+j,b,t
k,8,j,b,t
a,5,6,7,8

k,9,0+c+j,0,0
k,10,j+c+j,0,0
k,11,j+c+j,b,0
k,12,0+c+j,b,0
a,9,10,11,12
a,2,5,8,3
a,12,7,6,9

AGLUE,ALL !Glue areas together

ESIZE,esz
MAT,1
AMESH,ALL, !Mesh all areas

!Boundary Conditions – fix the end beam areas

ASEL,S,,,1
NSLA,S,1
D,ALL,UZ,0
D,ALL,UY,0
D,ALL,UX,0

```
NSEL,ALL
ASEL,ALL
ASEL,S,,,3
NSLA,S,1
D,ALL,UZ,0
D,ALL,UY,0
D,ALL,UX,0
ASEL,ALL
NSEL,ALL


BF,ALL,TEMP,1 !Apply temperature of 1 °K


!Solver


/sol
ANTYPE,0 !Static analysis
NLGEOM,1 !Nonlinear geometry is on
NSUBST,100,100,100  !Apply load over 100 steps
AUTOTS,0        !Do not use Auto-timestep
TIME,1
OUTRES,ALL,ALL
NROPT,FULL,
BCSOPTION,,INCORE,
NCNV,0,1e10


solve
```

A 2. Finite element analysis of the resonance of nanographite cantilever beams with undercut and stress gradient.

A 2.1. Mesh refinement study of the modal analysis of cantilever beams with undercut and stress gradient.
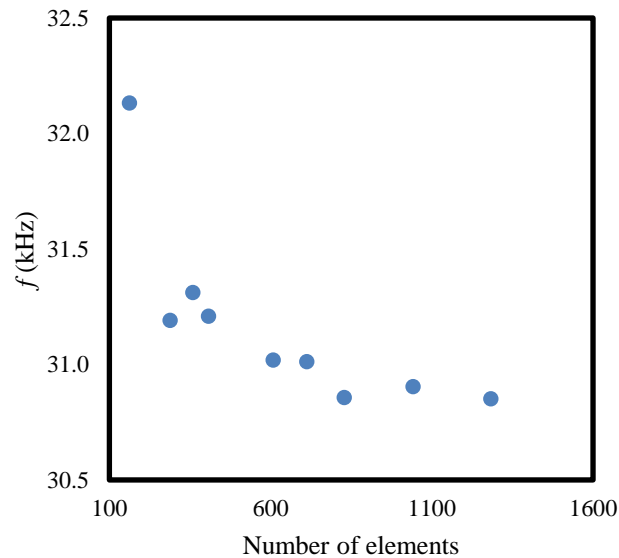
A 2.2. ANSYS parametric design language code for the nonlinear deflection and modal analysis of cantilever beams with undercut and stress gradient.

```
/TITLE, Deformation + modal analysis of cantilever under strain gradient
/PREP7
!the temperature gradient gives an average stress of 436 MPa and a gradient of 142 MPa/um
hs=0.35e-6 !thickness
A=200e-6 !anchor width
u=10e-6 !undercut (u+e is total undercut)
e=15e-6 !electrode overlap
c=75e-6 !cantilever length
b=10e-6 !cantilever width
esz=10e-6 !element size
p=1900 !Density
Y=23e9 !Young's modulus

ANTYPE,STATIC,
ET,1,SHELL281
n=5 !number of layers
```

```
ET,2,SHELL281
n=5 !number of layers

MP,EX,1,Y !NCG Y Modulus !bottom layer
MP,DENS,1,p !density
MP,PRXY,1,0.25 !Poisson's ratio
MP,ALPX,1,-2.00326E-05 !Thermal expansion coefficient
MP,ALPY,1,-2.00326E-05

MP,EX,2,Y
MP,DENS,2,p
MP,PRXY,2,0.25
MP,ALPX,2,-1.94946E-05
MP,ALPY,2,-1.94946E-05

MP,EX,3,Y
MP,DENS,3,p
MP,PRXY,3,0.25
MP,ALPX,3,-1.89565E-05
MP,ALPY,3,-1.89565E-05

MP,EX,4,Y
MP,DENS,4,p
MP,PRXY,4,0.25
MP,ALPX,4,-1.84185E-05
MP,ALPY,4,-1.84185E-05

MP,EX,5,Y
MP,DENS,5,p
MP,PRXY,5,0.25
MP,ALPX,5,-1.78804E-05
MP,ALPY,5,-1.78804E-05

MP,EX,6,200E9
MP,DENS,6,8900
MP,PRXY,6,0.25
MP,ALPX,6,0
```

MP,ALPY,6,0

SECTYPE,1,SHELL,
SECDATA,hs/n,1,0,,
SECDATA,hs/n,2,0,,
SECDATA,hs/n,3,0,,
SECDATA,hs/n,4,0,,
SECDATA,hs/n,5,0,,

SECTYPE,2,SHELL,
SECDATA,hs/n,1,0,,
SECDATA,hs/n,2,0,,
SECDATA,hs/n,3,0,,
SECDATA,hs/n,4,0,,
SECDATA,hs/n,5,0,,
SECDATA,50e-9,6,0,,

k,1,0,0,0
k,2,A,0,0
k,3,A,A,0
k,4,0,A,0

k,5,a-u-e,u+e,0
k,6,a-u-e,A-u-e,0
k,7,u+e,u+e,0
k,8,u+e,A-u-e,0

k,9,a-u,u,0
k,10,a-u,A-u,0
k,11,u,u,0
k,12,u,A-u,0

k,13,A,(A/2)-(b/2),0
k,14,A,(A/2)+(b/2),0
k,15,A+c,(A/2)-(b/2),0
k,16,A+c,(A/2)+(b/2),0

```
a,1,2,3,4
a,11,12,10,9

ASBA,1,2,,delete

a,11,12,10,9
a,7,8,6,5
ASBA,1,2,,delete
a,13,15,16,14
btol,1e-7
aglue,all !glue all areas

ESIZE,esz

ASEL,S,area,,2
AATT,,,,,1
AMESH,all

ASEL,S,area,,4
AATT,,,,,2
AMESH,all
asel,all

ASEL,S,area,,1
AATT,,,,,1
AMESH,all
!boundary conditions
LSEL,S,,,9,
LSEL,A,,,10,
LSEL,A,,,11,
LSEL,A,,,12,

NSLL,S,1, !select nodes attached to the 4 contrained lines

D,ALL,UX,0
D,ALL,UY,0
D,ALL,UZ,0
```

```
D,ALL,ROTX,0
D,ALL,ROTY,0
D,ALL,ROTZ,0
NSEL,ALL
LSEL,ALL

NSEL,ALL
ASEL,ALL

BF,ALL,TEMP,1000
NSEL,ALL
LSEL,ALL
ASEL,ALL
/solu

ANTYPE,0
NLGEOM,1 !nonlinear static analysis
PSTRES,ON
NSUBST,1000,10000,1000  !number of steps
save,'NLGEOMBeamModalanalysis','rstp'
AUTOTS,1      !autotimestep 0 is off, 1 is on
TIME,1
OUTRES,ALL,ALL
NROPT,FULL,
BCSOPTION,,INCORE,

solve

/solu
antype,,restart,1,1000,perturb     ! restart option for linear perturbation from 1000 substep
perturb,modal
solve,elform
/com
modopt,lanb,5
mxpand,5
solve
```

122

References

[1]   V. Cimalla, F. Niebelschutz, K. Tonisch, C. Foerster, K. Brueckner, I. Cimalla, T. Friedrich, J. Pezoldt, R. Stephan, M. Hein, Nanoelectromechanical devices for sensing applications, Sensors and Actuators B: Chemical. 126 (2007) 24–34. doi:10.1016/j.snb.2006.10.049.

[2]   S.S. Verbridge, J.M. Parpia, R.B. Reichenbach, L.M. Bellan, H.G. Craighead, High quality factor resonance at room temperature with nanostrings under high tensile stress, Journal of Applied Physics. 99 (2006) 124304. doi:10.1063/1.2204829.

[3]   N. Ono, K. Kitamura, K. Nakajima, Y. Shimanuki, Measurement of Young's Modulus of Silicon Single Crystal at High Temperature and Its Dependency on Boron Concentration Using the Flexural Vibration Method, Japanese Journal of Applied Physics. 39 (2000).

[4]   A. Acun, B. Poelsema, H.J.W. Zandvliet, R. Van Gastel, The instability of silicene on Ag(111), Applied Physics Letters. 103 (2013). doi:10.1063/1.4860964.

[5]   O.L. Blakslee, Elastic Constants of Compression-Annealed Pyrolytic Graphite, Journal of Applied Physics. 41 (1970) 3373. doi:10.1063/1.1659428.

[6]   M.A. Hopcroft, W.D. Nix, T.W. Kenny, What is the Young's Modulus of Silicon?, Journal of Microelectromechanical Systems. 19 (2010) 229–238. doi:10.1109/JMEMS.2009.2039697.

[7]   C. Malmstrom, R. Keen, L. Green, Some Mechanical Properties of Graphite at Elevated Temperatures, Journal of Applied Physics. 22 (1951) 593. doi:10.1063/1.1700013.

[8]   K.S. Novoselov, A.K. Geim, S. V. Morozov, D. Jiang, Y. Zhang, S.V. Dubonos, I. V. Grigorieva, A.A. Firsov, Electric field effect in atomically thin carbon films., Science. 306 (2004) 666–9. doi:10.1126/science.1102896.

[9]   J.S. Bunch, A.M. van der Zande, S.S. Verbridge, I.W. Frank, D.M. Tanenbaum, J.M. Parpia, H.G. Craighead, P.L. McEuen, Electromechanical resonators from graphene sheets., Science. 315 (2007) 490–3. doi:10.1126/science.1136836.

[10]   S.M. Kim, E.B. Song, S. Lee, S. Seo, D.H. Seo, Y. Hwang, R. Candler, K.L. Wang, Suspended few-layer graphene beam electromechanical switch with abrupt on-off characteristics and minimal leakage current, Applied Physics Letters. 99 (2011) 23103. doi:10.1063/1.3610571.

[11]   A.D. Smith, S. Vaziri, F. Niklaus, A.C. Fischer, M. Sterner, A. Delin, M. Östling, M.C. Lemme, Pressure sensors based on suspended graphene membranes, Solid-State Electronics. 88 (2013) 89–94. doi:10.1016/j.sse.2013.04.019.

[12]   S.P. Koenig, L. Wang, J. Pellegrino, J.S. Bunch, Selective molecular sieving through porous graphene., Nature Nanotechnology. 7 (2012) 728–32. doi:10.1038/nnano.2012.162.

[13]   Y. Yampolskii, B. Freeman, Membrane Gas Separation, John Wiley & Sons, Ltd., Chichester, UK, 2010. doi:10.1002/9780470665626.

[14]   S.P. Koenig, Graphene Membranes: Mechanics, Adhesion, and Gas Separations, University of Colorado at Boulder, 2013.

[15]   J.S. Bunch, S.S. Verbridge, J.S. Alden, A.M. Van Der Zande, J.M. Parpia, H.G. Craighead, P.L. McEuen, Impermeable atomic membranes from graphene sheets, Nano Letters. 8 (2008) 2458–62. doi:10.1021/nl801457b.

[16]   H. Li, Z. Song, X. Zhang, Y. Huang, S. Li, Y. Mao, H.J. Ploehn, Y. Bao, M. Yu, Ultrathin, Molecular-Sieving Graphene Oxide Membranes for Selective Hydrogen Separation, Science. 342 (2013) 95–98. doi:10.1126/science.1236686.

[17]   K.S. Kim, Y. Zhao, H. Jang, S.Y. Lee, J.M. Kim, K.S. Kim, J.-H. Ahn, P. Kim, J.-Y. Choi, B.H. Hong, Large-scale pattern growth of graphene films for stretchable transparent electrodes., Nature. 457 (2009) 706–10. doi:10.1038/nature07719.

[18]   X. Li, W. Cai, J. An, S. Kim, J. Nah, D. Yang, R. Piner, A. Velamakanni, I. Jung, E. Tutuc, S.K. Banerjee, L. Colombo, R.S. Ruoff, Large-area synthesis of high-quality and uniform graphene films on copper foils., Science. 324 (2009) 1312–4. doi:10.1126/science.1171245.

[19]   J. Lee, E.K. Lee, W. Joo, Y. Jang, B. Kim, J.Y. Lim, S. Choi, S.J. Ahn, J.R. Ahn, M. Park, C. Yang, B.L. Choi, S. Hwang, D. Whang, Wafer-Scale Growth of Single-Crystal Monolayer Graphene on Reusable Hydrogen-Terminated Germanium, Science. 344 (2014) 286–289. doi:10.1126/science.1252268.

[20]   K.M. Milaninia, M.A. Baldo, A. Reina, J. Kong, All graphene electromechanical switch fabricated by chemical vapor deposition, Applied Physics Letters. 95 (2009) 183105. doi:10.1063/1.3259415.

[21]   W. Yang, C. He, L. Zhang, Y. Wang, Z. Shi, M. Cheng, G. Xie, D. Wang, R. Yang, D. Shi, G. Zhang, Growth, characterization, and properties of nanographene., Small. 8 (2012) 1429–35. doi:10.1002/smll.201101827.

[22]   M.E. Schmidt, C. Xu, M. Cooke, H. Mizuta, H.M.H. Chong, Metal-free plasma-enhanced chemical vapor deposition of large area nanocrystalline graphene, Materials Research Express. 1 (2014) 25031. doi:10.1088/2053-1591/1/2/025031.

[23]   J. Zhao, C. He, R. Yang, Z. Shi, M. Cheng, W. Yang, G. Xie, D. Wang, D. Shi, G. Zhang, Ultra-sensitive strain sensors based on piezoresistive nanographene films, Applied Physics Letters. 101 (2012) 63112. doi:10.1063/1.4742331.

[24]   A.W. Tsen, L. Brown, M.P. Levendorf, F. Ghahari, P.Y. Huang, R.W. Havener, C.S. Ruiz-Vargas, D.A. Muller, P. Kim, J. Park, Tailoring electrical transport across grain boundaries in polycrystalline graphene., Science (New York, N.Y.). 336 (2012) 1143–6. doi:10.1126/science.1218948.

[25]   C.T.C. Nguyen, MEMS technology for timing and frequency control., IEEE Transactions on Ultrasonics, Ferroelectrics, and Frequency Control. 54 (2007) 251–70. http://www.ncbi.nlm.nih.gov/pubmed/17328323.

[26] V. Lindroos, M. Tilli, A. Lehto, T. Motooka, T. Veijola, Handbook of Silicon Based MEMS Materials and Technologies, Elsevier Inc., Oxford, UK, 2010. doi:10.1016/B978-0-8155-1594-4.00014-0.

[27] P.S. Waggoner, H.G. Craighead, Micro- and nanomechanical sensors for environmental, chemical, and biological detection., Lab on a Chip. 7 (2007) 1238–55. doi:10.1039/b707401h.

[28] K.B. Gavan, E. van der Drift, W.J. Venstra, M.R. Zuiddam, H.S.J. van der Zant, Effect of undercut on the resonant behaviour of silicon nitride cantilevers, Journal of Micromechanics and Microengineering. 19 (2009) 8. doi:035003\r10.1088/0960-1317/19/3/035003.

[29] R.F. Wiser, M. Tabib-Azar, M. Mehregany, C.A. Zorman, Polycrystalline silicon-carbide surface-micromachined vertical resonators - Part II: Electrical testing and material property extraction, Journal of Microelectromechanical Systems. 14 (2005) 579–589. doi:10.1109/JMEMS.2005.844748.

[30] R.A. Barton, B. Ilic, A.M. van der Zande, W.S. Whitney, P.L. McEuen, J.M. Parpia, H.G. Craighead, High, size-dependent quality factor in an array of graphene mechanical resonators., Nano Letters. 11 (2011) 1232–6. doi:10.1021/nl1042227.

[31] S.P. Beeby, G. Ensell, B.R. Baker, M.J. Tudor, N.M. White, Micromachined silicon resonant strain gauges fabricated using SOI wafer technology, Journal of Microelectromechanical Systems. 9 (2000) 104–111. doi:10.1109/84.825784.

[32] J. Wang, Z. Ren, C.T.C. Nguyen, 1.156-GHz self-aligned vibrating micromechanical disk resonator, IEEE Transactions on Ultrasonics, Ferroelectrics, and Frequency Control. 51 (2004) 1607–1627. doi:10.1109/TUFFC.2004.1386679.

[33] T.R. Gaborski, J.L. Snyder, C.C. Striemer, D.Z. Fang, M. Hoffman, P.M. Fauchet, J.L. McGrath, High-performance separation of nanoparticles with ultrathin porous nanocrystalline silicon membranes, ACS Nano. 4 (2010) 6973–6981. doi:10.1021/nn102064c.

[34] W.J. Venstra, M.J. Capener, S.R. Elliott, Nanomechanical gas sensing with nonlinear resonant cantilevers., Nanotechnology. 25 (2014) 425501. doi:10.1088/0957-4484/25/42/425501.

[35] C.T.-C. Nguyen, L.P.B. Katehi, G.M. Rebeiz, Micromachined devices for wireless communications, Proceedings of the IEEE. 86 (1998) 1756–1768. doi:10.1109/5.704281.

[36] D.K. Agrawal, P. Thiruvenkatanathan, J. Yan, A.A. Seshia, Electrically coupled MEMS oscillators, 2011 Joint Conference of the IEEE International Frequency Control and the European Frequency and Time Forum (FCS) Proceedings. (2011) 1–5. doi:10.1109/FCS.2011.5977776.

[37] J.T.M. van Beek, R. Puers, A review of MEMS oscillators for frequency reference and timing applications, Journal of Micromechanics and Microengineering. 22 (2012) 13001. doi:10.1088/0960-1317/22/1/013001.

[38] H.C. Nathanson, W.E. Newell, R.A. Wickstrom, J.R. Davis, The Resonant Gate Transistor,

IEEE Transactions on Electron Devices. 14 (1967) 117–133. doi:10.1109/T-ED.1967.15912.

[39] M. Imboden, P. Mohanty, A. Gaidarzhy, J. Rankin, B.W. Sheldon, Scaling of dissipation in megahertz-range micromechanical diamond oscillators, Applied Physics Letters. 90 (2007) 152–155. doi:10.1063/1.2732163.

[40] J.E.Y. Lee, B. Bahreyni, Y. Zhu, A.A. Seshia, Ultrasensitive mass balance based on a bulk acoustic mode single-crystal silicon resonator, Applied Physics Letters. 91 (2007) 3–5. doi:10.1063/1.2822405.

[41] T.P. Burg, M. Godin, S.M. Knudsen, W. Shen, G. Carlson, J.S. Foster, K. Babcock, S.R. Manalis, Weighing of biomolecules, single cells and single nanoparticles in fluid., Nature. 446 (2007) 1066–9. doi:10.1038/nature05741.

[42] R.G. Azevedo, D.G. Jones, A. V. Jog, B. Jamshidi, D.R. Myers, L.C.L. Chen, X. Fu, M. Mehregany, M.B.J. Wijesundara, A.P. Pisano, A SiC MEMS Resonant Strain Sensor for Harsh Environment Applications, IEEE Sensors Journal. 7 (2007) 568–576. doi:10.1109/JSEN.2007.891997.

[43] S.D. Senturia, Microsystem Design, Kluwer Academic Publishers, Dortrecht, Netherlands, 2001. doi:10.1017/CBO9781107415324.004.

[44] J.M. Bustjllo, R.T. Howe, R.S. Muller, Surface micromachining for microelectromechanical systems, Proceedings of the IEEE. 86 (1998) 1552–1573. doi:10.1109/5.704260.

[45] A. Stoffel, A. Kovacs, W. Kronast, B. Müller, LPCVD against PECVD for micromechanical applications, Journal of Micromechanics and Microengineering. 6 (1996) 1–13. http://iopscience.iop.org/0960-1317/6/1/001.

[46] M. Mehregany, C.A. Zorman, N. Rajan, Silicon carbide MEMS for harsh environments, Proceedings of the IEEE. 86 (1998) 1594–1609. doi:10.1109/5.704265.

[47] N.B. Strokan, A.M. Ivanov, N.S. Savkina, A.M. Strelchuk, A.A. Lebedev, M. Syväjärvi, R. Yakimova, Detection of strongly and weakly ionizing radiation by triode structure based on SIC films, Journal of Applied Physics. 93 (2003) 5714–5719. doi:10.1063/1.1564284.

[48] R.C. Liudi Jiang, A Review of Silicon Carbide Development in MEMS Applications, International Journal of Computational Materials Science and Surface Engineering. 2 (2009) 225–240.

[49] J. Mouro, A. Gualdino, V. Chu, S. Member, J.P. Conde, Tunable Properties of Hydrogenated Amorphous / Nanocrystalline Silicon Thin-Films for Enhanced MEMS Resonators Performance, 23 (2014) 600–609.

[50] M. Bouchina, P. Brogueira, V. Chu, J.P. Conde, Amorphous silicon air-gap resonators on large-area substrates, Applied Physics Letters. 77 (2000) 907–909. doi:10.1063/1.1306912.

[51] X.M.H. Huang, C.A. Zorman, M. Mehregany, Michael L. Roukes, Nanodevice motion at microwave frequencies, Nature. 421 (2003) 496–497.

[52] X. Du, I. Skachko, E.Y. Andrei, A. Barker, Approaching ballistic transport in suspended

graphene., Nature Nanotechnology. 3 (2008) 491–5. doi:10.1038/nnano.2008.199.

[53]   P. Vogt, P. De Padova, C. Quaresima, J. Avila, E. Frantzeskakis, M.C. Asensio, A. Resta, B. Ealet, G. Le Lay, Silicene: Compelling experimental evidence for graphenelike two-dimensional silicon, Physical Review Letters. 108 (2012) 1–5. doi:10.1103/PhysRevLett.108.155501.

[54]   S. Maruthoor, A. Ajayakumar, T. Fuchs, O. Jakovlev, H. Reinecke, J. Wilde, Mechanical Characterization of Polycrystalline and Amorphous Silicon Carbide Thin Films Using Bulge Test, Journal of Microelectromechanical Systems. 22 (2013) 140–146. doi:10.1109/JMEMS.2012.2218577.

[55]   C. Wu, C.A. Zorman, M. Mehregany, Fabrication and Testing of Bulk Micromachined Silicon Carbide Piezoresistive Pressure Sensors for High Temperature Applications, IEEE Sensors Journal. 6 (2006) 316–324. doi:10.1109/JSEN.2006.870145.

[56]   R.G. Azevedo, S. Member, D.G. Jones, A. V Jog, B. Jamshidi, D.R. Myers, L. Chen, X. Fu, M. Mehregany, S. Member, M.B.J. Wijesundara, A.P. Pisano, A SiC MEMS Resonant Strain Sensor for Harsh Environment Applications, IEEE Sensors Journal. 7 (2007) 568–576.

[57]   S.S. Lin, Light-emitting two-dimensional ultrathin silicon carbide, Journal of Physical Chemistry C. 116 (2012) 3951–3955. doi:10.1021/jp210536m.

[58]   S. Chabi, H. Chang, Y. Xia, Y. Zhu, From graphene to silicon carbide: ultrathin silicon carbide flakes, Nanotechnology. 27 (2016) 75602. doi:10.1088/0957-4484/27/7/075602.

[59]   B.T. Kelly, Physics of Graphite, Applied Science Publishers, London, U.K., Applied Science, London, 1981.

[60]   C. Lee, X. Wei, J.W. Kysar, J. Hone, Measurement of the elastic properties and intrinsic strength of monolayer graphene., Science. 321 (2008) 385–8. doi:10.1126/science.1157996.

[61]   X. Lu, M. Yu, H. Huang, R.S. Ruoff, Tailoring graphite with the goal of achieving single sheets, Nanotechnology. 10 (1999) 269. doi:10.1088/0957-4484/10/3/308.

[62]   J.S. Bunch, A.M. van der Zande, S.S. Verbridge, I.W. Frank, D.M. Tanenbaum, J.M. Parpia, H.G. Craighead, P.L. McEuen, Electromechanical resonators from graphene sheets., Science. 315 (2007) 490–3. doi:10.1126/science.1136836.

[63]   A. Reina, X. Jia, J. Ho, D. Nezich, H. Son, V. Bulovic, M.S. Dresselhaus, J. Kong, Large area, few-layer graphene films on arbitrary substrates by chemical vapor deposition., Nano Letters. 9 (2009) 30–5. doi:10.1021/nl801827v.

[64]   A.M. Van Der Zande, R.A. Barton, J.S. Alden, C.S. Ruiz-Vargas, W.S. Whitney, P.H.Q. Pham, J. Park, J.M. Parpia, H.G. Craighead, P.L. McEuen, Large-scale arrays of single-layer graphene resonators, Nano Letters. 10 (2010) 4869–4873. doi:10.1021/nl102713c.

[65]   H. Medina, Y.-C. Lin, C. Jin, C.-C. Lu, C.-H. Yeh, K.-P. Huang, K. Suenaga, J. Robertson, P.-W. Chiu, Metal-Free Growth of Nanographene on Silicon Oxides for Transparent Conducting Applications, Advanced Functional Materials. 22 (2012) 2123–2128.

doi:10.1002/adfm.201102423.

[66]   L. Zhang, Z. Shi, Y. Wang, R. Yang, D. Shi, G. Zhang, Catalyst-free growth of nanographene films on various substrates, Nano Research. 4 (2010) 315–321. doi:10.1007/s12274-010-0086-5.

[67]   J. Zhao, C. He, R. Yang, Z. Shi, M. Cheng, W. Yang, G. Xie, D. Wang, D. Shi, G. Zhang, Ultra-sensitive strain sensors based on piezoresistive nanographene films, Applied Physics Letters. 101 (2012) 063112 1-5. doi:10.1063/1.4742331.

[68]   J. Sun, M.E. Schmidt, M. Muruganathan, H.M.H. Chong, H. Mizuta, Large-scale nanoelectromechanical switches based on directly deposited nanocrystalline graphene on insulating substrates, Nanoscale. 8 (2016) 6659–6665. doi:10.1039/C6NR00253F.

[69]   H. Medina, Y.C. Lin, C.H. Jin, C.C. Lu, C.H. Yeh, K.P. Huang, K. Suenaga, J. Robertson, P.W. Chiu, Metal-Free Growth of Nanographene on Silicon Oxides for Transparent Conducting Applications, Advanced Functional Materials. 22 (2012) 2123–2128. doi:10.1002/adfm.201102423.

[70]   K. V Emtsev, A. Bostwick, K. Horn, J. Jobst, G.L. Kellogg, L. Ley, J.L. McChesney, T. Ohta, S.A. Reshanov, J. Röhrl, E. Rotenberg, A.K. Schmid, D. Waldmann, H.B. Weber, T. Seyller, Towards wafer-size graphene layers by atmospheric pressure graphitization of silicon carbide., Nature Materials. 8 (2009) 203–207. doi:10.1038/nmat2382.

[71]   S. Shivaraman, R.A. Barton, X. Yu, J. Alden, L. Herman, M.V.S. Chandrashekhar, J. Park, P.L. Mceuen, J.M. Parpia, H.G. Craighead, M.G. Spencer, Free-Standing Epitaxial Graphene, Nano Letters. 9 (2009) 1–6. doi:10.1021/nl900479g.

[72]   S.M. Spearing, Materials issues in microelectromechanical systems (MEMS), Acta Materialia. 48 (2000) 179–196.

[73]   S.D. Janssens, S. Drijkoningen, K. Haenen, Ultra-thin nanocrystalline diamond membranes as pressure sensors for harsh environments, Applied Physics Letters. 104 (2014) 73107. doi:10.1063/1.4866028.

[74]   W. Wang, M. Polo, G. Sanchez, Internal stress and strain in heavily boron-doped diamond films grown by microwave plasma and hot filament chemical vapor deposition, Journal of Applied Physics. 80 (1996). http://scitation.aip.org/content/aip/journal/jap/80/3/10.1063/1.362996.

[75]   J.W. Baldwin, M.K. Zalalutdinov, T. Feygelson, B.B. Pate, J.E. Butler, B.H. Houston, Nanocrystalline diamond resonator array for RF signal processing, Diamond and Related Materials. 15 (2006) 2061–2067. doi:10.1016/j.diamond.2006.09.009.

[76]   N.G. Ferreira, E. Abramof, E.. Corat, V.J. Trava-Airoldi, Residual stresses and crystalline quality of heavily boron-doped diamond films analysed by micro-Raman spectroscopy and X-ray diffraction, Carbon. 41 (2003) 1301–1308. doi:10.1016/S0008-6223(03)00071-X.

[77]   Y. Tao, J.M. Boss, B.A. Moores, C.L. Degen, Single-crystal diamond nanomechanical

resonators with quality factors exceeding one million., Nature Communications. 5 (2014) 3638. doi:10.1038/ncomms4638.

[78]   L. Sekaric, J.M. Parpia, H.G. Craighead, T. Feygelson, B.H. Houston, J.E. Butler, Nanomechanical resonant structures in nanocrystalline diamond, Applied Physics Letters. 81 (2002) 4455. doi:10.1063/1.1526941.

[79]   N. Sepulveda, D. Aslam, J.P. Sullivan, Polycrystalline diamond MEMS resonator technology for sensor applications, Diamond and Related Materials. 15 (2006) 398–403. doi:10.1016/j.diamond.2005.08.032.

[80]   T. Yoshikawa, F. Gao, V. Zuerbig, C. Giese, C.E. Nebel, O. Ambacher, V. Lebedev, Pinhole-free ultra-thin nanocrystalline diamond film growth via electrostatic self-assembly seeding with increased salt concentration of nanodiamond colloids, Diamond and Related Materials. 63 (2016) 103–107. doi:10.1016/j.diamond.2015.08.010.

[81]   A.C. Ferrari, J. Robertson, Interpretation of Raman spectra of disordered and amorphous carbon, Physical Review B. 61 (2000) 14095–14107. doi:10.1103/PhysRevB.61.14095.

[82]   M. Tomi, A. Isacsson, M. Oksanen, D. Lyashenko, J.P. Kaikkonen, S. Tervakangas, J. Kolehmainen, P.J. Hakonen, Buckled diamond-like carbon nanomechanical resonators, Nanoscale. 7 (2015) 14747–14751. doi:10.1039/C5NR02820E.

[83]   J.K. Luo, Y.Q. Fu, H.R. Le, J.A. Williams, S.M. Spearing, W.I. Milne, Diamond and diamond-like carbon MEMS, Journal of Micromechanics and Microengineering. 17 (2007) S147–S163. doi:10.1088/0960-1317/17/7/S12.

[84]   N. Ravi, V.L. Bukhovets, I.G. Varshavskaya, G. Sundararajan, Deposition of diamond-like carbon films on aluminium substrates by RF-PECVD technique: Influence of process parameters, Diamond and Related Materials. 16 (2007) 90–97. doi:10.1016/j.diamond.2006.04.001.

[85]   M. Stüber, S. Ulrich, H. Leiste, A. Kratzsch, H. Holleck, Graded layer design for stress-reduced and strongly adherent superhard amorphous carbon films, Surface and Coatings Technology. 116–119 (1999) 591–598. doi:10.1016/S0257-8972(99)00224-8.

[86]   M.C. Polo, J.L. Andú Jar, A. Hart, J. Robertson, W.I. Milne, Preparation of tetrahedral amorphous carbon films by filtered cathodic vacuum arc deposition, Diamond and Related Materials. 9 (2000) 663–667. doi:10.1016/S0925-9635(99)00339-8.

[87]   V. Sazonova, Y. Yaish, H. Ustünel, D. Roundy, T. a Arias, P.L. McEuen, A tunable carbon nanotube electromechanical oscillator., Nature. 431 (2004) 284–7. doi:10.1038/nature02905.

[88]   E. Peiner, A. Tibrewala, R. Bandorf, H. Lüthje, L. Doering, W. Limmer, Diamond-like carbon for MEMS, Journal of Micromechanics and Microengineering. 17 (2007) S83–S90. doi:10.1088/0960-1317/17/7/S04.

[89]   D. Yoon, Y.-W. Son, H. Cheong, Negative thermal expansion coefficient of graphene measured by Raman spectroscopy., Nano Letters. 11 (2011) 3227–31.

doi:10.1021/nl201488g.

[90] M.C. Salvadori, M.C. Fritz, C. Carraro, R. Maboudian, O.R. Monteiro, I.G. Brown, Characterization of AFM cantilevers coated with diamond-like carbon, Diamond and Related Materials. 10 (2001) 2190–2194.

[91] S.-E. Zhu, R. Shabani, J. Rho, Y. Kim, B.H. Hong, J.-H. Ahn, H.J. Cho, Graphene-based bimorph microactuators., Nano Letters. 11 (2011) 977–81. doi:10.1021/nl103618e.

[92] O. Loh, X. Wei, J. Sullivan, L.E. Ocola, R. Divan, H.D. Espinosa, Carbon-Carbon Contacts for Robust Nanoelectromechanical Switches, Advanced Materials. 24 (2012) 2463–2468. doi:10.1002/adma.201104889.

[93] A. Midilli, M. Ay, I. Dincer, M.A. Rosen, On hydrogen and hydrogen energy strategies I : Current status and needs, Renewable and Sustainable Energy Reviews. 9 (2005) 255–271. doi:10.1016/j.rser.2004.05.003.

[94] J. Dong, Y.S. Lin, M. Kanezashi, Z. Tang, Microporous inorganic membranes for high temperature hydrogen purification, Journal of Applied Physics. 104 (2008) 121301. doi:10.1063/1.3041061.

[95] M.T. Ravanchi, T. Kaghazchi, A. Kargari, Application of membrane separation processes in petrochemical industry: a review, Desalination. 235 (2009) 199–244. doi:10.1016/j.desal.2007.10.042.

[96] K.H. Kaplan, Helium shortage hampers research and industry, Physics Today. 60 (2007) 31–32. doi:10.1063/1.2754594.

[97] M. Bartolomei, E. Carmona-Novillo, M.I. Hernández, J. Campos-Martínez, F. Pirani, G. Giorgi, Graphdiyne pores: Ad hoc openings for helium separation applications, Journal of Physical Chemistry C. 118 (2014) 29966–29972. doi:10.1021/jp510124e.

[98] F. Li, Y. Qu, M. Zhao, Efficient helium separation of graphitic carbon nitride membrane, Carbon. 95 (2015) 51–57. doi:10.1016/j.carbon.2015.08.013.

[99] L. Zhu, Q. Xue, X. Li, T. Wu, Y. Jin, W. Xing, C2N: an excellent two-dimensional monolayer membrane for He separation, Journal of Materials Chemistry A. 3 (2015) 21351–21356. doi:10.1039/C5TA05700K.

[100] P. Pandey, R.S. Chauhan, Membranes for Gas Separation, Progress in Polymer Science. 26 (2001) 853–893. doi:10.1038/nchem.555.

[101] Y. Yampolskii, B. Freeman, Membrane Gas Separation, John Wiley & Sons, Ltd., Chichester, 2010. doi:10.1017/CBO9781107415324.004.

[102] M.B. Rao, S. Sircar, Nanoporous Carbon Membranes for Separation of Gas-Mixtures by Selective Surface Flow, Journal of Membrane Science. 85 (1993) 253–264. doi:10.1016/0376-7388(93)85279-6.

[103] L.M. Robeson, The upper bound revisited, Journal of Membrane Science. 320 (2008) 390–400. doi:10.1016/j.memsci.2008.04.030.

[104] B. Elyassi, M. Sahimi, T.T. Tsotsis, Silicon carbide membranes for gas separation applications, Journal of Membrane Science. 288 (2007) 290–297. doi:10.1016/j.memsci.2006.11.027.

[105] S.A. Stern, The "barrer" permeability unit, Journal of Polymer Science Part A-2: Polymer Physics. 6 (1968) 1933–1934. doi:10.1002/pol.1968.160061108.

[106] Table of units, Journal of Membrane Science. 366 (2011) III–III. doi:Doi: 10.1016/s0376-7388(10)00894-x.

[107] Y. Gu, S.T. Oyama, Permeation properties and hydrothermal stability of silica-titania membranes supported on porous alumina substrates, Journal of Membrane Science. 345 (2009) 267–275. doi:10.1016/j.memsci.2009.09.009.

[108] R.M. De Vos, H. Verweij, High-Selectivity, High-Flux Silica Membranes for Gas Separation, Science. 279 (1998) 1710–1711. doi:10.1126/science.279.5357.1710.

[109] S.R. Venna, M.A. Carreon, Metal organic framework membranes for carbon dioxide separation, Chemical Engineering Science. 124 (2015) 3–19. doi:10.1016/j.ces.2014.10.007.

[110] Y. Peng, Y. Li, Y. Ban, H. Jin, W. Jiao, X. Liu, W. Yang, Metal-organic framework nanosheets as building blocks for molecular sieving membranes, Science. 346 (2014) 1356–1359. doi:10.1126/science.1254227.

[111] H. Guo, G. Zhu, I.J. Hewitt, S. Qiu, "Twin copper source" growth of metal-organic framework membrane: Cu3(BTC)2 with high permeability and selectivity for recycling H2, Journal of the American Chemical Society. 131 (2009) 1646–1647. doi:10.1021/ja8074874.

[112] S.M. Saufi, A.F. Ismail, Fabrication of carbon membranes for gas separation - A review, Carbon. 42 (2004) 241–259. doi:10.1016/j.carbon.2003.10.022.

[113] M. Wissler, Graphite and carbon powders for electrochemical applications, Journal of Power Sources. 156 (2006) 142–150. doi:10.1016/j.jpowsour.2006.02.064.

[114] R.S.A. De Lange, K. Keizer, A.J. Burggraaf, Analysis and theory of gas transport in microporous sol-gel derived ceramic membranes, Journal of Membrane Science. 104 (1995) 81–100. doi:10.1016/0376-7388(95)00014-4.

[115] K. Celebi, J. Buchheim, R.M. Wyss, A. Droudian, P. Gasser, I. Shorubalko, J.-I. Kye, C. Lee, H.G. Park, Ultimate permeation across atomically thin porous graphene., Science. 344 (2014) 289–92. doi:10.1126/science.1249097.

[116] M.S.H. Boutilier, C. Sun, S.C. O'Hern, H. Au, N.G. Hadjiconstantinou, R. Karnik, Implications of permeation through intrinsic defects in graphene on the design of defect-tolerant membranes for gas separation, ACS Nano. 8 (2014) 841–849. doi:10.1021/nn405537u.

[117] K.R. Williams, K. Gupta, M. Wasilik, Etch Rates for Micromachining Processing - Part II, Journal of Microelectromechanical Systems. 12 (2004) 761–778. doi:10.1109/JMEMS.2003.820936.

[118] D. Grech, K.S. Kiang, J. Zekonyte, M. Stolz, R.J.K. Wood, H.M.H. Chong, Highly linear and large spring deflection characteristics of a Quasi-Concertina MEMS device, Microelectronic Engineering. 119 (2014) 75–78. doi:10.1016/j.mee.2014.02.016.

[119] J.-Y. Jin, S. Yoo, J.-S. Bae, Y.-K. Kim, Deep wet etching of borosilicate glass and fused silica with dehydrated AZ4330 and a Cr/Au mask, Journal of Micromechanics and Microengineering. 24 (2014) 15003. doi:10.1088/0960-1317/24/1/015003.

[120] Hardware manual Polytec Scanning Vibrometer PSV 300, (n.d.).

[121] P. Tremblay, M. Savard, J. Vermette, R. Paquin, Gas permeability, diffusivity and solubility of nitrogen, helium, methane, carbon dioxide and formaldehyde in dense polymeric membranes using a new on-line permeation apparatus, Journal of Membrane Science. 282 (2006) 245–256. doi:10.1016/j.memsci.2006.05.030.

[122] G. Firpo, E. Angeli, L. Repetto, U. Valbusa, Permeability thickness dependence of polydimethylsiloxane (PDMS) membranes, Journal of Membrane Science. 481 (2015) 1–8. doi:10.1016/j.memsci.2014.12.043.

[123] Operating Manudal and Programming Reference: Models RGA100, RGA200 and RGA300 Residual Gas Analyzer, Stanford Research Systems, USA, 1996.

[124] C.D. Ehrlich, J.A. Basford, Recommended practices for the calibration and use of leaks, Journal of Vacuum Science & Technology A. 10 (1992) 1–17. doi:10.1116/1.578137.

[125] Y. Li, F. Liang, H. Bux, W. Yang, J. Caro, Zeolitic imidazolate framework ZIF-7 based molecular sieve membrane for hydrogen separation, Journal of Membrane Science. 354 (2010) 48–54. doi:10.1016/j.memsci.2010.02.074.

[126] Y. Ishikawa, T. Yoshimura, Importance of the surface oxide layer in the reduction of outgassing from stainless steels, Journal of Vacuum Science & Technology A. 13 (1995) 1847–1852. doi:+10.1116/1.579669.

[127] K.E. Petersen, C.R. Guarnieri, Young's modulus measurements of thin films using micromechanics, Journal of Applied Physics. 50 (1979) 6761. doi:10.1063/1.325870.

[128] S. Sundararajan, B. Bhushan, Development of AFM-based techniques to measure mechanical properties of nanoscale structures, Sensors and Actuators A: Physical. 101 (2002) 338–351. doi:10.1016/S0924-4247(02)00268-6.

[129] BS 2782-10: Method 1005: 1977. Methods of testing plastics. Glass reinforced plastics. Determination of flexural properties. Three point method, BSI. (1983).

[130] J. Vlassak, W. Nix, A new bulge test technique for the determination of Young's modulus and Poisson's ratio of thin films, Journal of Materials Research. 94305 (1992). http://journals.cambridge.org/abstract_S0884291400019099.

[131] P.M. Osterberg, S.D. Senturia, M-test: A test chip for MEMS material property measurement using electrostatically actuated test structures, Journal of Microelectromechanical Systems. 6 (1997) 107–118. doi:10.1109/84.585788.

[132] Y. Xiang, The mechanical properties of freestanding electroplated Cu thin films, (2006) 1607–1618. doi:10.1557/JMR.2006.0195.

[133] B.T. Kelly, Physics of graphite, Applied Science Publishers, London, U.K., 1981.

[134] S. Yoda, M. Eto, T. Oku, Change in dynamic young's modulus of nuclear-grade isotropic graphite during tensile and compressive stressing, Journal of Nuclear Materials. 119 (1983) 278–283. doi:10.1016/0022-3115(83)90204-0.

[135] M.A. Pimenta, G. Dresselhaus, M.S. Dresselhaus, L.G. Cançado, A. Jorio, R. Saito, Studying disorder in graphite-based systems by Raman spectroscopy, Physical Chemistry Chemical Physics. 9 (2007) 1276. doi:10.1039/b613962k.

[136] V. Ziebart, O. Paul, H. Baltes, Strongly buckled square micromachined membranes, Journal of Microelectromechanical Systems. 8 (1999) 423–432. doi:10.1109/84.809057.

[137] E. Liu, L. Li, B. Blanpain, J.P. Celis, Residual stresses of diamond and diamondlike carbon films, Journal of Applied Physics. 98 (2005) 73515. doi:10.1063/1.2071451.

[138] D. Ngo, X. Feng, Y. Huang, a. J. Rosakis, M. a. Brown, Thin film/substrate systems featuring arbitrary film thickness and misfit strain distributions. Part I: Analysis for obtaining film stress from non-local curvature information, International Journal of Solids and Structures. 44 (2007) 1745–1754. doi:10.1016/j.ijsolstr.2006.10.016.

[139] A.H. Nayfeh, S. a. Emam, Exact solution and stability of postbuckling configurations of beams, Nonlinear Dynamics. 54 (2008) 395–408. doi:10.1007/s11071-008-9338-2.

[140] J.R. Cost, K.R. Janowski, R.C. Rossi, Elastic properties of isotropic graphite, Philosophical Magazine. 17 (1968) 851–854. doi:10.1080/14786436808223035.

[141] M.J. Kobrinsky, E.R. Deutsch, S.D. Senturia, Effect of support compliance and residual stress on the shape of doubly supported surface-micromachined beams, Journal of Microelectromechanical Systems. 9 (2000) 361–369. doi:10.1109/84.870062.

[142] W.B. Gauster, Elastic Constants and Gruneisen Parameters of Pyrolytic Graphite, Philosophical Magazine. 25 (1972) 687.

[143] S.J. Fishlock, D. Grech, J.W. McBride, H.M.H. Chong, S.H. Pu, Mechanical characterisation of nanocrystalline graphite using micromechanical structures, Microelectronic Engineering. 159 (2016) 184–189. doi:10.1016/j.mee.2016.03.040.

[144] E. Cianci, A. Schina, A. Minotti, S. Quaresima, V. Foglietti, Dual frequency PECVD silicon nitride for fabrication of CMUTs membranes, Sensors and Actuators A: Physical. 127 (2006) 80–87. doi:10.1016/j.sna.2005.11.053.

[145] F. Delachat, C. Constancias, F. Fournel, C. Morales, B. Le Drogoff, M. Chaker, J. Margot, Fabrication of Buckling Free Ultrathin Silicon Membranes by Direct Bonding with Thermal Difference, ACS Nano. 9 (2015) 3654–3663.

[146] R.G. Azevedo, J.Z.J. Zhang, D.G. Jones, D.R. Myers, A. V Jog, B. Jamshidi, M.B.J. Wijesundara, R. Maboudian, A.P. Pisano, Silicon Carbide Coated Mems Strain Sensor for

Harsh, 2007 IEEE 20th International Conference on Micro Electro Mechanical Systems MEMS. (2007) 643–646. doi:10.1109/MEMSYS.2007.4433166.

[147] X.L. Feng, M.H. Matheny, C.A. Zorman, M. Mehregany, M.L. Roukes, Low voltage nanoelectromechanical switches based on silicon carbide nanowires, Nano Letters. 10 (2010) 2891–2896. doi:10.1021/nl1009734.

[148] L. Meirovitch, Fundamentals of Vibrations, McGraw-Hill Book Company, Singapore, 2001.

[149] S. Timoshenko, Vibration problems in engineering, D. Van Nostrand Company, INC., New York, USA, 1937. doi:10.1016/S0016-0032(29)91051-6.

[150] R. Sandberg, W. Svendsen, K. Mølhave, A. Boisen, Temperature and pressure dependence of resonance in multi-layer microcantilevers, Journal of Micromechanics and Microengineering. 15 (2005) 1454–1458. doi:10.1088/0960-1317/15/8/011.

[151] M.P. Norton, D.G. Karczub, Fundamentals of Noise and Vibration Analysis for Engineers, Cambridge University Press, Cambridge, UK, 2003. doi:10.1121/1.400194.

[152] S.S. Verbridge, D.F. Shapiro, H.G. Craighead, J.M. Parpia, Macroscopic tuning of nanomechanics: substrate bending for reversible control of frequency and quality factor of nanostring resonators., Nano Letters. 7 (2007) 1728–35. doi:10.1021/nl070716t.

[153] A. Bokaian, Natural frequencies of beams under tensile axial loads, Journal of Sound and Vibration. 142 (1990) 481–498. doi:10.1016/0022-460X(92)90370-D.

[154] K. Babaei Gavan, E.W.J.M. van der Drift, W.J. Venstra, M.R. Zuiddam, H.S.J. van der Zant, Effect of undercut on the resonant behaviour of silicon nitride cantilevers, Journal of Micromechanics and Microengineering. 19 (2009) 35003. doi:10.1088/0960-1317/19/3/035003.

[155] T. Fritz, H.S. Cho, K.J. Hemker, W. Mokwa, U. Schnakenberg, Characterization of electroplated nickel, Microsystem Technologies. 9 (2003) 87–91. doi:10.1007/s00542-002-0199-1.

[156] A.B. Hutchinson, P.A. Truitt, K.C. Schwab, L. Sekaric, J.M. Parpia, H.G. Craighead, J.E. Butler, Dissipation in nanocrystalline-diamond nanomechanical resonators, Applied Physics Letters. 84 (2004) 972–974. doi:10.1063/1.1646213.

[157] A.R. Kermany, G. Brawley, N. Mishra, E. Sheridan, W.P. Bowen, F. Iacopi, Microresonators with Q-factors over a million from highly stressed epitaxial silicon carbide on silicon, Applied Physics Letters. 104 (2014) 81901. doi:10.1063/1.4866268.

[158] V. Adiga, a. Sumant, S. Suresh, C. Gudeman, O. Auciello, J. Carlisle, R. Carpick, Mechanical stiffness and dissipation in ultrananocrystalline diamond microresonators, Physical Review B. 79 (2009) 245403. doi:10.1103/PhysRevB.79.245403.

[159] R.F. Wiser, J. Chung, M. Mehregany, S. Member, C.A. Zorman, M. Tabib-azar, Polycrystalline Silicon-Carbide Surface-Micromachined Vertical Resonators — Part II : Electrical Testing and Material Property Extraction, 14 (2005) 567–578.

[160] F. Rose, A. Debray, P. Martin, H. Fujita, H. Kawakatsu, Suspended HOPG nanosheets for HOPG nanoresonator engineering and new carbon nanostructure synthesis, Nanotechnology. 135 (2006) 5192. doi:10.1002/adfm.200600179.

[161] N.W. Ockwig, T.M. Nenoff, Membranes for hydrogen separation, Chemical Reviews. 107 (2007) 4078–4110. doi:10.1021/cr0501792.

[162] A.J. Burggraaf, Single gas permeation of thin zeolite (MFI) membranes: Theory and analysis of experimental observations, Journal of Membrane Science. 155 (1999) 45–65. doi:10.1016/S0376-7388(98)00295-6.

[163] J. Gilron, A. Soffer, Knudsen diffusion in microporous carbon membranes with molecular sieving character, Journal of Membrane Science. 209 (2002) 339–352. doi:10.1016/S0376-7388(02)00074-1.

[164] J. Xiao, J. Wei, Diffusion mechanism of hydrocarbons in zeolites-I. Theory, Chemical Engineering Science. 47 (1992) 1123–1141. doi:10.1016/0009-2509(92)80236-6.

[165] N. Mehio, S. Dai, D.E. Jiang, Quantum mechanical basis for kinetic diameters of small gaseous molecules, Journal of Physical Chemistry A. 118 (2014) 1150–1154. doi:10.1021/jp412588f.

[166] W.J.W. Bakker, L.J.P. Van Den Broeke, F. Kapteijn, J.A. Moulijn, Temperature dependence of one-component permeation through a silicalite-1 membrane, AIChE Journal. 43 (1997) 2203–2214. doi:10.1002/aic.690430907.

[167] T.C. Bowen, R.D. Noble, J.L. Falconer, Fundamentals and applications of pervaporation through zeolite membranes, Journal of Membrane Science. 245 (2004) 1–33. doi:10.1016/j.memsci.2004.06.059.

[168] Y. Yampolskii, I. Pinnau, B. Freeman, Materials Science of Membranes for Gas and Vapor Separation Materials Science of Membranes for Gas and Vapor Separation, John Wiley & Sons, Ltd., Chichester, 2006. doi:10.1002/047002903X.

[169] A.W. Thornton, T. Hilder, A.J. Hill, J.M. Hill, Predicting gas diffusion regime within pores of different size, shape and composition, Journal of Membrane Science. 336 (2009) 101–108. doi:10.1016/j.memsci.2009.03.019.

[170] H.L. Castricum, H.F. Qureshi, A. Nijmeijer, L. Winnubst, Hybrid silica membranes with enhanced hydrogen and CO2 separation properties, Journal of Membrane Science. 488 (2015) 121–128. doi:10.1016/j.memsci.2015.03.084.

[171] W.J. Koros, G.K. Fleming, Membrane-based gas separation, Journal of Membrane Science. 83 (1993) 1–80. doi:10.1016/0376-7388(93)80013-N.

[172] H.W. Kim, H.W. Yoon, S. Yoon, B.M. Yoo, B.K. Ahn, Y.H. Cho, H.J. Shin, H. Yang, U. Paik, S. Kwon, Selective Gas Transport Through few-layered graphene and praphene oxide membranes, Science. 342 (2013) 91–95. doi:10.1126/science.1236098.

[173] Z. Tang, J. Dong, T.M. Nenoff, Internal surface modification of MFI-type zeolite membranes

for high selectivity and high flux for hydrogen, Langmuir. 25 (2009) 4848–4852. doi:10.1021/la900474y.

[174] M. Hong, J.L. Falconer, R.D. Noble, Modification of zeolite membranes for H2 separation by catalytic cracking of methyldiethoxysilane, Ind. Eng. Chem. Res. Industrial & Engineering Chemistry Research. 44 (2005) 4035–4041. doi:10.1021/ie048739v.

[175] D.H. Weinkauf, D.R. Paul, Gas transport properties of thermotropic liquid-crystalline copolyesters. II. The effects of copolymer composition, Journal of Polymer Science, Part B: Polymer Physics. 30 (1992) 837–849. doi:10.1002/polb.1992.090300805.

[176] G. Polotskaya, M. Goikhman, I. Podeshvo, V. Kudryavtsev, Z. Pientka, L. Brozova, M. Bleha, Gas transport properties of polybenzoxazinoneimides and their prepolymers, Polymer. 46 (2005) 3730–3736. doi:10.1016/j.polymer.2005.02.111.

[177] C.M. Lee, J. Choi, Direct growth of nanographene on glass and postdeposition size control, Applied Physics Letters. 98 (2011) 1–4. doi:10.1063/1.3587784.

[178] S. Huebner, N. Miyakawa, A. Pahlke, F. Kreupl, Design and properties of low-energy X-ray transmission windows based on graphenic carbon, Physica Status Solidi (B) Basic Research. 252 (2015) 2564–2573. doi:10.1002/pssb.201552216.

[179] C. Jiang, S. Markutsya, Y. Pikus, V. V Tsukruk, Freely suspended nanocomposite membranes as highly sensitive sensors, Nature Materials. 3 (2004) 721–728. doi:10.1038/nmat1212.

[180] Y.A. Kim, K. Fujisawa, H. Muramatsu, T. Hayashi, M. Endo, T. Fujimori, K. Kaneko, M. Terrones, J. Behrends, A. Eckmann, C. Casiraghi, K.S. Novoselov, R. Saito, M.S. Dresselhaus, Raman spectroscopy of boron-doped single-layer graphene, ACS Nano. (2012) 6293–6300. http://pubs.acs.org/doi/abs/10.1021/nn301728j.

[181] C. Chen, S. Rosenblatt, K.I. Bolotin, W. Kalb, P. Kim, I. Kymissis, H.L. Stormer, T.F. Heinz, J. Hone, Performance of monolayer graphene nanomechanical resonators with electrical readout., Nature Nanotechnology. 4 (2009) 861–7. doi:10.1038/nnano.2009.267.